A polarizing Fourier transform spectrometer for atmospheric spectroscopy at millimeter wavelengths

by

Miguel Velázquez de la Rosa Becerra

A thesis submitted to the Instituto Nacional de Astrofísica, Optica y Electrónica for the degree of Doctor of Philosophy in the department of Astrophysics.

Supervisor:

Dr. David H. Hughes.

Sta. Ma. Tonantzintla, Pue. México

Enero, 2007

A Raquel...

que con gran amor y

paciencia me ha motivado

a finalizar este trabajo, gracias.

Quiero agradecer ...

A David Hughes y a Daniel Ferrusca por compartir conmigo su trabajo y amistad. A mis sinodales, Dra. Esperanza Carrasco, Dr. Alejandro Cornejo, Dr. Alfonso Torres, Dr. Luis Salas y Dr. Jesús González, por sus comentarios y observaciones.

A mis compañeros del INAOE y amigos: Perla, Felix, Ary, Liliana, Olga y Daniel, Izbeth, Martha y a tantos buenos amigos y gente querida que me han acompañado durante estos años.

Por último, al CONACYT por apoyarme económicamente para realizar estos estudios.

Resumen

Esta tesis describe el diseño, integración y caracterización de un sistema espectroscópico para su operación en longitudes de onda milimétrica, basado en los principios de un espectrómetro de transformada de Fourier Martin-Puplett. El objetivo principal de este proyecto instrumental fue caracterizar las variaciones estaciónales en las ventanas de transmisión atmosférica del cielo en Sierra La Negra, el sitio del Gran Telescopio Milimétrico a una altitud de ∼4600 m.

El sistema de detección del FTS-MPI, el cual es montado dentro de un criostato de LN_2/L^4He, usa como dispositivo principal un bolómetro compuesto que opera en temperaturas criogénicas (∼1.5 - 3.9 K). El bolómetro es fabricado con termistor de germanio dopado por transmutación de neutrones (NTD, por sus siglas es ingles). La uniones térmicas y eléctricas son provistas por alambres the niobio-titanio (NbTi) con un diámetro de 12 μm, que definen la conductancia térmica del dispositivo. Los parámetros físicos tales como temperatura de operación, conductancia térmica, capacidad calorífica y respuesta temporal son discutidos y determinados experimentalmente en este trabajo. A partir de estos parámetros fue posible calcular las figuras de mérito del sistema, i.e. NEP y responsividad.

El diseño de la electrónica de operación en frío y ambiente está descrito, así como el sistema de adquisición de datos, implementado con la tecnología NI-DAQ y LabView, que nos permitió el registro de datos y la visualización de ellos pre-procesados.

El espectrómetro es un interferómetro el cual usa un polarizador de rejilla de alambre como divisor de haz. Los dos polarizadores de rejilla de alambre son fabricados con alambre de tungsteno, con un diámetro de 25 μm y un espaciamiento entre alambres de 75 μm. Las dimensiones finales de la óptica del interferómetro, incluyendo polarizadores permitió lograr una respuesta espectral de ∼215 GHz - 2 THz. La óptica de acoplamiento para el bolómetro y el FTS-MPI, así como todas

las partes ópticas y mecánicas del ineterferómetro fueron diseñadas y construidas en el INAOE.

El FTS-MPI fue exitosamente integrado y probado con el sistema de detección en nuestro laboratorio e interferogramas de cargas frías (LN_2) y del cielo fueron obtenidos. El rendimiento óptico del sistema fue determinado a partir del análisis de los interferogramas registrados. Finalmente los espectros de potencia calculados son mostrados, los cuales muestran detección confiable de líneas espectrales relacionadas con la emisión de vapor de agua contenido en la atmósfera.

Abstract

This thesis describes the design, integration and characterization of a spectroscopic system for millimeter wavelength operation based on the principles of Martin-Puplett Fourier transform spectrometer. The initial goal of this experimental project was to characterize the seasonal variations in the atmospheric transmission windows above Sierra La Negra, the site of the Gran Telescopio Milimétrico at an altitude of ∼4600 m.

The detection system of the FTS-MPI, which is mounted inside a LN_2/L^4He cryostat, takes advantage of a single-pixel composite bolometer operating at cryogenics temperatures (∼1.5 - 3.9 K). The bolometer is fabricated with a NTD germanium thermistor. The thermal and electrical links are provided by NbTi wires with a diameter of 12 μm, that define the thermal conductance of the device. The physical parameters, such as bath temperature, thermal conductance, heat capacity and temporal response are discussed and determined experimentally in this work. From these parameters we are able to calculate the figures of merit of the system, i.e. NEP and responsivity.

The design of the cold and warm electronics are described, as well as the data acquisition system, implemented with the technology of NI-DAQ and LabView, that allow us to record the data and to visualize the pre-processed spectra.

The spectrometer is a Martin-Puplett interferometer which uses a wire-grid polarizer as a beam-splitter. The wire-grid polarizers are fabricated with tungsten wire, with a diameter of 25 μm and a wire spacing of 75 μm. The final dimensions of the interferometer optics, including the polarizers, allow us to achieve a spectral response between 215 GHz to 2 THz. The coupling optics for the bolometer and the FTS-MPI, as well as all the optical and mechanical parts of the interferometer were designed and built at INAOE.

The FTS-MPI was successfully integrated and tested with the detection system in our laboratory, and interferograms of cold-loads (LN_2 sources) and of sky

were obtained. The optical performance of the system was determined from the analysis of the recorded interferograms. Finally the computed power-spectra are shown, which provide a confident detection of spectral features related with the water-vapour emission of the atmosphere.

Contents

Chapter 1

Introduction

The Instituto Nacional de Astrofísica Optica y Electrónica, México (INAOE) is building the Large Millimetre Telescope (LMT), the world's largest telescope optimized for millimetre-wavelength single-dish astronomy. The project is being developed in cooperation with the University of Massachusetts (UMASS), USA. The LMT is a 50-m telescope designed to operate in the sub-millimetre/millimetre wavelength regime ($850\mu\text{m} < \lambda < 4000\mu\text{m}$) and is being built on the summit of the Volcán Sierra La Negra at an altitude of 4,600 m, situated $\sim$100 km east of the city of Puebla (latitude $\sim +19$ degree North). The major scientific objective of the LMT is to study the formation of the structure and the evolutionary history of the Universe over an enormous range of physical scales (from dust grains to clusters of galaxies and large-scale structures in the Cosmic microwave background).

Previous site monitoring (Estrada et al., 2002) has demonstrated that the sky opacity at 215 GHz (τ_{215}) above Sierra La Negra is about < 0.2 over the dry winter months with a seasonal increase, during the summer to $0.2 < \tau_{215} < 0.7$. The site has been characterized however with radiometric methods that provided

very narrow-band ($\Delta\nu \sim 300$ MHz) measurements of the sky opacity on time scales of ∼5 minutes. A valuable comparison can be made with the recent total-power observations at 1.1 mm from AzTEC, an LMT first-light instrument, which already completed a successfully scientific run on the 15-m JCMT on Mauna Kea, Hawaii. Figure 1.1 shows the voltage output of one pixel of the AzTEC camera at 1.1 mm, looking at the sky above Mauna Kea. The AzTEC data show significant sky variations on shorter timescales than the radiometric observations from Sierra La Negra reported by Ferrusca (2006). In order to improve the situation and provide broad-band atmospheric data on shorter timescales, INAOE decided to develop the basic technical skills and infrastructure to allow the construction of instrumentation for LMT. To achieve this we first had to create the Millimetre Instrumentation Laboratory (here after MI-Lab) in 2000. Given the relative simplicity of techniques to measure the total power fluctuations for millimetre atmosphere, the MI-lab channeled its initial efforts into instrumentation related to the characterization of the atmosphere above the LMT site using broad-band (continuum) instrumentation at ∼250 GHz.

The goal of the work described in this thesis is therefore the design, construction and testing of a Fourier Transform Spectrometer to characterize the seasonal variations in the transmission of the atmospheric windows available for the LMT observations. The FTS uses a cryogenic single-pixel bolometric system to record the spectrum of the atmosphere in the range of $\sim 200 - 1000$ GHz. The data obtained with the FTS will have a direct impact on the design of the future instrumentation for the LMT and the operational strategies of the telescope following the commissioning in 2007.

1.1 Sub-millimetre/millimetre astronomy

Ground-based access to the sub-millimetre and millimetre wavelength (here after sub-mm/mm) atmospheric windows has only been possible in the last couple of

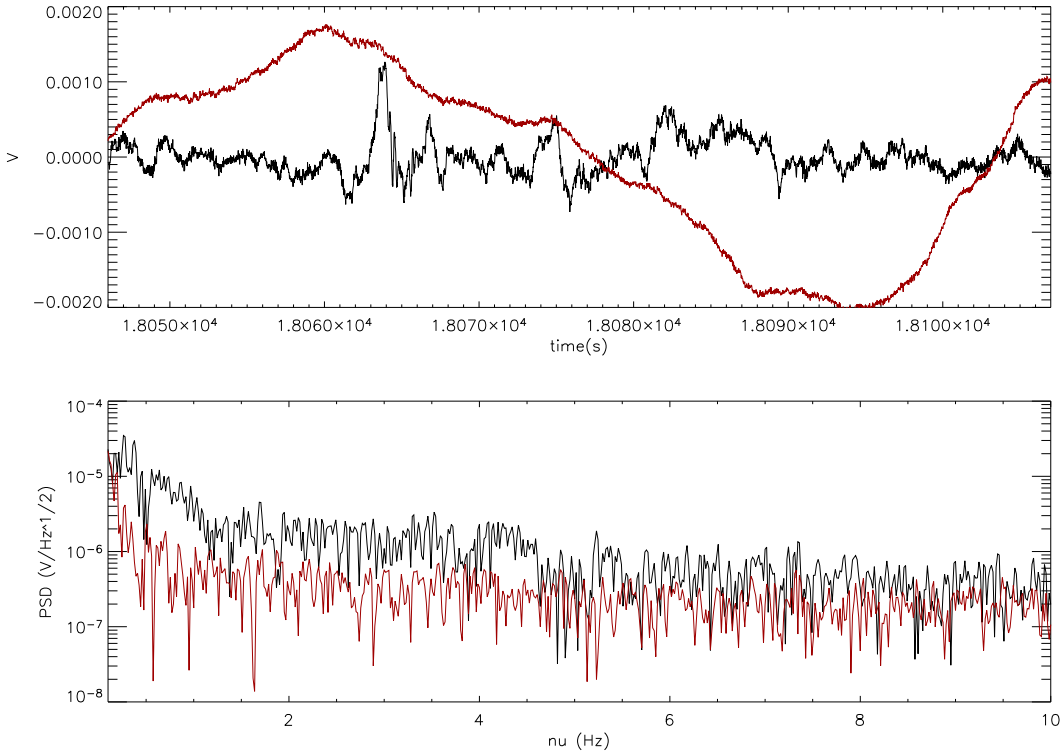

Figure 1.1: Voltage output of one pixel of the AzTEC camera at 1.1 mm, looking at the sky above Mauna Kea. The top panel shows the sky variations over a times-scale of 1 minute. The two curves show measurements taken under different sky opacity conditions($\tau_{215GHz} \sim 0.034$, dark-line; $\tau_{215GHz} \sim 0.114$, red-line). The bottom panel shows the power-spectrum density of the sky under the opacity conditions shown in the upper panel, where the dark-line and red-line again represent low and high opacity conditions.

decades due to the improvements in telescope design and instrument technology (e.g. large aperture telescopes and detections systems based on thermal devices). Observational evidence shows that the Universe is full of very cold material such as planets (with surface temperatures $\sim$ 40 - 750 K), comets ($\sim$10 K at the Oort Cloud and close to 300 K when approaching to the Solar System) and galaxies which contain cold neutral gas and cold molecular gas (T<20 K). All these objects are consequently strong radiators at FIR/sub-mm/mm wavelengths, and the properties of the dusty ISM are strongly related to early evolutionary stages of the galaxies, stars and planets. Furthermore, since the Universe is transparent to sub-mm/mm wavelengths, we are able to measure the rest-frame peak of the FIR emission, which is strongly related to the stellar formation rate obscured by dust in local galaxies and also in galaxies at the highest redshift with the sub-mm/mm observations. In order to understand the origin and evolution of these fundamental astronomical objects, experimental data with suitable resolution ans sensitivity at sub-mm/mm wavelengths are required. Therefore the LMT will play an important role in modern astronomy and astrophysics.

1.2 High-z Universe at sub-mm/mm wavelengths

The Universe is full of cold discrete sources and a diffuse background that radiate strongly at FIR - sub-mm/mm wavelengths. Six decades ago the Big-Bang model, was proposed as an explanation for the origin of the Universe. The Big-Bang model predicts an expanding Universe that causes a redshift in the light coming from very distant objects, which is proportional to their distance from the observer. Also, the model predicts the existence of the isotropic Cosmic Microwave Background (here after CMB) radiation that fills the entire Universe. In 1964, Penzias & Wilson were the first to detect a signal with the expected char-

acteristics of the CMB (Alpher et al., 1948). They measured an excess isotropic sky signal at 4 MHz, using their 20-foot horn reflector antenna in Holmdel, New Jersey, and were not able to attribute the signal to terrestrial sources or any kind of noise coming from their equipment. The signal was equivalent to a blackbody emitter with a temperature of 3.5 ± 1 K, originating from primordial radiation at an epoch when the Universe was very hot and dense (Penzias & Wilson, 1965; Dicke et al., 1965), and the radiation and the matter were strongly coupled. As the Universe cooled to T $\sim$ 10000 K, photons no longer interacted efficiently with the matter and they started to travel freely. In this radiation-dominated epoch, the Universe was in thermodynamic equilibrium and hence produced a Planckian energy distribution which has not been affected by continuous the expansion of the Universe.

The CMB is one of the most exciting topics in modern cosmology and astronomy. After the first detection of the CMB, many other experiments have been designed in order to measure the CMB power spectrum on different angular scales which provides information on cosmological parameters and the amplitude of the initial acoustic oscillation in baryon-photon fluid, etc. Three different types of experiments have conducted CMB observations: (i) Satellites, e.g. COBE, WMAP; (ii) Balloon-borne, e.g. BOOMEranG, MAXIMA, ARCHEOPS, QMAP; (iii) Ground-based, e.g. CAT, TOCO/MAT, Viper, ACBAR, DASI, CBI, Saskatoon, Tenerife.

In 1989 the Cosmic Background Experiment satellite (COBE) confirmed with FIRAS (Far Infrared Absolute Spectrophotometer experiment) that the distribution of energy of CMB was isotropic and fitted a blackbody curve described with a temperature of 2.725$\pm$0.0002 K, (Mather et al., 1990). The Differential Microwave Radiometer (3-10 mm, DMR) experiment on COBE also discovered a small signal of 30 μK fluctuations ($\sim$10 deg), (Bennett et al., 1996). This anisotropy is evidence of variations in density which would eventually evolve into galaxies, clusters and other larges structures. Finally, DIRBE (Diffuse Infrared

Background Experiment) mapped the entire sky at FIR wavelengths to extend the previous observations of the infrared Astronomy Satellite IRAS (1983). The Wilkinson Microwave Anisotropy Probe (WMAP) satellite was launched in 2001, with the mission to observe, with a resolution of ∼0.3 deg, and sensitivity of 20 μK per 0.3 square deg the CMB which showed temperature differences of $\sim 10^{-6}$ K (see Figure1.2).

Other evidence to support the suggestion of a cold and active Universe was provided by the IRAS satellite, which conducted an all sky FIR survey in 1983. Imaging the sky at 12, 25, 60, 100 μm (2 arcmin FWHM), IRAS detected ∼350,000 individual point sources, of which 75% were galaxies at low redshift z∼0.02 (Soifer et al., 1987). Whilst the majority were identified as late type spirals, IRAS also discovered a new population of luminous infrared starburst galaxies (LIRG's) with a monochromatic (60 μm) luminosities $L_{FIR} > 10^{12} L_{\odot}$. The combined FIR emission of these objects is larger than the total luminosity in all others bands, (Sanders & Mirabel, 1996). The energy distribution and luminosity is due to dust in the interstellar medium heated to 30 - 80 K by the optical-UV photons (i.e. attributed to the primary radiation from young massive stars forming at rates of >100 $M_{\odot}$/yr) and re-radiated into FIR region. IRAS confirmed the existence of the cosmic infrared background CIB (i.e. unresolved high-z objects). The CIB has a total energy density $\sim 40 \times 10^{-9}$ W/m^2/sr, compared with the optical background $(17 \pm 3) \times 10^{-9}$ W/m^2/sr (Franceschini, 2001), where 30% of the CIB energy density belongs to the local universe. The rest of this energy density could be attributed to a large population of isothermal objects distributed over a range of redshifts (z>1) with similar SED to those local objects called ultraluminous infrared galaxies (ULIRG's). A more precise measurement of the CIB was made by COBE/DIRBE (42 arcmin FWHM) which discovered that the CIB is isotropic. The IRAS survey was also used to determine the 60 μm galaxy luminosity function, (Saunders et al., 1990), which helps to constrain the evolution models of the starburst galaxy population in order to understand

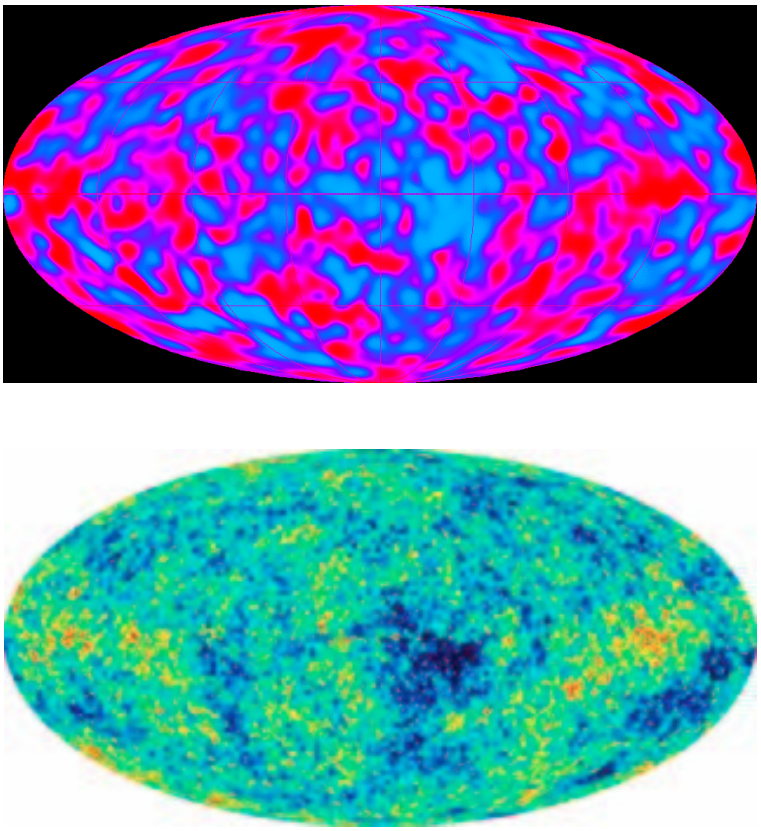

Figure 1.2: Top panel: The COBE image shows the reduced map (i.e., both the dipole and Galactic emission subtracted). The cosmic microwave background fluctuations are extremely faint, 10 μK compared to the 2.73 K average temperature of the radiation field. Bottom panel: The later WMAP image shows a higher resolution image of the CMB temperature fluctuations of $\sim$ 1 μK. The CMB radiation is a remnant of the Big Bang and the temperature fluctuations are evidence of variations in the density of the early universe. These density ripples are believed to have given rise to the largest structures that populate the universe today, i.e. clusters of galaxies and vast regions devoid of galaxies.

the spectral composition of the CIB.

Higher angular resolution studies were not made until the Infrared Space Observatory was launched in 1995. The three-year mission provided evidence that further supported a population of optically-obscured sources at high-z. The ISOPHOT (a 170 μm photometer) deep extragalactic survey (Far Infrared Background project, FIRBACK) detected sources as faint as $\sim$100 mJy, which contribute $\sim$10% (z$<$ 2) of the CIB (Puget et al., 1999). Therefore, an important result of the confirmation of the CIB is the fact that most of the star formation is produced in a heavily-obscured interstellar medium. Furthermore, due to a strong k-correction, sub-mm/mm wavelength observations are even more capable of providing information to trace the star formation evolution in dusty galaxies in the high-z Universe, (Hughes & Dunlop, 1999). For example, if a large population of ULIRG's (e.g. Arp 220, $L_{60} = 8.4 \times 10^{11} L_{\odot}$) are at z$>$ 1 then the strong negative k-correction at sub-mm/mm wavelengths will make their detection possible out to redshifts as high as z$\sim$10 (Blain et al. 2002, see Figure 1.3). The sub-mm/mm emission of local ULIRG's is also due mainly to dust, and it is well described by optically-thin thermal emission greybody with temperatures between 20 to 80 K. The greybody spectrum is due to the shape, size and composition of dust grains (i.e. small grains are unable to emit efficiently at wavelengths similar to or larger than their sizes, i.e. $\lambda \geq 2\pi a$).

Therefore, the rapid increase in our understanding of the high-z redshift Universe and the technological development of telescopes and receivers, operating at FIR-mm wavelengths, over the last few decades, the capability to detect of sub-mm/mm radiation from distant galaxies is one of the most important and recent developments in observational cosmology. The most successful sub-mm/mm extragalactic surveys have been conducted since 1997 with the Submillimetre Common -User Bolometer Array (SCUBA) on the 15-m James Clerk Maxwell Telescope (JCMT) on Mauna Kea, Hawaii. The SCUBA galaxy source-counts have been used to constrain the evolutionary history of dust-enshrouded star-

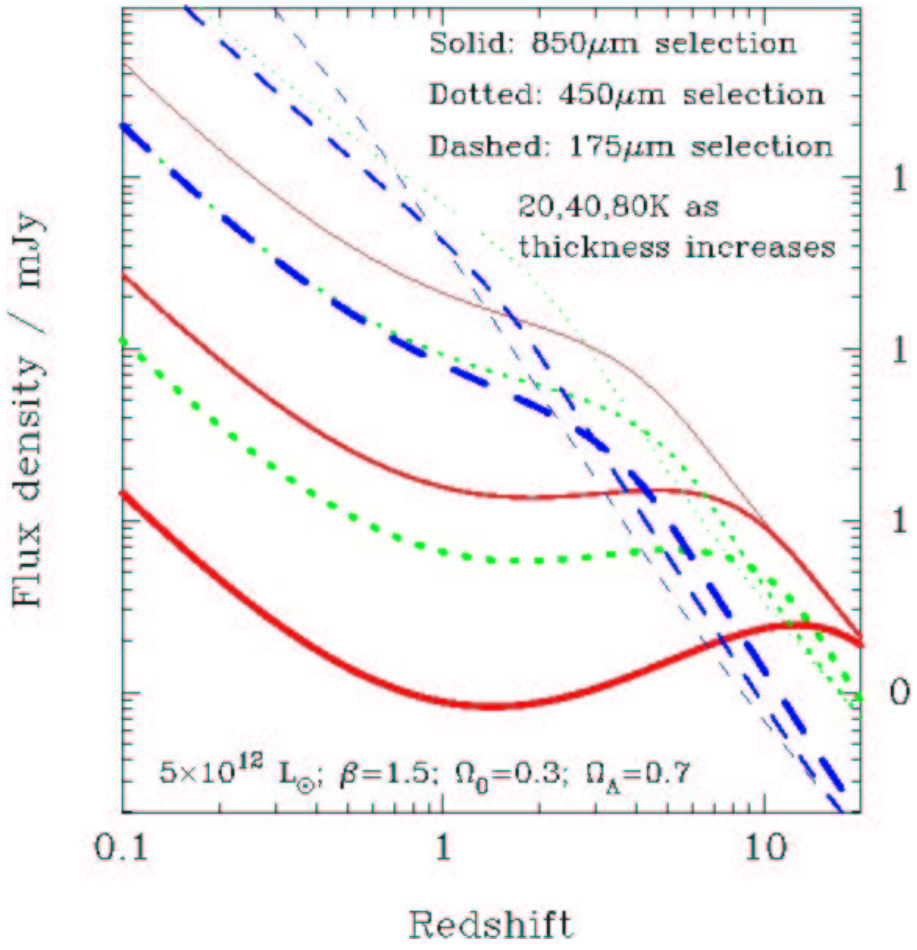

Figure 1.3: Flux density of a ULIRG (e.g. Arp 220) as a function of the redshift. The flux density is observed at wavelengths of 175, 450 and 850 μm, over a range of redshifts $z = 0.1 - 10$. The lines of different thickness illustrate 20 K, 40 K and 80 K SED temperatures. The graphs were made using a pure evolution model (i.e. 5×10^{12}, $\beta = 1.5$, $\Omega_o = 0.3$ and $\Omega_\Lambda = 0.7$). As the SED is redshifted, it becomes fainter, but the negative k-correction compensates for this dimming, and so the flux remains basically constant for $z \sim 1 - 8$ (e.g. at 850 μm wavelength). In the case of longer wavelengths or warmer SEDs, the k-correction increases the observed flux at higher redshifts.

burst galaxies at z ∼2 - 3, as well as the intensity of the background radiation at sub-mm/mm wavelengths (Smail et al., 1997; Hughes et al., 1998; Scott et al., 2002).

However, todate less than 1 sq. degree of the entire sky has been mapped at sub-mm/mm wavelengths, because the actual surveys are still restricted by the angular resolution, sensitivity and field-of-view. For example, SCUBA and MAMBO on the 30-m IRAM telescope, have mapped individual regions with areas of 0.002 - 0.2 sq degree and have resolved close to 20% of the total radiation at FIR wavelengths measured by COBE/DIRBE. A new generation of large format array cameras (SCUBA-II; ∼ 64000 pixeles) will allow one to significantly improve the mapping speed by fully-sampling the focal plane of the 15-m JCMT telescope in the near future. On the other hand, the small primary apertures of these existing sub-mm telescopes, limit the sensitivities of the source detections to an extra-galactic confusion limit of ∼2 mJy at 850 μm, with 15 arcsec resolution. A larger single-dish millimetre wavelength telescope will provide a greater gain in both sensitivity and resolution and, combined with large format-array cameras, will significally increase the mapping speeds. Therefore the 50-m LMT millimetre-wavelength observations will be extremely important in tracing the evolution of the star formation in dusty enviroments at high-z. For example AzTEC (Aztronomical Thermal Emission Camera) is one of the first-light instruments for the LMT. AzTEC uses a 144-pixel SiNi spider-web bolometer array operating at 1.1 and 2.1 mm, with a FOV of 2.4 sq. arcmin. Given the predicted AzTEC sensitivity (NEFD ∼ 3 mJy$^{-1/2}$ per pixel at 1.1 mm), and a mapping-speed of ∼ 0.3 deg^{2}hr^{-1}mJy^{-2} on the LMT, as well increasing the high angular resolution, AzTEC and the LMT will reduce the measured extragalactic confusion limits. This will make it possible to resolve a significant increased fraction (90 - 100%) of the mm-FIR wavelength background into individual point sources (i.e. $L_{FIR} > 10^{11} L_{\odot}$). In addition, the large-scale structure of the Universe will be studied with the LMT by conducting observations of clusters via the

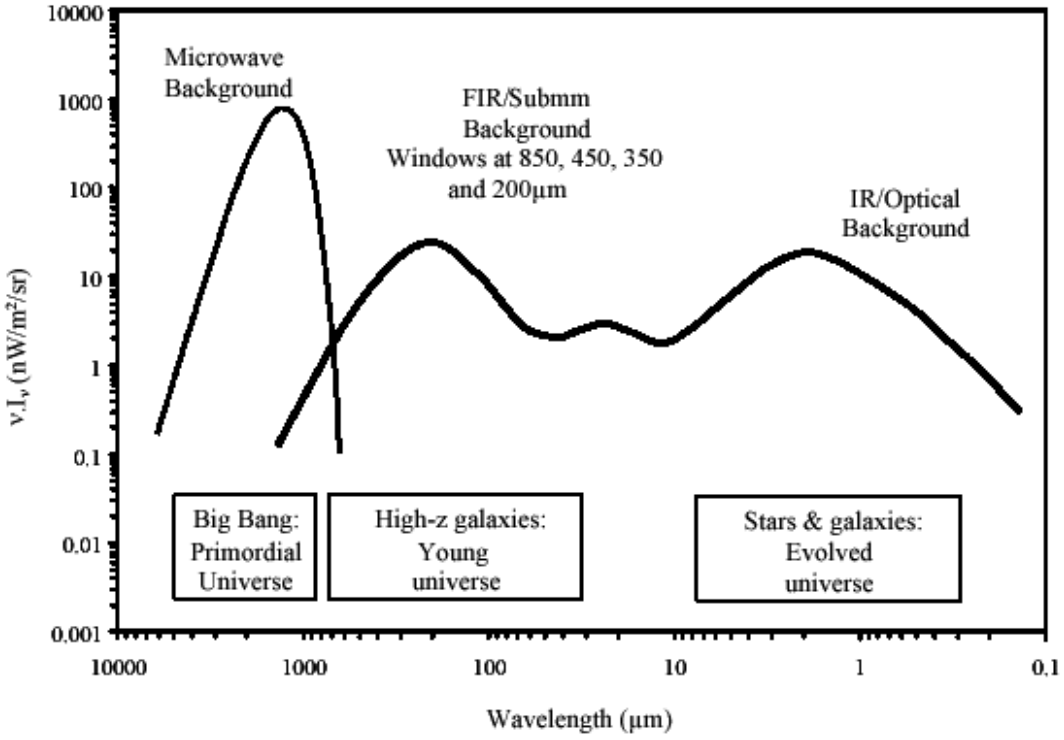

Figure 1.4: The three main components of the extragalactic background spectrum. The dominant component is the *microwave* background at millimetric wavelengths given by the primordial Universe at the epoch of recombination. The second component is the FIR/sub-mm/mm background produced by galaxies in the young Universe, and finally the third component is the IR/optical background due to the light coming from stars, galaxies and AGN in the evolved Universe. (Busswell & Shanks, adapted by Holland et al. 2004)

Sunyaev-Zeldovich effect, with AzTEC observing at both 1.1 mm and 2.1 mm the increment and decrement of the S-Z signature, (Hughes, 2005). Therfore, having motivated and justified the many opportunities to conduct exciting scientific projects at FIR-millimetric wavelengths, in particular with the LMT, we now describe the unavoidable impact of the atmosphere on ground-based millimetric wavelengths observations.

1.3 Ground-based observations at sub-mm/mm

Despite the growing importance of the sub-mm/mm astronomy in understanding the evolution and growth of the structure in the Universe, it is currently only practical to make the majority of these observations from ground-based observatories. At sub-mm/mm ($\sim$ 4 mm - 300 μm), the atmosphere is partially transparent. In this region there is absorption and emission from a variety of molecules (CO, NH_3, HCl, etc ...). There are windows of excellent transmission between $\sim$50 GHz and 300 GHz, but these still include some features from H_2O and O_2. With the exception of two wide windows at 650 GHz and 850 GHz, however, the atmosphere is completely opaque at higher frequencies until one reaches the mid infrared ($\sim$10 THz). This high atmospheric opacity is due to water molecules and dioxide of carbon and ozone. In addition, a pseudo-continuum with both wet and dry components contributes to the atmospheric absorption. This pseudo-continuum is stronger at higher sub-mm frequencies.

The atmospheric transparency is one of the most important features when choosing a telescope site. The atmospheric opacity produces a reduction in signal strength by the absorption, and therefore longer integration times are required to reach the desired signal-to-noise ratio. Also the atmospheric stability will produce phase delays on the incoming signal. This is produced by the non-uniform distribution of the atmospheric water vapor, due to imperfect mixing. The water vapor moves in layers creating a turbulent cells which impose a limit for interfer-

ometric observations. In addition, time fluctuations on the sky temperature due to the water vapour are an important source of sky-noise for ground-based observations. Atmospheric models are helpful in conjunction with observational data programs to study the strategies for site characterization (Surtees, 1991). Models of the atmospheric spectrum were first presented by van Vleck (1947a,b). The current favored model is the Atmospheric Transmission Model, (ATM) (Pardo et al. 2001). These models depend on the physical parameters, such as barometric pressure or site altitude, surface temperature and amount of water (PWV) (see Figure 1.5). In ground-based observations, beyond the issue of site-selection, it is helpful to characterize the site before the first observations begin in order to plan the observatory operations. Both temporal and spatial atmospheric characterization are necessary and typically involve measurements of opacity, PWV and sky stability. Previous knowledge of the sky behavior will also help in the design of the electronic systems (control and readout) for the next generation of detectors, for example those based on superconductors materials (superconducting transition-edge sensors, TES). Therefore removing the effect of the atmospheric water-vapour is the major challenge in ground-based sub-mm/mm observational astronomy. One way to minimize the water-vapour problem is to build observatories in high and dry sites, where atmospheric water content is small or ideally, ignoring the financial implications, telescopes on balloon-borne or satellite platforms. The next sections will describe briefly some atmospheric properties and characteristics, and some of the methods to study the atmosphere that ultimately motivated our decision to build a FTS system.

1.4 The atmosphere

The Earth is surrounded by gases that we call *atmosphere*. The atmosphere is a mix of gases (air) formed by nitrogen (79%), oxygen (20%) and other gases (1%). The atmosphere is dived into many layers. Strong correlations exist be-

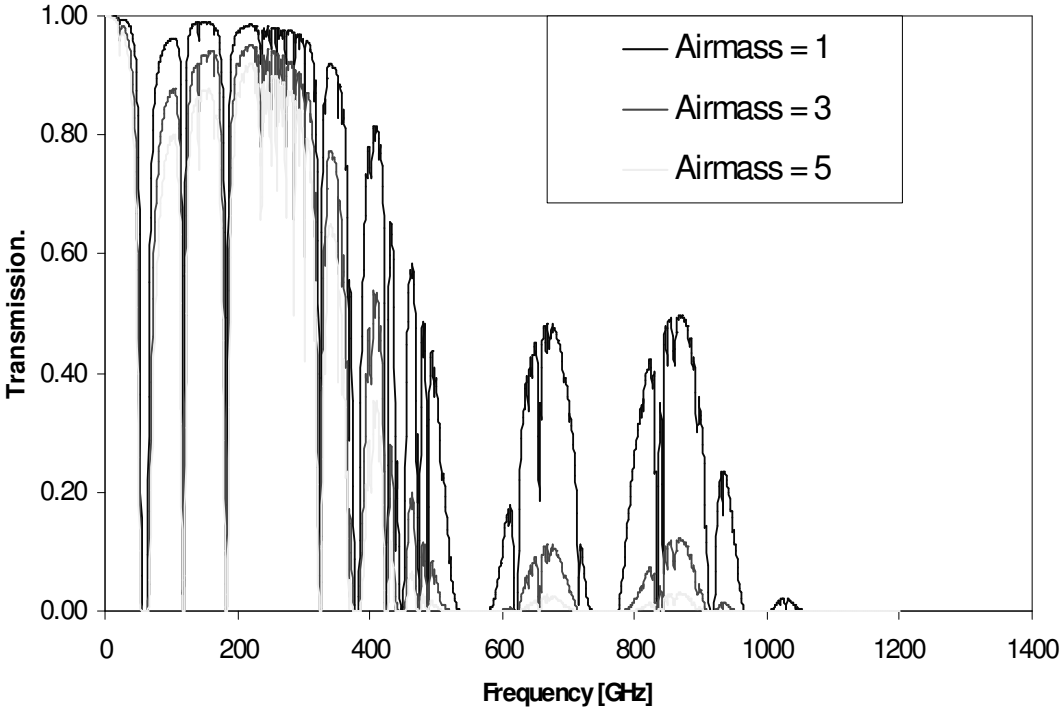

Figure 1.5: Synthetic atmospheric spectrum of the sky at La Negra for 1 mm PWV (using the ATM code).

tween physical properties (i.e. temperature, pressure, density, etc.) and altitude. This natural stratification of the atmosphere is illustrated in figure 1.6. The *troposphere* extends from the Earth's surface to nearly 8 km (Earth's poles) and 18 km (equator). Three-quarters of the Earths's air is contained in the troposphere, along with the nearly all the water-vapour and atmospheric particles and includes 70% of the total atmospheric weight. Also all the weather phenomena occur in this layer. The water vapour and particles decrease exponentially with altitude and the rate temperature change is 6.5 K/km. Most of the astronomical observatories take advantage of this behavior. The *stratosphere* is a layer that lies above 11 km to 50 km with no water-vapour and the temperature is quite uniform (218.15 K - 233.15 K). Oxygen is present in a triatomic molecule (ozone 0_3) which is the main absorber of UV radiation. In the stratosphere the ozone is both produced and destroyed by photochemical processes. The greatest concentration of ozone is found at an altitude of 22 km. The *mesosphere*, extends from 50 km to 80 km and the temperature decreases again to 183.15 K at about 80 km. Next is the *ionosphere* at an altitude of about 500 km. The ionospheric molecules are ionized and dissociated and the temperature in the ionosphere is $\sim$1280 K. Above 500 km is the *exosphere* which is a rarified environment in which molecules seldom collide and frequently they escape into space.

1.5 Water vapour absorption

The abundance of water-vapour is highly variable. It is quite abundant in the atmosphere but hardly exceeds 1% in mass. The water diffuses into the air by evaporation. It is transported by wind and convection processes. The amount of columnar water is as variable as the weather itself. The atmospheric water can exist in three different phases (liquid, solid and gas). The water liquid is mostly located in low and middle layers in the form of vapour. Even inside the clouds, precipitation and turbulence ensure that the mass of water droplets per cm^{-3}

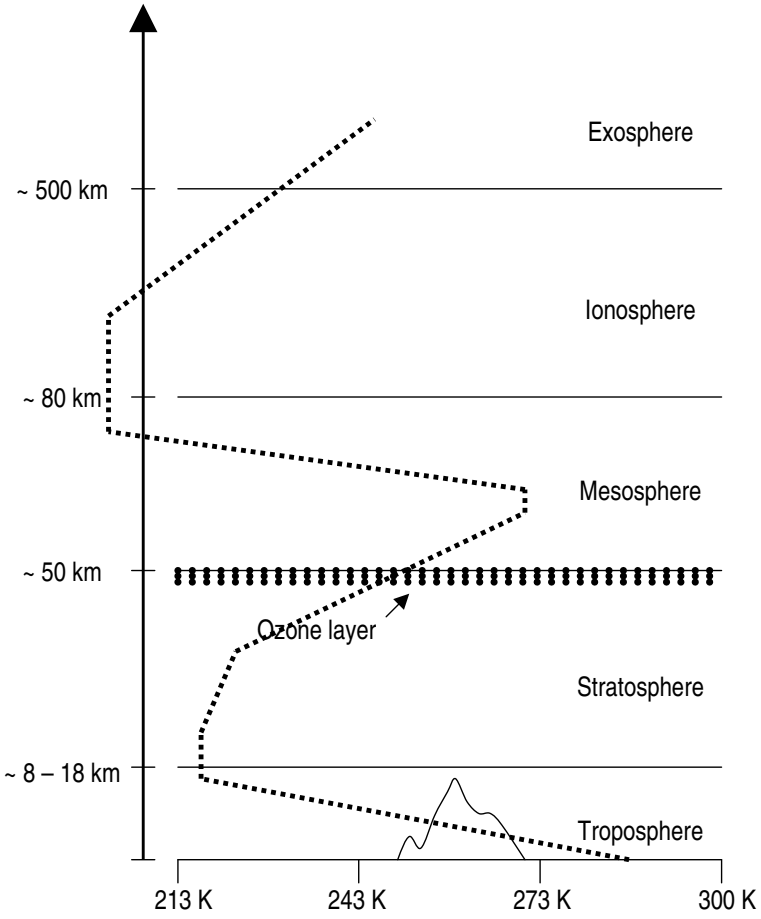

Figure 1.6: Stratification of the Earth atmosphere showing the change in temperature (K) with the increasing altitude (km).

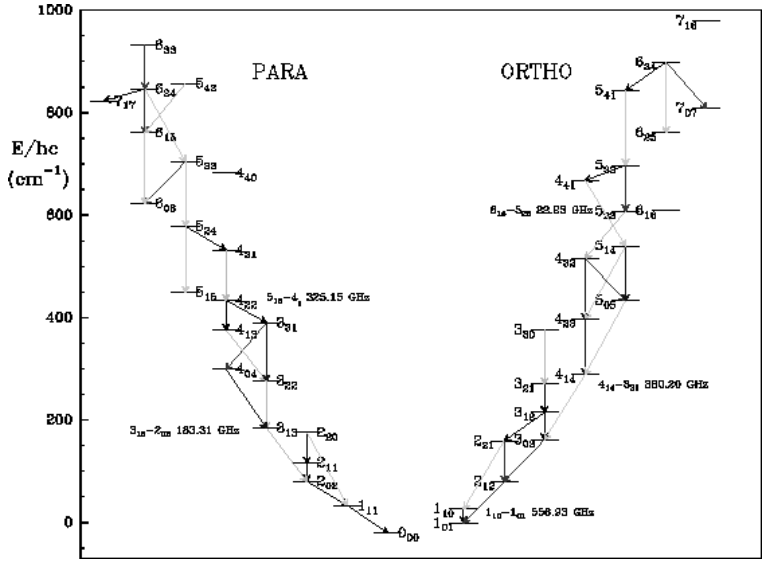

Figure 1.7: Rotational energy level diagram for water-vapour (Guélin, 1998).

seldom equals that of water-vapour. The amount of water-vapour in an air parcel could be expressed by the amount of liquid water that would be produced when all the vapour is condensed, often measured in mm of precipitable water (PWV).

The major contributions to the atmospheric opacity are the molecular rotational transitions of H_2O, O_2 and O_3. The oxygen has a magnetic dipole with a strength 10^2-10^3 times weaker than the water transitions. Oxygen is more abundant ($\sim$ 21%) than water, and so the lines of oxygen and water have similar intensities, (Guilloteau, 2000). Oxygen on the other hand, is well mixed and decreases exponentially in concentration with the increasing altitude. Ozone has 2800 weak transitions, and it has significant opacity above 230 GHz (Surtees, 1991).

Water is a triatomic asymmetric molecule that presents a permanent dipole moment, and therefore a pure rotation spectrum. Figure 1.7 shows the rotational energy level diagram for water-vapour. The water-vapour shows five strong lines between 10 GHz to 500 GHz, (22 GHz, 183 GHz, 325 GHz, 380 GHz and 425

GHz). Above 500 GHz water-vapour emits strongly and produces an optically-thick atmosphere that radiates with power $> 10^6$ times stronger than the typical astronomical sources at sub-mm/mm wavelengths.

1.6 Measuring the atmospheric transparency

The opacity and atmospheric instability effects are important for the sub-mm/mm wavelength range. Observations at wavelengths < 2 mm are more affected by the atmospheric conditions and only a few sites in the world offer acceptable conditions for sub-mm/mm astronomical observations, including the LMT site Sierra La Negra.

1.6.1 Radiometers

Astronomical observations under high opacity conditions are futile due to the fact that astronomical radiation can not penetrate the atmosphere. The opacity over sub-mm/mm wavelength range is highly correlated with the amount of atmospheric water-vapour, so a potential site for sub-mm/mm observatory will be a dry site at very high altitude.

A common method to measure the opacity is by means of a tipping radiometer. Typically there are two types; single-line and broad-band window. Tipping radiometers directly measure the total atmospheric opacity (adding all the contributions from all the atmospheric components) at wavelengths close to the wavelengths of the bandpasses in which the observations are being made. The atmospheric opacity is measured by using a tipping mirror in order to measure the sky temperature at different elevations (e.g. 215 GHz INAOE radiometer, Torres et al. 1997; Estrada et al. 2002), and a linear relation between the measured power as function of the airmass is then fitted to these data. Currently 200-225 GHz tipping radiometers are standard for site characterization at sub-mm/mm

wavelengths. A single-line radiometer measures the total power in a single-line, for example at 22 GHz or 183 GHz which lie within the frequency range of strong water emission lines. The opacity is then obtained from the amount of water by means of atmospheric models, describing the water line-profile (Delgado et. al., 1999).

Tipping radiometers are relatively simple to construct and operate (i.e. no strict support is required), and they are suitable for long-term monitoring campaigns. The disadvantage is that they only measure the opacity at a single wavelength or in a broad-band window. More detailed atmospheric information over a wide-band (e.g. $\sim$ 200 GHz - 2 THz) can be performed by spectroscopic methods. Wide-band radiometers are more complex and they usually require cryogenic cooling, as well as a more elaborate optical system. Alternatively Fourier Transform Spectrometers (FTS) covering all the sub-mm/mm range, offering detailed atmospheric spectra of the site, and have been extensively used in South Pole (Chamberlin et al., 2003), and Pampa La Bola, Chile, for example (Matsuo et al., 1998; Matsushita et al., 1999, 2000).

1.6.2 Interferometers

In the sub-mm/mm wavelength range, temporal variations in the amount of atmospheric water-vapour cause sky instability. Because the astronomical radiation travels more slowly through cells of water-vapour than through the dry air, fluctuations in the water-vapour content will produce variations in the phase of the detected astronomical radiation. The main consequences of these fluctuations are: (i) loss of resolution and (ii) attenuation of the intensity of the astronomical radiation.

Interferometers are useful to simultaneously measure the sky stability (phase/ brightness fluctuations), as well as atmospheric opacity. Whilst atmospheric stability is not as fundamental as transparency for a site characterization, it is important for observations of the faintest point sources and the extended cosmic microwave background. Experiments to measure the anisotropy of the CMB at small angular scales ($<$ arcmin) are the most affected by these fluctuations. For sub-mm/mm interferometry, the instability causes phase fluctuations and also produces lower resolution observations. Measuring the phase fluctuations directly with an interferometer, by observing a convenient beacon outside the atmosphere, i.e., on a geostationary satellite, can correct the phase (Ishiguro et al., 1990). Inhomogeneities in the atmospheric water-vapour distribution also produce fluctuations in the sky brightness that have been measured by interferometers, (Lay & Halverson, 2000). Differential measurements are usually employed to minimize the effects of the sky instability: (i) chopped-beam instruments measure the difference in emission between two or more directions on the sky, e.g. Python I-IV: (Dragovan et al., 1994; Ruhl et al., 1995; Platt et al., 1997; Kovac et al., 1997), (ii) swept-beam instruments sweep a beam rapidly backward and forward $\sim$5 Hz, e.g. Python V: (Coble et al., 1999); Mobile Anisotropy Experiment: (Torbet et al., 1999). Both techniques efficiently reduce the noise from rapid sky-fluctuations. A similar chopping (sky-subtracting) strategy is also used

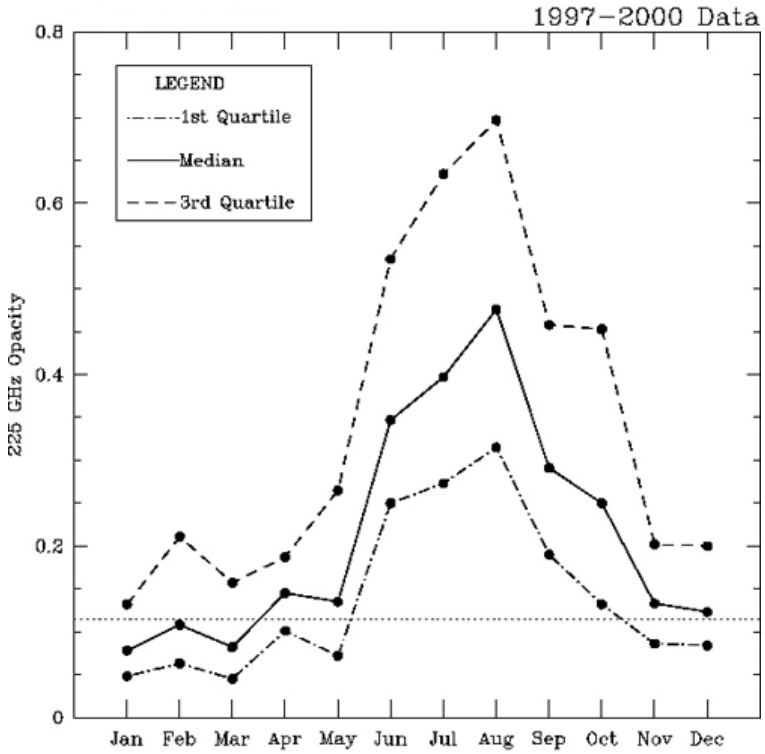

Figure 1.8: 215 GHz opacity for the LMT site, measured during 1997-2002. The best season for sub-mm/mm observation are from November through May with opacity values < 0.2. Data reduction by Microwave Laboratory, INAOE

for single-dish experiments using single-pixel and large feed-horn coupled arrays.

1.7 LMT site characterization with a FTS

Since 1999, there has been construction on Sierra La Negra to build a single-dish large-aperture sub-mm/mm telescope ($\sim$ 50 m) at an altitude of 4600 m. The opacity of the site has been measured with water-vapour tipping radiometers at 215 GHz during 1997 - 2005 (Torres et al., 1997; Estrada et al., 2002). Sierra La Negra is a sub-mm/mm site during a large fraction of the year (November through May) when the opacity τ_{215GHz} is around 0.2 or less (third quartile, see Figure 1.8). However, the characterization of the atmospheric transparency and stability of the LMT site has only been made with narrow-band radiometric methods at 215 GHz (Torres et al., 1997; Estrada et al., 2002). This information just reflects the narrow-band behavior of the sky, and a better understanding of the atmospheric behavior is needed in order to understand the broad-band characteristics since continuum detectors are commonly used at sub-mm/mm wavelengths (i.e bolometers array, AzTEC, SPEED). The operational band of a bolometric camera is defined by the available atmospheric windows (e.g. 2.1 mm, 1.1 mm, 850μm: see Figure 1.5), and the optical filtering within the camera. In practice, however the optical bandpass filters are designed to closely match the atmospheric windows. This maximizes the sensitivity whilst minimizing the impact of a variable sky emission.

Also, the sky stability has a strong influence on the design of the readout electronics, because the change in the optical background can produce changes in sensitivity and overloading on the detector system. It is not only the broadband systems that need atmospheric information, but also the heterodyne systems (i.e. SEQUOIA, Z-machine, etc) which will work over a wide range of frequencies, $70 - 115$ GHz, and hence are also affected by the sky conditions. Figure 1.9 illustrates the atmospheric modeled transmission from Sierra La Negra over a range of $50 - 400$ GHz showing the atmospheric behavior for summer and winter seasons. The atmospheric transmission was calculated from measurements of

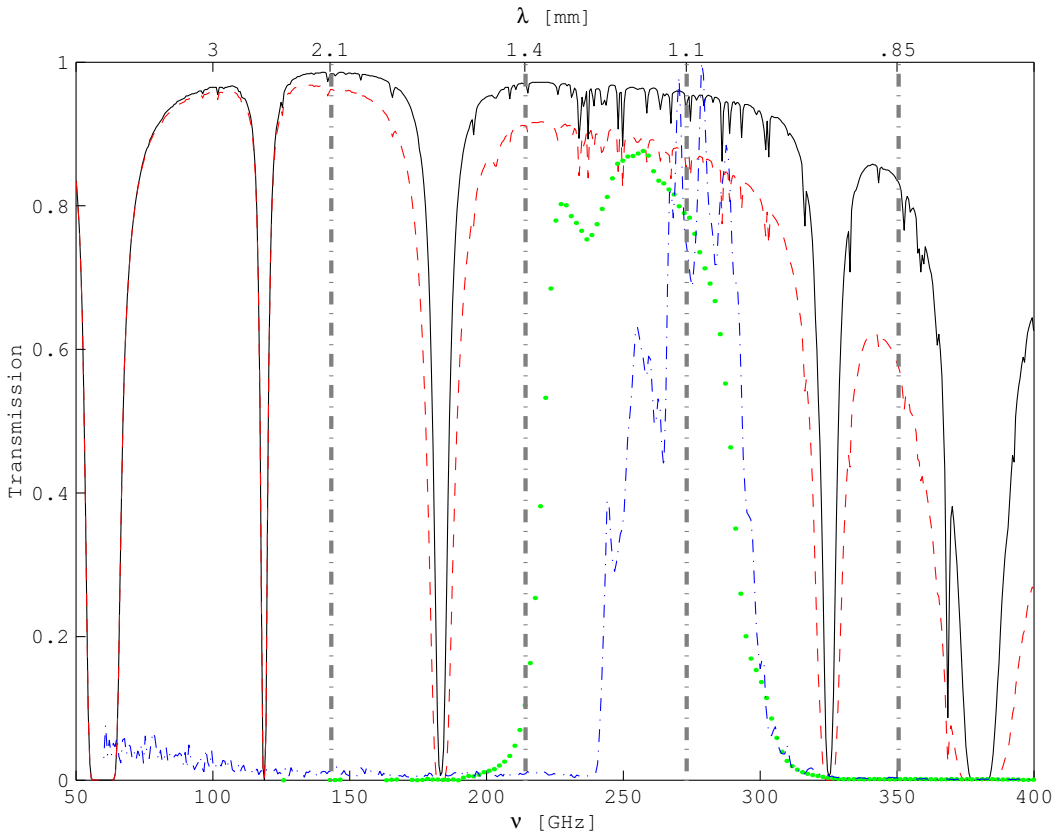

Figure 1.9: Simulated atmospheric transmission spectrum for the LMT site. The black solid-line and red dashed-line illustrate the atmospheric model for winter and summer mean opacity respectively (1997-2004). The blue dot-dashed line is the measured AzTEC bandpass ($\sim$ 1.1mm). The gray dot-dashed lines illustrate the central frequency bandpasses of the SPEED camera (SPEctral Energy Distribution camera)

the mean opacity, base temperature and local pressure for the respective season. Also, shown in figure 1.9 are the transmission characteristic of the AzTEC filter at 1.1 mm, which is not contaminated with any water-emission lines (that occur at 183 and 325 GHz, which define the wider sub-mm/mm window). Extensive broad-band observations of the atmospheric transmission above the LMT site, derived by the FTS system described in this thesis, can guide the future instruments developments for the LMT. Also, the FTS system will provide information about the percentage time of open atmospheric windows and the guidelines for the design of the broad-band filtering, allowing us to optimize the observation operations throughout the year. Therefore, an FTS system developed at INAOE will be a powerful complementary instrument for a continuous site characterization program. Furthermore by optimizing the design of the first instruments, the LMT will play a leading-role in the coming decades in the investigations into the formation and evolution of the structure at all epochs.

1.8 Millimetre Instrumentation Laboratory

The MI-Lab was created to design and build instruments for the site characterization, scientific experiments, as well as to provide support to the LMT instruments by forming the necessary human resources through the technical training of students. In order to design, build and integrate the cryogenic FTS system as part of this development, we first had to establish the suitable working space for a laboratory and set up all the necessary infrastructure in the MI-Lab, (see Figure 1.10). Currently, we are able to conduct cryogenic experiments at temperatures of 4.2 to 1.5 K under moderate vacuum levels $\sim 10^{-5}$ mbar.

The basic equipment of the laboratory includes: vacuum pumps and spares (i.e. fittings, hoses, valves, etc.), cryogenic (L^4He, LN_2) storage dewars, thermometry systems and sensors, cryostat, detectors, filters, optics, electronic equipment, etc.

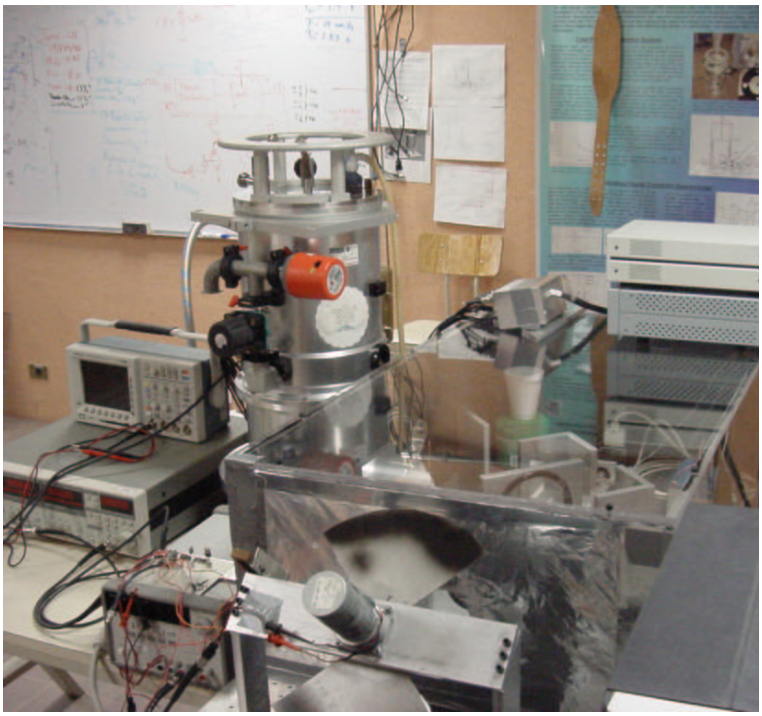

Figure 1.10: Fourier Transform Spectrometer in the MI-LAB, INAOE, showing the FTS-MPI (front-right), the cryostat (back-left) and associated electronics.

1.9 Objective of the thesis

At the start of this effort to build and develop experience in sub-mm/mm wavelength instrumentation at INAOE, we asked a few straight-forward questions. Is it possible to characterize the atmospheric conditions of the sky for LMT site in the sub-mm/mm range by building at INAOE a cryogenic Fourier Transform Spectrometer, instead of buying a commercial one? Is a Fourier Transform spectrometer a suitable instrument for the purpose of characterizing the atmosphere above Sierra La Negra? It is possible to use a cryogenic composite bolometer operating temperatures above 1 K in order to make measurements over the sub-mm/mm range? In order to answer the above questions, we proposed to design and construct a Fourier transform spectrometer using a single-pixel cryogenic camera, based on a composite bolometer operating at temperatures < 2 K. The composite bolometer uses a NTD Ge thermistor type-B from Haller-Beeman Inc. and uses NbTi electrical leads which would allow us to measure radiation levels as low as 10^{-12} W. The advantage of the NbTi wires is that they reduce the thermal conductance by a factor $\sim$100 compared to brass, and by a factor of $\sim$1000 compared to copper at cryogenic temperatures as low as 1.8 K. The final working temperature of the system is $\sim$ 1.8 K (under vacuum), which provides an expected thermal conductance close to 1×10^{-10} W/K, allowing the system to work with backgrounds of about 10^{-12} W. The responsivity of the detection system is 3×10^{6} V/W and the NEP is 1.26×10^{-13} W/Hz$^{1/2}$. In order to have a compact system we decided to adopt a medium-throughput system (i.e. $\sim$ 8.9 cm, $\sim f/4.7$) and a small linear stage (i.e. 18 cm) without sacrificing the spectral resolution. The FTS-MPI system allows us to measure a broad-band spectrum in the 215 - 1000 GHz frequency range with a resolution from 10 GHz - 500 MHz. As an important secondary goal, the FTS could provide detailed (high-resolution) measured atmospheric spectra for comparison with models (e.g. ATM), and allow us to set up a continuous program of site characterization and monitoring

with the following objectives: (i) to identify and quantify the site conditions and their influence on the design and operation of the current, as well as the future instruments; (ii) to provided historical records of the site conditions to guide the efficient future operation of the LMT observatory (i.e flexible queue scheduling, engineering maintenance periods, etc.).

The present work also deals with the development of a methodology for the design and integration skills, that will lead to the development of future sub-mm/mm astronomical instrumentation at INAOE in México.

One important factor is the experimental quantification of the thermal properties of the NbTi wires, which were expected to have a suitable behavior for operational temperatures lower than 2 K, but for which insufficient data existed in the literature prior to this decision. Finally we developed a complete Fourier transform spectrometer that operates at sub-mm/mm wavelengths, that includes the optics which were completely fabricated at the INAOE facilities.

1.10 Thesis Outline

The design of FTS-MPI system is described in this thesis, which is part of the first instrumentation projects conducted by the MI-Lab at INAOE. The basic Fourier transform spectroscopy, based on a polarizing Martin-Puplett interferometer, is reviewed in Chapter 2, as well as a brief discussion about using a bolometric camera as part of the FTS-MPI. The detection system is based on cryogenic bolometer, and the basic theory is reviewed in Chapter 3. The design of the bolometer, optical coupling, cryogenic system, readout electronics and the performance analysis is developed in the Chapter 4. The design of the FTS-MPI, as well as the integration of the system is described in Chapter 5, and in addition we discuss the data reduction method and first results from the laboratory tests. In Chapter 6, the final conclusions and the summary of the result of this project are presented. A discussion of the modifications to the system in order

to provided an operational spectroscopic instrument, installed at the LMT are, also presented as part of the future work.

Chapter 2

Fourier Transform Spectrometry: FTS

This chapter deals with the theory of Fourier transform spectroscopy, and the Fourier transform method of interference spectroscopy via which a spectrum can be recorded and analyzed. The basic properties i.e apodization, interferogram sampling and spectrum computation are discussed in order to understand the performance of the Fourier spectrometer. The spectroscopic process can be divided into two main parts: the first, the recording of the interferogram; and the second, the computation of the spectrum from the Fourier-transform of the interferogram. The discussion is then extended to the design of our FTS system at INAOE, based on the Martin-Puplett interferometer which is widely used for far-infrared experiments and astronomy studies.

2.1 Interference Spectroscopy

A spectrometer is an instrument that separates the continuous radiation from the electromagnetic spectrum into individual higher resolution measurements (spectra). There exist several types of spectrometers, each used in different research fields. Generally a spectrometer works over a small fraction of frequencies in the electromagnetic spectrum. The spectrometers are mainly divided in two categories: (i) Dispersing spectrometers (e.g. prism spectrometer, diffraction spectrometer); (ii) interference spectrometers (e.g. two-beam interferometer, multi-beam interferometer).

The dispersing interferometers or diffraction gratings, spatially separate the individual frequency components (monochromators) of the incoming radiation. Each frequency component is selected by a slit and measured with a suitable detector. The final spectrum is obtained after measuring all the frequency components of interest. The main drawback is their slow scanning process when used as a monochromator. In comparison the interferometric method uses an interferometer which divides the incoming radiation into two or more paths (i.e. multi-beam systems) and then recombines the beams after a phase delay has been introduced into one of the beams. This delay produces an interference pattern which is detected and recorded. The recombined signal is called an interferogram, which is the Fourier Transform of the power spectrum of the incoming radiation. Therefore, the inverse Fourier Transform of the interferogram will yield the original power spectrum. The main drawback in Fourier transform spectroscopy comes from the post-observation mathematical process which can introduce errors into the final computed spectrum. Methods to reduce the impact of these errors are discussed.

2.1.1 Two beam interference

Mathematically the interference could be explained as simply the superposition of two scalar waves. The nature of the light is vectorial (electric and magnetic fields are both vectorial). The electric field **E** at any point in space could be represented by the combined fields $\mathbf{E}_1$,$\mathbf{E}_1$,**...**, from different sources,

$$E = E_1 + E_2 + \cdots \tag{2.1}$$

Since the electric field varies too fast, a better quantity to measure by a variety of detectors such as the bolometers, is the radiant flux density **S**. The radiant flux density is defined as,

$$I = \langle S \rangle = \epsilon \upsilon \left\langle E^2 \right\rangle \tag{2.2}$$

where the term in brackets is the squared time-average magnitude of the intensity of the electric field. Now we consider a beam of radiant energy divided into two parts. Those two beams superpose at a point **Q** after travelling different paths. Let $\hat{E}_1(t)$ and $\hat{E}_2(t)$ be the analytic representation of the beams. Each beam is represented at **Q** as $\hat{k}_1\hat{E}_1(t-\theta_1)$ and $\hat{k}_2\hat{E}_2(t-\theta_2)$, where θ is the time delay and $\hat{k}$ is a geometric factor. The superposed beams can be expressed as a vectorial sum,

$$\hat{E}(t) = \hat{k}_1\hat{E}_1(t-\theta_1) + \hat{k}_2\hat{E}_2(t-\theta_2), \tag{2.3}$$

using the expression for the radiant flux with the Eq.(2.3) we get

$$I = \left\langle \hat{E}(t)\hat{E}(t)^* \right\rangle,$$

$$\begin{aligned} \text{where} \qquad \hat{E}(t)\hat{E}(t)^* &= \hat{k}_1\hat{k}_2\hat{E}_1(t-\theta_1)\hat{E}_1^*(t-\theta_1) \\ &+ \hat{k}_1\hat{k}_2\hat{E}_2(t-\theta_2)\hat{E}_2^*(t-\theta_2) \\ &+ \hat{k}_1\hat{k}_2^*\hat{E}_1(t-\theta_1)\hat{E}_2^*(t-\theta_2) \\ &+ \hat{k}_1^*\hat{k}_2\hat{E}_1^*(t-\theta_1)\hat{E}_2(t-\theta_2). \end{aligned} \tag{2.4}$$

The first and the second terms of Eq.(2.4) are the radiant flux densities at **Q** without any interference. The third and fourth terms are the complex conjugates of each one, such that their sum is

$$2\left|k_1k_2\right|\Re\left\{\hat{E}_1(t-\theta_1)\hat{E}_2^*(t)\right\}. \tag{2.5}$$

Using Eq.(2.5), and the fact that $I_1(t) = \left\langle \hat{E}_1(t)\hat{E}_1(t)^* \right\rangle$, $I_2(t) = \left\langle \hat{E}_2(t)\hat{E}_2(t)^* \right\rangle$ and that $\hat{k}\hat{k}^* = |k|^2$, then $I(t)$ at **Q** is,

$$I(t) = |k_1|^2 I_1(t) + |k_2|^2 I_2(t) + 2\left|k_1k_2\right|\Re\left\langle \hat{E}_1(t-\theta_1)\hat{E}_2^*(t)\right\rangle \tag{2.6}$$

2.1.2 Frequency information

The frequency information is contained in the interference pattern. The quantity $< \hat{E}_1(t-\theta_1)\hat{E}_2^*(t) >$ in the third term of Eq. 2.6 is the mutual coherence of the two beams. This term is a cross-correlation function from which we obtain the cross-power spectrum by taking the Fourier transform. We can express the mutual coherence as,

$$\hat{C}_{12}(\theta) = \hat{\Gamma}_{12}(\theta) \tag{2.7}$$

If the two beams came from the same source in such way that $\hat{E}_1(t) = \hat{E}_2(t)$ we get the auto-correlation function of the source. Therefore the Fourier transform gives the power density spectrum denoted by $\hat{B}(\nu)$:

$$\hat{B}(\nu) = \int_{-\infty}^{+\infty} \hat{C}_{11}(\theta) exp(-2\pi i\nu\theta)\, d\theta \tag{2.8}$$

Using the inversion theorem,

$$\hat{C}_{11}(\theta) = \int_{-\infty}^{+\infty} \hat{B}(\nu) exp(2\pi i \nu \theta)\, d\nu \tag{2.9}$$

Realizing the following substitutions to put these equations (2.8,2.9) in terms of the path difference and wavenumber,

$$\begin{aligned} \theta &= \delta/c, \\ \nu &= \sigma c, \\ \hat{C}_{11}(\theta) &= \hat{I}(\delta), \\ \hat{B}(\nu) &= \hat{I}(\sigma). \end{aligned}$$

we obtain expressions

$$\hat{I}(\delta) = \int_{-\infty}^{+\infty} \hat{I}(\sigma) exp(2\pi i \sigma \delta)\, d\sigma \tag{2.10}$$

$$\hat{I}(\sigma) = \int_{-\infty}^{+\infty} \hat{I}(\delta) exp(-2\pi i \sigma \delta)\, d\delta \tag{2.11}$$

The expression in Eq. (2.10) is the auto-correlation of the source, and it is a function of the path difference δ. Therefore, recording the interferogram and taking the Fourier transform, we can obtain a computed source spectrum.

2.1.3 The finite retardation and apodization

The computed spectrum is not a perfect representation of the true spectrum, since the interferogram is not measured over an infinitely long path-difference, and hence the result is a truncated interferogram. Mathematically this truncation can be expressed as the result of the complete interferogram multiplied by a truncation function $D(\delta)$ defined as,

$$\begin{aligned} D(\delta) &= 1 \qquad |\delta| < L \\ &= 0 \qquad |\delta| \geq L, \end{aligned} \tag{2.12}$$

where L is the maximum retardation. The product of two functions, say $D(\delta)$ and $\hat{I}(\delta)$, is the convolution of the Fourier transform of each function. Consequently, the computed spectrum is the true spectrum convolved with the Fourier Transform of the truncation function. The Fourier Transform of $D(\delta)$ is the sinc function:

$$\mathcal{F}\left[D(\delta)\right] = 2L\frac{sin(2\pi\sigma L)}{2\pi\sigma L} = 2Lsinc(2\pi\sigma L). \tag{2.13}$$

When the sinc function is convolved with a single narrow feature of the true spectrum, the result is the sinc function centered at the wavenumber σ_1, hence the narrow spectral line is smoothed (see Fig. 2.1). The two first zeros of the sinc function occurs at $\sigma_1 \pm 1/2L$. Thus two spectral lines separated by $1/L$ are completely resolved. The above is the basic definition of the spectral resolution, and is given by the maximum path difference in the interferogram. The truncation function $D(\delta)$ has a sudden cutoff which introduces side-lobes near sharp spectral features. This process, known as apodization, reduces the side-lobes, but sacrifices the result resolution given by L.

2.1.4 Computation of the spectrum

The expression 2.11 is the density power spectrum, and 2.10 is the autocorrelation function defining the square of the amplitude function; i.e. $|\Phi|^2 = I(\delta)$, and therefore

$$\hat{I}(\sigma) = \int_{+\infty}^{-\infty} |\Phi|^2 \, exp(-2\pi i\sigma\delta)\, d\delta \tag{2.14}$$

Since $|\Phi|^2$ is the product of a function times itself, the Fourier transform is the convolution of the Fourier transform of the function with itself. The calculation of the spectrum from a sampled interferogram can be performed by a Fourier series approximation or in a more convenient way, by taking the inverse Fourier

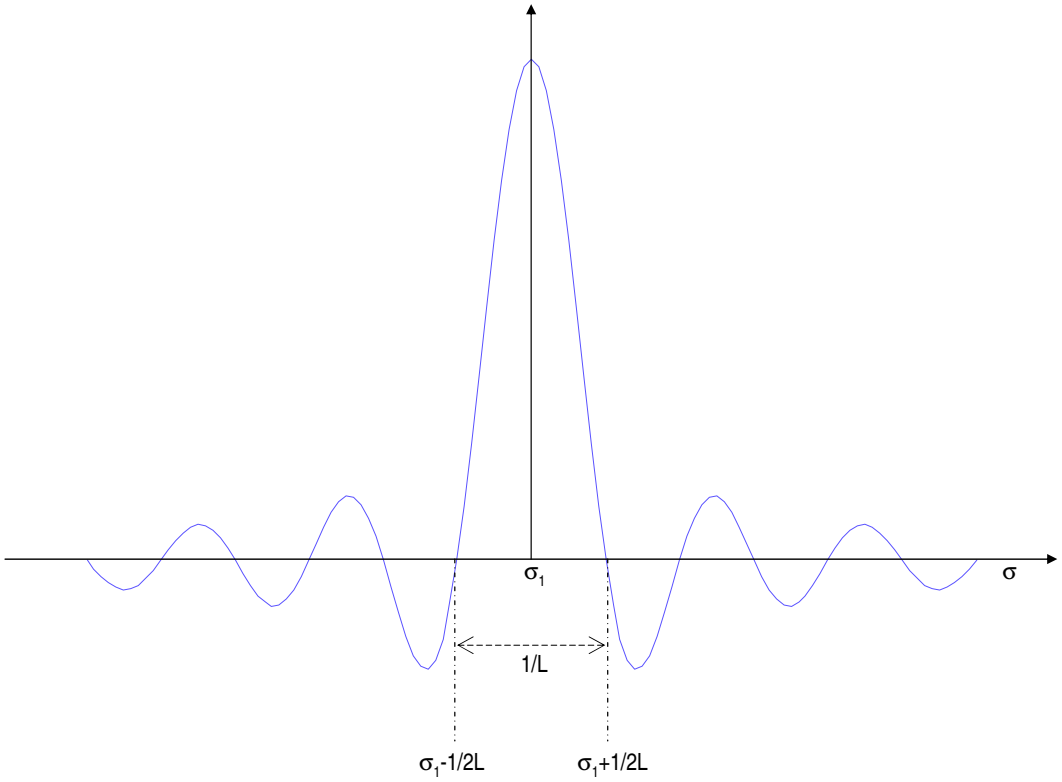

Figure 2.1: The sinc function convolved with a single spectral line at σ_1.

transform of Eq. 2.10. The fidelity of the spectrum is improved by apodizing, whilst the theoretical resolution is reduced by the effect of the truncation.

2.1.5 Sampling

In order to obtain the spectrum from an interferogram, a mathematical computation must be performed. The data is obtained by sampling at regular and small intervals of δ along the interferogram. The Fourier integral is then approximated by a sum. The sampling process can be handled mathematically by the Dirac delta comb,

$$\underline{III}(\delta) = \sum_{n=-\infty}^{\infty} \delta_{dirac}(\delta - n). \tag{2.15}$$

The interferogram $I(\delta)$ is an analog signal which is digitized at intervals of $\Delta(\delta)$. The sampled interferogram $I'(\delta)$ is given by

$$I'(\delta) = \underline{III}(\frac{\delta}{\Delta\delta})I(\delta) = \Delta\delta \sum_{n=-\infty}^{\infty} I(n\Delta\delta)\delta_{dirac}(\delta - n\Delta\delta). \tag{2.16}$$

Then, the spectrum obtained from the Fourier transform of $I'(\delta)$ is

$$I'(\delta) = \frac{1}{\Delta\sigma}\underline{III}(\frac{\sigma}{\Delta\sigma}) \otimes I\sigma = \sum_{n=-\infty}^{\infty} I(\sigma - n\Delta\sigma), \tag{2.17}$$

where $\Delta\sigma = 1/\Delta\delta$ and $I(\sigma) = \mathcal{F}[I(\delta)]$. The last expression is the computed spectrum, which is composed of periodic replicas of our real spectrum $I(\sigma)$ with period $\Delta\sigma$. The above is an important result that impacts our analysis. The proper choice of the sampling rate produces a true spectrum that is confined to only one-half of the replication period, i.e. $\sigma_{max} \leq \Delta\sigma/2$ (see Fig. 2.2). In order to prevent the effect called aliasing, we have to ensure the condition of $\delta \leq 1/2\sigma_{max}$. This condition states that the highest frequency must be sampled at least twice, which is the Nyquist sampling criterion. Experimentally it is necessary to ensure a high enough sampling rate or limit the range of frequency input to the detector by means of optical and/or electronic filtering.

2.1.6 Phase error and correction

Until this point, we have assumed an interferogram with perfect symmetry around the zero path difference. Experimentally a recorded interferogram could be asymmetric, due mainly to a phase error introduced in the measured interferogram. Phase errors can result from sampling errors, electronic filtering and optical effects from various parts of the instrument optics and cause a distortion of the

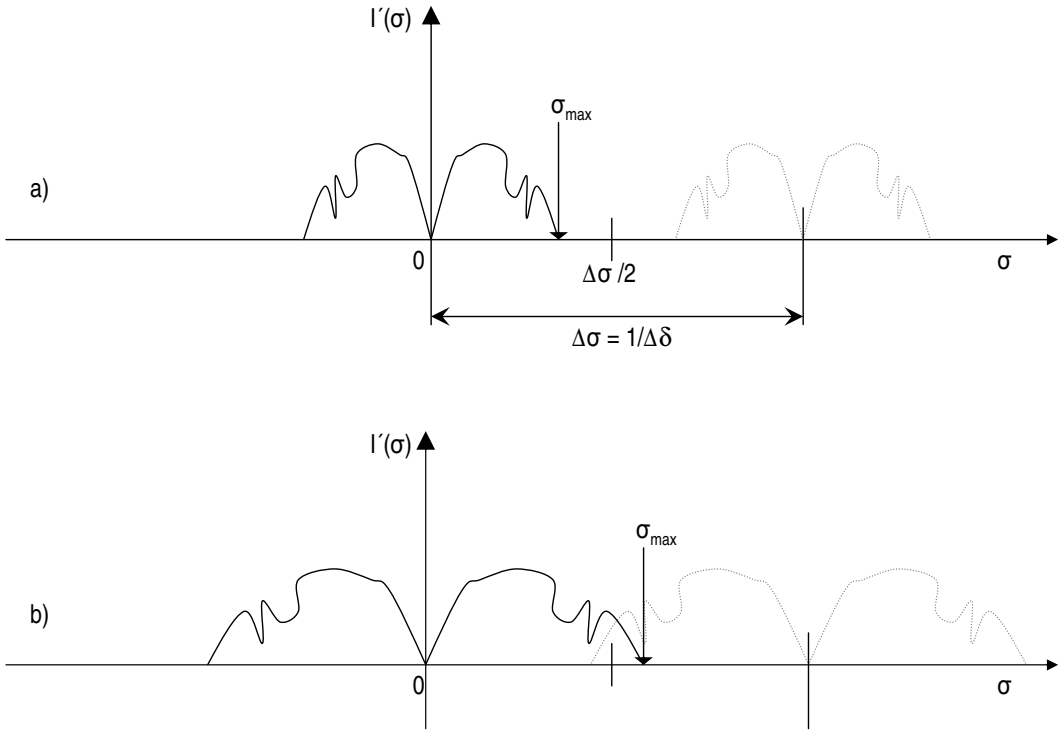

Figure 2.2: Spectrum replication and sampling rate: a) the correct choice of the sampling rate produces an spectrum confined to one-half of the replica period; b) a bad selection of the sampling rate will produce an overlap of the replicated spectrum.

instrumental line-shape function. This leads to a negative spectrum or slight shift of the spectral features. When the phase error is introduced to the interferogram we have

$$I(\delta) = \int_{-\infty}^{\infty} \left[I(\sigma) e^{i\theta} \right] e^{-i2\pi\sigma\delta} d\sigma, \tag{2.18}$$

where θ is the phase error, or the phase spectrum which can be frequency dependent. The computed spectrum is then

$$\tilde{I}(\sigma) = I(\sigma)e^{i\theta}. \tag{2.19}$$

Therefore, an asymmetric interferogram produces a complex spectrum. The phase spectrum can be corrected using the Mertz method, Mertz 1965, which is the most commonly scheme used. The instrumental phase is determined taking a small symmetric sample of the interferogram about the central fringe and then performing Fourier transform on this sample. The result is a low-resolution, high signal-to-noise computed spectrum, which is normalized to its maximum. Using the real and imaginary of the high S/N computed spectrum we obtain the phase spectrum as

$$\theta(\sigma) = arctan\frac{\Im(\sigma)}{\Re(\sigma)}. \tag{2.20}$$

The conjugate of this phase spectrum $e^{-i\theta(\sigma)}$ is then multiplied by the Fourier transformed spectrum of the full interferogram in order to obtain the computed phase-corrected spectrum of the source $I(\sigma)$.

2.1.7 Interferogram scanning methods

Commonly there are two kind of interferometers depending of the scanning method: step-scan interferometer and rapid-scan interferometer. In the step-scanning method, the movable mirror, on a motorized track, starts from a reference point and steps to equidistant points along the linear track. At each point the movable mirror is kept stationary and the detector signal is recorded. The movable mirror proceeds along the track until the desired resolution is achieved. The step-scan method has an unavoidable downtime (overhead) while moving from one sampling point to the next, and whilst waiting for the mirror position to stabilize, before acquiring the signal. This approach takes a longer time to complete a single scan than a continuous movement,and therefore it is sensitive to

slow variations in the source intensity and instability in the detector and readout electronics.

In the rapid-scan method the movable mirror moves at constant velocity along the linear track. This method modulates the incoming signal at a frequency ν' which is related to the mirror velocity ν,

$$\nu' = \frac{\nu}{\lambda} = \nu\sigma, \tag{2.21}$$

An important factor in the rapid-scan system is the determination of the correct time to start the data acquisition. This information is required because the analysis method relies on the co-adding (synchronization) of various low S/N interferograms. The S/N ratio increases as the square root of the number of scans co-added.

2.2 Martin Puplett Interferometer

The Martin-Puplett Interferometer (here after, MPI) is a version of the Michelson interferometer that uses wire-grid polarizers as beam splitters and roof mirrors for reflectors. The MPI has been used widely in FIR spectroscopy and in astrophysical spectroscopy. The MPI provides two input ports; one of them could be used with a blackbody source of known temperature in order to have an absolute intensity calibration. In addition, the MPI provides two output ports which are complementary and hence the output signals can be subtracted to cancel any common-mode noise. The MPI is an absolute interferometer because the DC offset component is removed. One of the main advantages of the wire-grid polarizers is the flat broad-band spectral response.

2.2.1 Wire grid polarizer

A wire-grid polarizer consists of many parallel wires separated by a small distance in the plane of the grid. The physical properties of the polarizing grids designed and fabricated for this experiment (i.e dimensions, wire-spacing, material, etc) are described in chapter 5. When the light enters the polarizer, the component parallel to the wire grid will induce a current along the wires. Therefore, all the wires act as a solid metallic surface, which reflects that portion of the incoming light with a 180 degree phase shift. The perpendicular portion of the incoming light will not introduce a significant current in the transverse direction of the wires, and therefore this component is unaffected and the light will be transmitted through the polarizer. Hence, if the incoming light is polarized in a particular direction, say horizontally, and is incident on a polarizer oriented at an angle of 45 degrees respected to the incoming light, then half of the light will be transmitted and half will be reflected. For the case in which half of the light is reflected, a 180 degree phase shift occurs and the transmitted portion is unaffected. Thus both the reflected and the transmitted components are 180 degrees out of phase.

2.2.2 Roof mirror

A roof mirror is a pair of plane metal surfaces placed at 90 degrees to one another. The intersection line formed by the two planes is called the *roof line*. The effect of a roof mirror is to reflect the incoming light which is perpendicular to the roof line in the direction of incidence. The roof mirror also rotates the polarization by 2ϕ, where ϕ is the angle between the roof line and the incident polarization direction. If the resulting direction of polarization after passing through the polarizer is 45 degrees, then the polarization shift is 90 degrees.

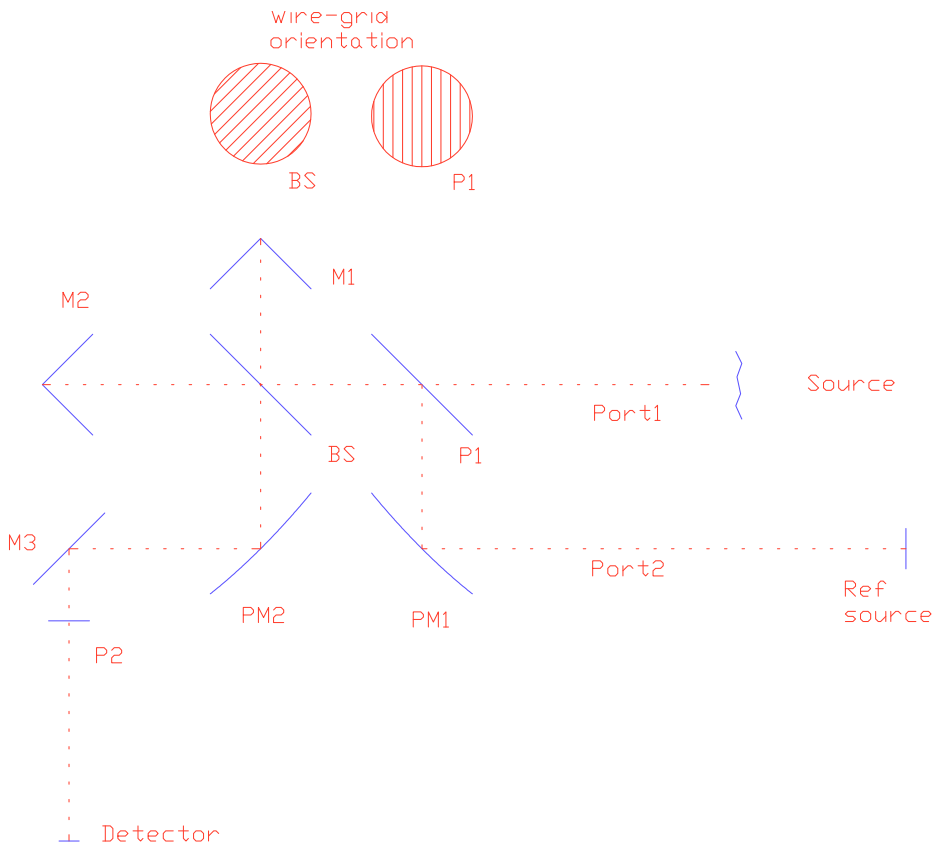

Figure 2.3: A schematic of a Martin-Puplett interferometer, showing the position and orientation of the various ports, mirrors an and polarizing grids.

2.3 Polarization through the interferometer

Figure 2.3 shows the MPI schematically, which is the same as the configuration used for our design. The polarizer P1 will be oriented at some angle, say vertically. The polarizer BS is oriented 45 degrees with respect to the P1. P1 is oriented in the x direction, which indicates horizontal polarization in the positive x direction. When the light is incident upon P1, half of the light pases through P1 with horizontal polarization and the other half is reflected upwards. The resultant electric field vector is

$$E_i = Asin\left(\frac{2\pi ct}{\lambda}\right)x, \tag{2.22}$$

where A is the amplitude of the field. The light that comes from PM1 and is incident at P1 will also enter the interferometer by reflection. After passing through the P1 the light strikes BS. Half the light is transmitted through the beam splitter and half is reflected. The transmitted light now has a electric field vector of

$$E_t = \frac{1}{2}Asin\left(\frac{2\pi ct}{\lambda}\right)(x+y). \tag{2.23}$$

The transmitted light is incident on the roof mirror M2 which reflects the light back with a phase shift of 90 degrees and returns to BS. At this point the light has a traveled a distance d1, which is the round-trip distance from BS to M2. The electric field vector is

$$E_t' = \frac{1}{2}Asin\left(\frac{2\pi(ct+d1)}{\lambda}\right)(x-y). \tag{2.24}$$

On the other hand, the light which is reflected towards M1 from BS has an electric field vector of

$$E_r = \frac{1}{2}Asin\left(\frac{2\pi ct}{\lambda}+\pi\right)(x-y). \tag{2.25}$$

where the polarization is -45 degrees, and a 180 degree phase shift is introduced by the BS reflection. The light travels toward M1, and the polarization angle is now shifted 90 degrees. The light has travelled a round trip distance d2 from BS to M1. Thus, the electric field vector is

$$E_r' = \frac{1}{2}Asin\left(\frac{2\pi(ct+d2)}{\lambda}+\pi\right)(x+y), \tag{2.26}$$

when the light returns to BS. Now, the light beams are incident on BS. The beam that comes from M2 will now reflect and a 180 degree phase shift is introduced with respect to the light leaving BS. The electric field vector is

$$E_{tr} = \frac{1}{2} A sin\left(\frac{2\pi(ct + d1)}{\lambda} + \pi\right)(x - y). \tag{2.27}$$

The light that comes from M1 is now transmitted through BS. The electric field vector is unaltered. We can write this vector as

$$E_{rt} = \frac{1}{2} A sin\left(\frac{2\pi(ct + d2)}{\lambda} + \pi\right)(x + y). \tag{2.28}$$

The two beams leave BS in parallel and continue toward the mirror PM2 and eventually the detector. The total field E_{tot} is therefore the sum of E_{tr} and E_{rt}

$$\begin{aligned} E_{tot} &= A sin\left(\frac{\pi(2ct - d1 - d2)}{\lambda} + \pi\right) cos\left(\frac{\pi(d1 - d2)}{\lambda}\right) x \\ &+ A cos\left(\frac{\pi(2ct - d1 - d2)}{\lambda} + \pi\right) sin\left(\frac{\pi(d1 - d2)}{\lambda}\right) y. \end{aligned} \tag{2.29}$$

Note that the first term in both components have an argument of $(\frac{\pi(2ct-d1-d2)}{\lambda} + \pi)$; the sine term will be zero when $2ct - d1 - d2$ is an integral number of wavelengths, and the cosine term will be zero when $2ct-d1-d2$ is a half number of wavelengths. The argument in the second term of both components is $\left(\frac{\pi(d1-d2)}{\lambda}\right)$. The sine term will be zero when $(d1 - d2)$ is an integral number of wavelengths and similarly the cosine term will be also zero when $(d1 - d2)$ is a half number of wavelengths.

A MPI system is able to work with two input ports and two output ports. If there is a load present in the system in both input ports, then the radiation from this load will enter the interferometer by transmission and reflection at P1. In our analysis P1 is oriented vertically. The radiation from a load placed to the right of P1 will be transmitted, and a load placed below P1 (after being collimated by PM1) will be reflected. The transmitted component will have a horizontal polarization and the reflected component will have vertical polarization. Then, the two components will sum after P1, producing unpolarized light. When this

unpolarized light is incident on BS, it will split and recombine such that the beam will be unpolarized after leaving BS. The sum of the contribution of both the horizontal and vertical polarized components after BS will be

$$\begin{aligned} E_T &= A\Bigg\{ sin\left(\frac{\pi(2ct-d1-d2)}{\lambda}\right) cos\left(\frac{\pi(d1-d2)}{\lambda}\right) \\ &+ cos\left(\frac{\pi(2ct-d1-d2)}{\lambda}\right) sin\left(\frac{\pi(d1-d2)}{\lambda}\right)\Bigg\}(x+y). \end{aligned} \tag{2.30}$$

The incident light on the detector is one half of the light leaving BS, no matter the orientation of P2. The light from the load will affect the absolute measurement of the intensity in a constant way as long as the load source is unpolarized, isotropic and uniform in time.

Up to here, we have reviewed the basics of the Fourier transform spectroscopy. The importance of this brief resume, it is to put into the context the basics mathematical expression to understand the influence of the aspects such as, maximum optical path difference L, sampling intervals δ and scanning methods (i.e. continuous-scan and step-integrate scan). We have also described the main elements of the Martin-Puplett interferometer, which allows us to understand how the elements affect the radiation entering the interferometer. This previous knowledge will give the tools for the design of the FTS system, which is described in Chapter 5.

Chapter 3

Bolometer theory for millimeter-wave detectors

There are a wide variety of detectors used in astronomy, which act mainly as the transducer of the incoming radiation. The detectors can be categorized by the physical process used to convert the electromagnetic radiation into an electrical variable. In essence, there are three techniques: (i) photoelectric effect; (ii) induced current by electromagnetic radiation, and (iii) thermal effects.

The photoelectric detection is achieved by generation of energy carriers in the detector due to the incidence of a photon. The detection of a single photon is possible if the energy exceeds several MeV i.e. at wavelengths larger than 200 μm. Devices based on a photoelectric effect are used over a wide spectral-range, that goes from X-rays to mid infrared wavelengths.

Detectors which convert the electromagnetic field into current are also called "no quantum" detectors. The electromagnetic field is coupled to an antenna, which produces a current, which is then applied a non-linear element, i.e. a Shottky diode. These detectors are usable throughout the whole radio and sub-

mm/mm wavelength range.

The detectors based on thermal effect absorb the photon energy and transform it into thermal excitation. The incident radiation can be detected by the small temperature drift produced by the excitation. These detectors are mainly used at infrared and sub-mm/mm wavelengths as bolometers, as well as in the X-ray and gamma-ray regimes as calorimeters. Due to their broad-band spectral response, bolometers are also the most suitable as detectors for spectroscopy (i.e. as part of an FTS).

The Fourier transform spectrometer described in this thesis will be used to measure the sub-mm/mm atmospheric emission and calculate the transmission spectrum of the atmosphere and other materials, such as bandpass filters. We have chosen to use a bolometer as the detector in a cryogenic system operating at ~ 1.8 or 3.9 K. The FTS-MPI is designed to work over a frequency range of ~ 215 to 2000 GHz. The estimated sky background power that falls on the bolometer continuously is 30×10^{-9} W. For an operating temperature is 1.8 K, the required noise equivalent power (NEP) of the detector under background limited operation is $\sim 10^{-15}$ WHz$^{-1/2}$. These parameters drive the design and performance of the bolometer, which are described in chapter 4, as well as the results of the electrical characterization of the cryogenic detector system.

In this chapter we describe bolometer theory and their basic principles of operation. We focus our attention on those devices that use Neutron Transmutation Doped Germanium (NTD Ge here after) thermistors. The theory has been developed and reported by other authors (e.g. Low 1961; Mather 1982; Richards 1994), and therefore only a brief review of the theory for ideal bolometers is given here. The experimental characterization of our cryogenic bolometer system is described in chapter 4.

3.1 An ideal Bolometer

A bolometer is a thermal device, which does not detect photons by means of an excitation of the charge carriers, but instead it detects a thermal variation which is proportional to the energy absorbed from the photons. Typically bolometers have a broadband spectral response that is defined by the properties of the absorber material used. Bolometers are the most suitable devices for applications in the infrared and sub-mm/mm spectral range (since stressed photoconductors reach their limits at $\sim 200\mu m$). The germanium crystal was the first thermometer, (Low, 1961) to be developed for operation at low temperature. Currently the most popular thermometer elements are those made by the NTD process, which produces more uniform doping through the semiconductor crystal.

Semiconductor bolometers have been used successfully in astronomical observations in the past, although they will become increasingly replaced by a new generation of devices in the future. The increasing research effort into the development of superconducting detectors and into micro-machining techniques have now made it possible to construct large-format detectors array (i.e. ≥ 1000 pixels). The next generation of instruments (e.g. SCUBA-2) will be based on the Superconducting Transition Edge Sensor (TES) array that will work mapping the focal plane of the telescope as fast as a CCD or IR array does.

TES detectors are made of a superconducting film that works in the transition temperature region T_C, between the superconducting and normal state. The resistance has a very steep dependence on temperature as shown in Figure 3.1. Small changes in temperature will produce a large change in resistance. These devices are voltage biased, so that the change in resistance produces a change in the current through the superconducting film, which is measured with a very sensitive ammeter (i.e. Superconducting Quantum Interference Devices, SQUID).

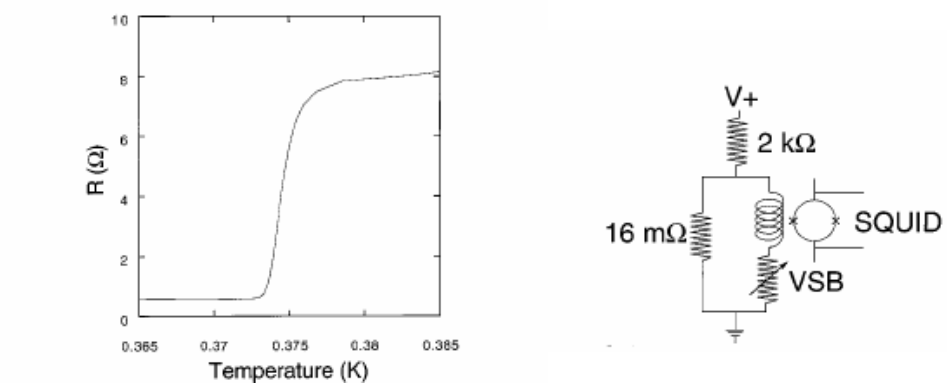

Figure 3.1: At the left the resistance versus temperature characteristic for a superconducting Ti film at Tc∼370mK (Lee et al., 1998). At the right the voltage-biased bolometer with the SQUID read-out amplifier.

3.2 Principles of operation

All thermal detectors work as follows and Figure 3.2 illustrates the basic operation of a bolometer. The detector is connected to a heat sink at temperature T_0 (K), by mean of thermal link of conductance G (W/K). We assume there are no additional heat leaks. In the absence of any optical loading, the detector absorbs a constant electrical power P_{bias} (W), which is applied by a voltage source V_{bias}, and hence the detector increases the temperature to T. Under steady state condition the thermal conductance is given by,

$$G = \frac{P_{bias}}{T - T_0} \tag{3.1}$$

Under the condition of a time varying incident power, P_{signal} (W), the bolometer temperature will increase due to the energy absorbed, dQ, in a given period of time dt, such that

$$\eta P_{signal} = \frac{dQ}{dt} = C\frac{dT}{dt} \tag{3.2}$$

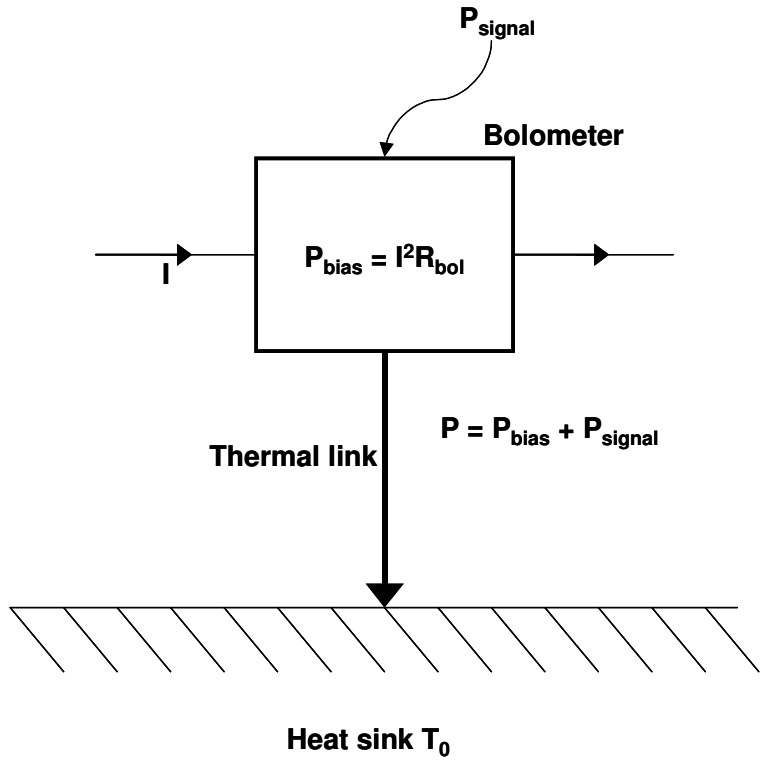

Figure 3.2: Schematic principle of operation

where η is the quantum efficiency and C is the heat capacity (J/K). The total power $P_T(t)$ absorbed by the detector is

$$P_T(t) = P_{bias} + \eta P_{signal} = GT + C\frac{dT}{dt}. \tag{3.3}$$

In order to solve the above equation, we assume that P_{signal} is a step function where $P_{signal} = 0$ for $t < 0$ and $P_{signal} = Q$ for $t > 0$. Thus the bolometer temperature is,

$$T = \begin{cases} \frac{P_{bias}}{G} & \text{for } t < 0 \\ \frac{P_{bias}}{G} + \frac{Q}{G}(1 - exp(\frac{-t}{\tau}) & \text{for } t > 0, \end{cases} \tag{3.4}$$

where $\tau = C/G$ which is the thermal time constant of the bolometer. We can see

that for a time t greater than the thermal time constant τ, the final temperature is proportional to the total power $P_T = P_{bias} + Q$, and for a given constant bias power we can derive the incident power.

3.3 Electrical properties

The performance of a bolometer is related to the temperature dependence of the thermistor element given by the temperature coefficient,

$$\alpha(T) = \frac{1}{R}\frac{dR}{dT} \tag{3.5}$$

The value of α should be as large as possible to maximize the temperature dependence of the thermistor. In order to use bolometers at low temperatures we need a semiconductor material that is highly doped with impurities which are very close together in the crystalline structure, so the electrons shift from one atom to other without first entering the conduction band. Typical doping processes, produce large variations of α and R_{bol}. A neutron transmutation doping, (Haller et al., 1982) is a more suitable method to give very uniform doping throughout a large piece of single semiconductor crystal. The bolometer resistance as a function of temperature is then given by

$$R = R_0\, exp\left(\frac{T_g}{T}\right)^n \tag{3.6}$$

where R_0, T_g are material parameters with a value of $n = 1/2$ that produces good fit to the observed R vs. T variation , (Haller et al., 1982). Figure 3.3 illustrates a typical bias circuit. The bolometer is biased with a load resistor R_L, usually with a value much greater than the bolometer resistance at typical operational temperatures. Hence the bias current I_{bias} flowing through the bolometer is independent of the bolometer resistance. Usually the first amplifier stage is a high impedance transistor (i.e. JFET) placed close to the detector

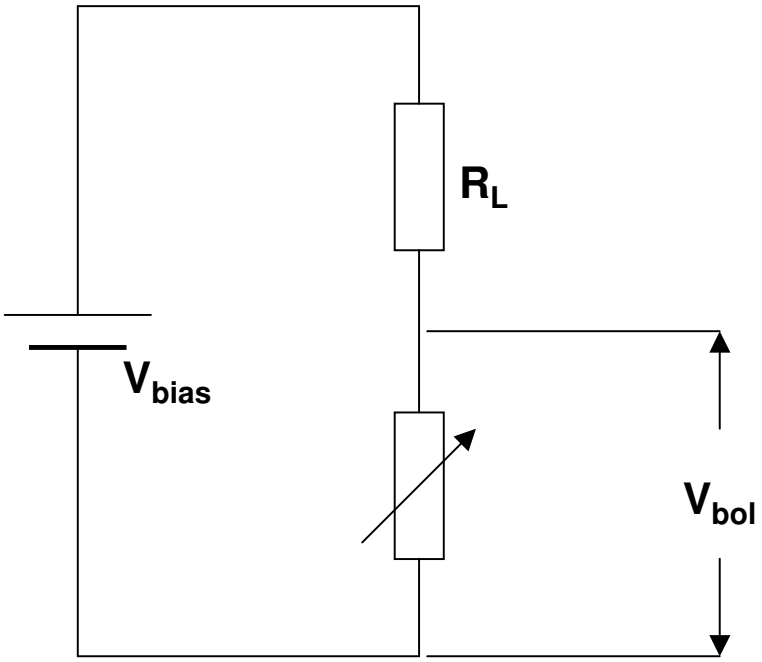

Figure 3.3: Typical bias circuit for a single bolometer represented as a variable resistor R_{bol}

in order to minimize microphonic noise due to the mechanical vibrations in the wiring. Details of operational temperature and thermal isolation are described in section 4.1.2 and 4.2.

3.3.1 Bolometer time response

The power dissipated by the detector is $P_{bias} = I_{bias}^2 R_{bol}(T)$. Since the bolometer resistance R_{bol} is function of the temperature, we express the total power in the following way,

$$P_T(t) = C\frac{dT}{dt} + G\Delta T - \frac{dP_{bias}}{dT}\Delta T \tag{3.7}$$

The first term is the power absorbed by the detector, the second term is the

bias power and third is the dissipated power by the detector resistance R_{bol}. The change in the power due to a change in the temperature is expressed as,

$$\frac{dP}{dT} = I^2 \frac{dR_{bol}}{dT} \tag{3.8}$$

where $\frac{dR_{bol}}{dT} = R_0\alpha(T)$, and hence

$$\frac{dP}{dT} = \alpha(T)P_{bias} \tag{3.9}$$

Substituting equation 3.9 into the expression for total power (Eq. 3.7) we obtain

$$P_T(t) = C\frac{dT}{dt} + (G - \alpha P_{bias})\Delta T. \tag{3.10}$$

Solving this diferential equation we then obtain the electrical time constant $\tau_e = \frac{C}{G-\alpha P_{bias}}$.

When $\alpha < 0$ we observe that the electrical time constant is smaller than the thermal time constant ($\tau = C/G$). Therefore, a bolometer responds electrically faster than thermally which is due to the Electro thermal feedback. This effect has the advantage to speed up the response time of the sensor.

3.3.2 Responsivity

The temperature of a bolometer increases due to absorbed radiant power. The bolometer is also biased by a constant current, and produces additional electrical power via the Joule effect. The bolometer dissipates the combined power through the thermal link to the heat sink. Changes in the voltage output are related to variations in the absorbed power. The detector responsivity is defined as the change in the voltage output due to the absorbed input signal power, dV/dP (V/W),

$$dV = IdR = I\alpha RdT = \alpha V dT, \tag{3.11}$$

for a zero frequency response ($\tau >> \tau_e$) and where dT is expressed as

$$dT = \frac{dP}{G - \alpha P_{bias}} \tag{3.12}$$

and hence

$$dV = \frac{\alpha V dP}{G - \alpha P_{bias}}. \tag{3.13}$$

The electrical responsivity of a bolometer $S(0) = dV/dP$ is then

$$S(0) = \frac{\alpha V}{G - \alpha P_{bias}}. \tag{3.14}$$

In order to measure the electrical responsivity it is necessary to derive α and G from the V-I load curve. The dependence of the voltage on bias is not linear due to the Joule heating of the bolometer. For a bolometer with $\alpha < 0$, $V_{bol}(I)$ is linear with a slope R when $V_{bol} \approx 0$ (low bias regime), and it also has a broad roll over before falling slowly at larger bias currents. Experimental V-I curves are presented in Chapter 4.

From the load curves, we are able to derive R = V/I and the impedance Z = dV/dI. The electrical responsivity S can also be expressed in terms of R and Z when no optical power is applied.

$$S(0) = \frac{(Z - R)}{2IR} \tag{3.15}$$

Note that the responsivity of a bolometer is independent of the operation wavelength.

3.3.3 Noise and noise equivalent power (NEP)

There are two ways to study the noise in a bolometric system. The first is under assumption of thermal equilibrium. The second is using the non-equilibrium

theory developed by Mather (1982) in which the mechanism of the thermal feedback is taken into account. In the present work we use the thermal equilibrium theory that is very useful for obtaining a general understanding of the bolometer operation and its optimization.

One important figure of merit for a bolometer is the noise equivalent power (NEP), which is a measure of the sensitivity of a bolometer, and is defined as the power absorbed that produces a signal to noise ratio of unity at the output (units of $W/Hz^{1/2}$). The NEP is formed by taking into account the detector and the background noise, and can be expressed as,

$$NEP_{tot} = \sqrt{NEP^2_{detector} + NEP^2_{background}} \tag{3.16}$$

In an ideal case the NEP should be limited by the thermal noise (i.e. sky background, telescope and optics background) and not by the detector noise contribution. In general there are two types of noise in a bolometric system. One kind is related to the pure electrical components (i.e. Johnson noise coming from the bolometer, load resistor and amplifier). The bolometer is subject to Johnson noise due to the random motion of the free electrons in the thermistor element and it is expressed as,

$$NEP_J = \frac{(4kTR_{bol})^{1/2}}{S} \tag{3.17}$$

where k is the Boltzman constant, and S is responsivity in V/W. The NEP_J is independent of the load resistance. Another source of Johnson noise comes from the load resistors, but in the practice we reduce this contribution by using a large load resistor $R_L >> R_{bol}$ at the operating temperature.

Second, noise comes from thermalization of the mechanical vibrations and thermal fluctuations at the thermal link (i.e. electrical leads), which is produced by the random propagation of energy carriers, (e.g. electrons, phonons, photons, etc). These fluctuations are generally called phonon noise, and are analogous

to the Johnson noise. We consider a system with a heat capacity C connected via a thermal link with a conductance G to a heat sink at T_0 to help describe its contribution. In thermal equilibrium the energy E_T stored in the thermal capacitance C_T should be,

$$E_T = \frac{1}{2} C_T T_N^2 \tag{3.18}$$

where T_N is the thermal fluctuation, and the power dissipation in the R_T (where R_T is the equivalent resistance that replaces the thermal link) is

$$P_T = \frac{T_N^2}{R_T}. \tag{3.19}$$

We also expect the circuit to have a exponential response with a time constant of $R_T C_T$. From $\tau = C/G$ we obtain,

$$C_T = \frac{C}{T} \quad \text{and} \quad R_T = \frac{T}{G} \tag{3.20}$$

where R_T is the thermal resistance. Using the the electrical analogous $\langle V_J^2 \rangle = (4kTR)d\nu$, to make the analogy with the thermal variables we have,

$$\langle T_N^2 \rangle = \frac{4kT^2}{G} d\nu \tag{3.21}$$

We let P_ν be the power falling on the bolometer which produces a temperature change of

$$\Delta T_s = \frac{\eta P_\nu}{G} \tag{3.22}$$

Thus the value of P_ν give us an equality between thermal fluctuations and the signal noise,

$$\Delta T_s = \langle T_N^2 \rangle^{1/2} \tag{3.23}$$

such that the phonon NEP in unit bandwidth is expressed as,

Temperature	NEP	Author
0.10	2.5×10^{-17}	Hagmann et al. 1992
0.30	1×10^{-16}	Alsop et al. 1992
0.97	1.6×10^{-15}	Lange et al. 1987
1.6	4.5×10^{-15}	Serlemitsos 1989

Table 3.1: NEP performance for NTD:Ge composite bolometers at different bath temperatures.

$$NEP_T = \frac{(4kT_0^2G)^{1/2}}{\eta} \tag{3.24}$$

Finally we consider the photon noise, which arises from random fluctuations in the rate of absorbed radiation. In order to give a complete computation of photon noise, all the optical components of the system should be included. The noise equivalent power is given by,

$$NEP_{pho} = (2h\nu(\epsilon\tau\eta)P_\nu)^{1/2} \tag{3.25}$$

where P_ν is the incident absorbed power given by $P_\nu = A\Omega(\epsilon\eta)\int_{\nu_1}^{\nu_2} B_\nu(T_{bg})d\nu$, where ϵ is the emissivity, η is the overall transmission of the system, $A\Omega$ is the telescope throughput (A is the telescope primary area and Ω is the beam solid angle) and $B_\nu(T_{bg})$ is the Planck function for the background temperature T_{bg}.

Therefore the total NEP for a bolometer is given by the quadratic combination of the NEP's from all uncorrelated noise sources, including those described above,

$$NEP = (NEP_J^2 + NEP_T^2 + NEP_{pho}^2 + \ldots)^{1/2} \tag{3.26}$$

From the last expression we can optimize the total NEP by minimizing the R_{bol}, T_0, G and P_ν and maximizing S. Also, we observe here the importance of reducing the operating temperature to improve the performance of the bolometric device (see Table 3.1).

3.4 Physical parameters

3.4.1 Heat capacity

The material used as a thermistor is usually a semiconductor crystal. The specific heat of a pure semiconductor material at low temperature is given by the Debye theory for a crystal lattice:

$$c_v^{lat} = \frac{12\pi^4 \aleph_A k}{5} \left(\frac{T}{\Theta_D}\right)^3, \tag{3.27}$$

where $\aleph_A$ is Avogadro's number times density over atomic weight and Θ_D is the Debye temperature. For metals, c_v, includes contributions both from the lattice structure and from free electrons. The electronic specific heat is

$$c_v^e = \gamma_e T(\rho \,\mathrm{mole}^{-1}), \tag{3.28}$$

where γ_e depends on the metal and ρ is the material density. The specific heat includes the lattice and electronic contributions, and as the temperature approaches to zero, the major contribution is due to c_v^e. Hence

$$c_v = DT^3 + \gamma_e T, \tag{3.29}$$

Since a bolometer is a semiconductor connected by metallic leads, the contributions to its heat capacity comes from both the crystalline semiconductor elements ($C \propto T^3$) and from the electrical leads ($C \propto T$), such that

$$C = c_v^{lat} V_{lat} + c_v^e V_e, \tag{3.30}$$

where V_{lat} and V_e represent their respective volumes.

For temperatures above 1 K we have chosen very carefully the materials in order to reduce the total heat capacity of our device (see Chapter 4). Another way to minimize C is by reducing the total volume of the elements, although in

the practice the exact dimension of some components are hard to control (i.e. glue, silver epoxy, etc.)

3.4.2 Thermal conductance

The behavior of the thermal link has a direct influence on many figures of merit for a bolometer (e.g. NEP, time response and responsivity). The thermal conductance is dominated by the electrical leads. The thermal conductivity of metals is described by

$$k_e \approx \mathcal{L}\sigma T \tag{3.31}$$

where the term $\mathcal{L}$ is the Lorentz number ($\approx 2.45 \times 10^{-8}\ W\Omega K^{-2}$) and σ is the electrical conductivity. The value of k_e is $\sim T^a$, with $a \geq 1$ for low temperatures (e.g. $\sim$.1 - 4.2 K). Usually a bolometer is connected with two leads of length L and cross sectional area A, so that the thermal conductance is

$$G = 2\frac{A}{L}k_e. \tag{3.32}$$

3.4.3 Choice of the thermistor

Usually Si and Ge semiconductors are used as the thermometer material for bolometers operating at L^{4}He temperatures. These devices must then be heavily doped in order reduce the intrinsic large resistance at such low operating temperatures ($\sim 0.1 - 4.2$ K).

Semiconductors thermistors are doped close to the metal-insulator transition with majority impurity, in order to get a hopping conductivity mode, (Efros & Shklovskii, 1975), which gives a temperature-dependent resistance described by Eq. 3.6. A neutron transmutation doping (NTD) of ultra-pure Ge produces a more uniform material that can operate effectively at temperatures from 4.2 K

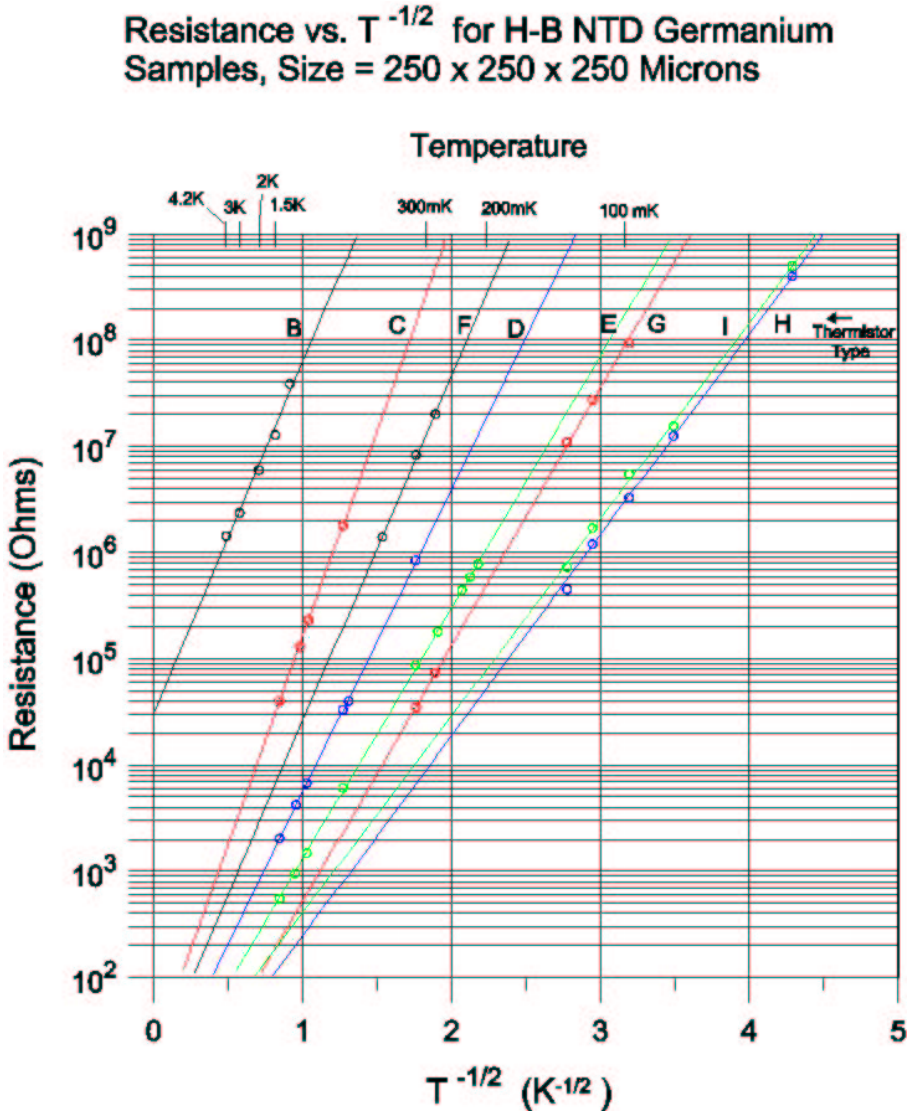

Figure 3.4: R-T curves for diferents NTD:Ge thermistors from Haller-Beeman Inc. The thermistor type B was selected to build the bolometer for the detection system.

to 20 mK. The data shown in figure 3.4 was taken from datasheets of Haller and Beeman Inc. We see a linear relationship between log resistivity and $T^{-1/2}$ which indicates good agreement with the theory (Eq. 3.6). NTD Ge thermometers ($\sim 200\ \mu m^3$) are now mass-produced with ion implanted and metallazided (Cr or Ti-Au) contacts pads. Electrical leads can be attached with silver-filled epoxy.

The difference between Si and Ge bolometers is due mainly to their heat capacities. The lattice specific heat per unit volume of Si is a factor of ~ 5 smaller than that for Ge at L^{4}He temperatures. At temperatures lower than 1 K the lattice contribution of both Si and Ge to their heat capacity are negligible compared to the contributions from the metallic elements or epoxy (see Eq. 3.29). We use a NTD germanium thermistor manufactured by Haller-Beeman Inc that follows our performance requirements. In the next chapter we describe the bolometer design, materials and construction. We also discuss the cryogenic system and electronics, as well as the data-acquisition system that allow us to perform the experimental characterization, including R vs. T dependence and measurements of responsivity, time constant and NEP.

Chapter 4

Cryogenic Camera for the FTS

As part of the construction and testing a working sub-mm/mm FTS we decided to design a detection system for FTS-MPI (described in Chapter 5) based on a composite bolometer detector due to its sensitivity and low noise characteristics over the sub-mm/mm wavelengths. In this chapter we describe the design of the bolometer, assuming it operates under background limited conditions, and also describe how this influences parameters such as thermal conductance and operating temperature. We also explain issues related to the overall characterization of the cryogenic system and finally we derive the figures of merit for the bolometer.

4.1 Bolometer design

The cryogenic camera system for the FTS uses a composite bolometer, which consists of a small thermistor element mounted in a dielectric-coated substrate. The dielectric substrate acts as the absorber of the incident radiation. Figure 4.1 shows the general scheme for our composite bolometer, which consists of a NTD Ge thermistor mounted on a thin square of sapphire. The absorber surface is

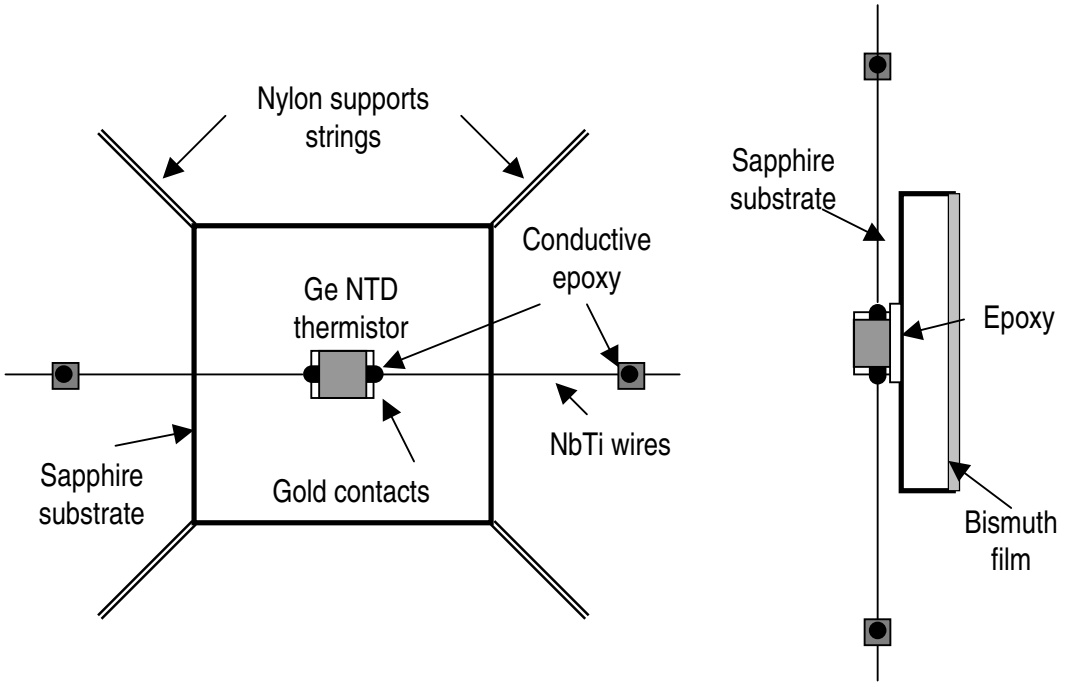

Figure 4.1: Details of the composite bolometer unit.

coated with a thin bismuth metal film in order to improve the absorption.

The bolometer-absorber unit is suspended by two nylon leads that provided stiff support, in order to avoid microphonic vibration. The contact pads are gold plated to provided good thermal and electrical connection with the two NbTi electrical leads. The NbTi wires, which are connected to the cold stage by mean of a Winston cone, define the thermal conduction path. The physical dimensions, optical and electrical properties of the bolometer are described in the following sections.

The largest contributions to the heat capacity are from the NTD chip, electrical wires and the epoxies. Since we are unable to measure the dimensions of the bolometer components, we have to assume that the device was fabricated exactly to our specifications. If this is not the case then our calculated heat capacities

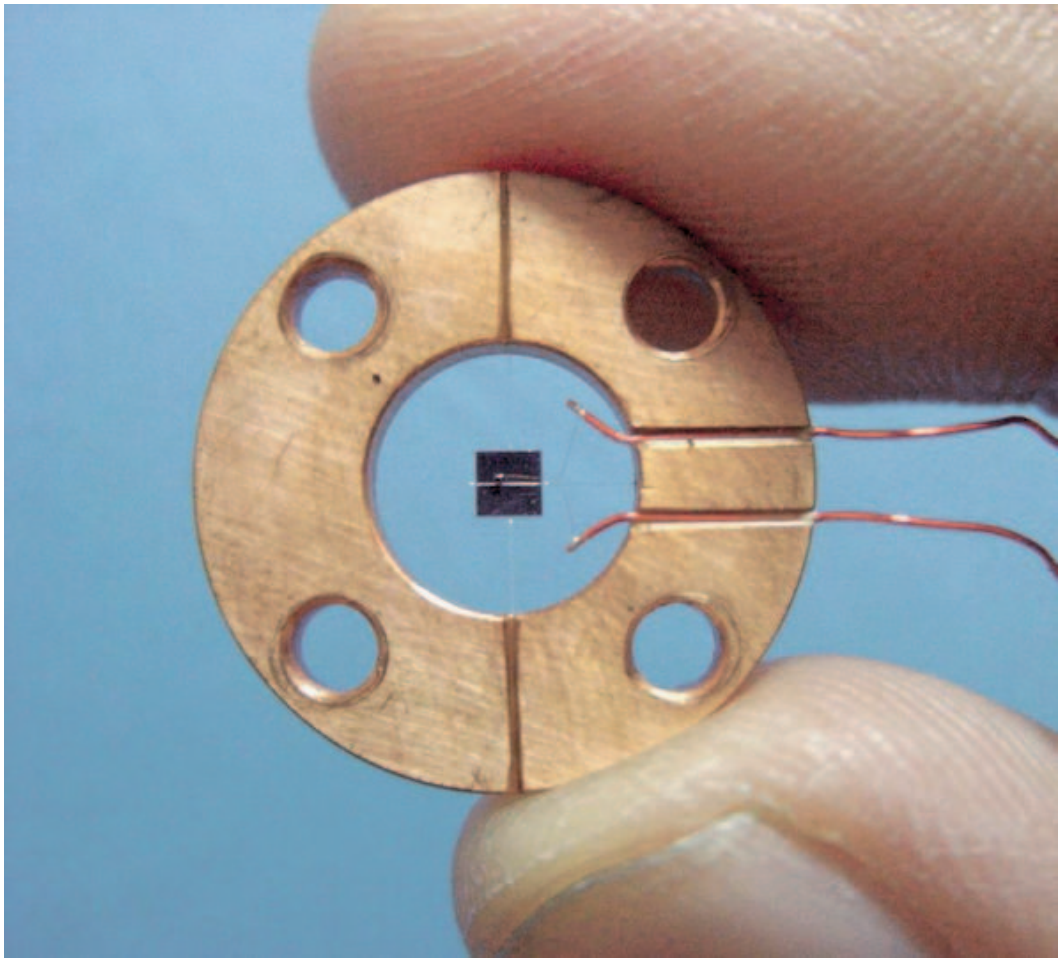

Figure 4.2: Bolometer unit details. The bolometer unit is suspended at the center of a brass ring by two nylons string that provide mechanical support. The two copper leads are connected to the 12 μm diameter NbTi leads that allows the electrical connection to the amplification stages.

are in error. Heat capacity, thermal conductance and the operation temperature should be chosen carefully in order to give the required performance for a given application. The next sections describe our detailed design of the composite bolometer.

4.1.1 Detector load and sky-power conditions

The FTS has been designed with the intention and goal to measured the broadband spectrum of the sky above Sierra La Negra. The bolometer is designed to work with two different experiments. The first experiment is a Total Power Sky Monitor (Ferrusca, 2006), which measures the sky power at 250 GHz with a bandwidth of $\sim$ 70 GHz. The second application, described in this thesis is the FTS, in which the bandwidth is defined by the natural cut-off of the Winston Cone at $\sim$ 200 GHz (low-frequency side) and the high-frequency cut-off of the flourogold filter at $\sim$ 1000 GHz. The background power level can be calculated as follows,

$$P(\nu, T) = \eta \epsilon A \Omega B(\nu, T) d\nu \tag{4.1}$$

where η and ϵ are total transmission of the system and the emissivity of the background respectively. The product AΩ is the throughput of the system and $B(\nu, T)$ is the Plank function. The effective Rayleigh-Jeans temperature for a blackbody is,

$$J(\nu, T) = \frac{xT}{e^x - 1} d\nu \tag{4.2}$$

where $x = h\nu/kT$, and therefore the Plank function in terms of the effective temperature is

$$B(\nu, T) = \frac{2k\nu^2}{c^2} J(\nu, T) d\nu. \tag{4.3}$$

We can now express the total power as follow,

$$P(\nu, T) = \eta \epsilon A \Omega \frac{2k}{\lambda^2} J(\nu, T) d\nu \tag{4.4}$$

where the throughput for a broadband system is $> \lambda^2$. It can be expressed as $N(\lambda) = 2A\Omega/\lambda^2$, where N is the number of modes. In general the power absorbed by the detector is,

$$P(\nu, T) = \eta\epsilon N(\lambda) k J(\nu, T) d\nu \tag{4.5}$$

The estimated sky-background power for sky-temperature of 270K is 20.7×10^{-9} W and the optical background power is 8.2×10^{-9} W for the useful bandwidth of $\sim$ 200 to 1000 GHz. Hence the expected total background power is $\sim 30 \times 10^{-9}$ W.

4.1.2 Operational temperature

Once the background power is estimated, we have to choose the operation temperature T_0. The choice of the operation temperature is not a trivial task because T_0 has a direct influence on the bolometer sensitivity and noise performance. Also the choice will depend on the refrigeration system available. Typical refrigeration systems are: an open system of liquid helium (L^4He), for temperatures of $\sim$ 4.2 K; pumped L^4He for range of temperatures $\sim$ 1.8 $-$ 1.2 K (depending on the vacuum level); a closed cycle system of L^3He for temperatures of $\sim$ 300 $-$ 200 mK; a L^4He/L^3He dilution refrigerator and adiabatic demagnetization refrigerator with temperatures as low as $\sim$ 100 mK. The contribution to the NEP depends strongly with the bath temperature T_0. In the case of a constant background the NEP goes as $\propto T^{1/2}$. The photon noise is independent of the temperature. In the case that T_0 has been chosen to keep a given frequency response, the NEP $\propto T^{5/2}$. Finally the choice should be driven by increasing the responsivity, where R $\propto NEP^{-1}$, in order to minimize the Johnson noise and amplifier noise.

Due to the strict financial limitations we have designed the bolometer to work in a temperature range of $\sim$1.6 K - 4.2 K, since a colder, more sensitive 300 mK system costs $\sim$ 50,000 USD. The cryogenic system of the MI-LAB is a liquid helium cryostat, in which is possible to pump directly on the liquid helium

reservoir to obtain a $T_0 < 4.2$ K. By reducing the vapor pressure above the liquid, temperatures down to 1.2 K can be obtained. Our system system is able to attain a stable temperature at 1.8 K.

4.1.3 Thermal conductance

In general the thermal conductance G of the thermal link depends on the temperature gradient, cross-sectional area, length and material composition. The temperature distribution along the thermal link will depend on the bolometer temperature T_b and the heat sink temperature T_0. By the definition the power passing through the thermal link is equal to the thermal conductance times the temperature difference across the link (Eq. 3.1). Eq. 3.32 relates the geometry and material composition of the thermal link, which is used to design a given value for G. In order to determine G in terms of a constant background power i.e. $Q = P$, we set a temperature rise ratio $(T_b - T_0)/T_0 = 0.5$, where T_b is the bolometer temperature. Under that condition the required thermal conductance is calculated using the next expression,

$$G = \frac{2Q}{T_0}, \tag{4.6}$$

and hence the thermal conductance is $G \approx 3 \times 10^{-8}$ W/K. The electrical leads dominate the thermal conductance in a bolometer. Then choice of the electrical leads is driven by the required value of G. Nevertheless there is not a wide variety of materials and it is not easy to select a suitable one.

We chose to use copper clad NbTi wires as the electrical leads. This material has been characterized partially at temperatures below 1 K. Reported values of G are: 4.7×10^{-10} W/K at 375 mK Lee et al. (1998), 7×10^{-11} W/K at 315 mK Mauskopf et al. (1997), and a G$\sim 1 \times 10^{-9}$ W/K at 4.2 K is reported (Lakeshore Inc. datasheet). From a linear interpolation to the thermal conductivity, we obtained a G$\approx 3 \times 10^{-9}$ W/K, which is ~ 10 times lower than the required G under

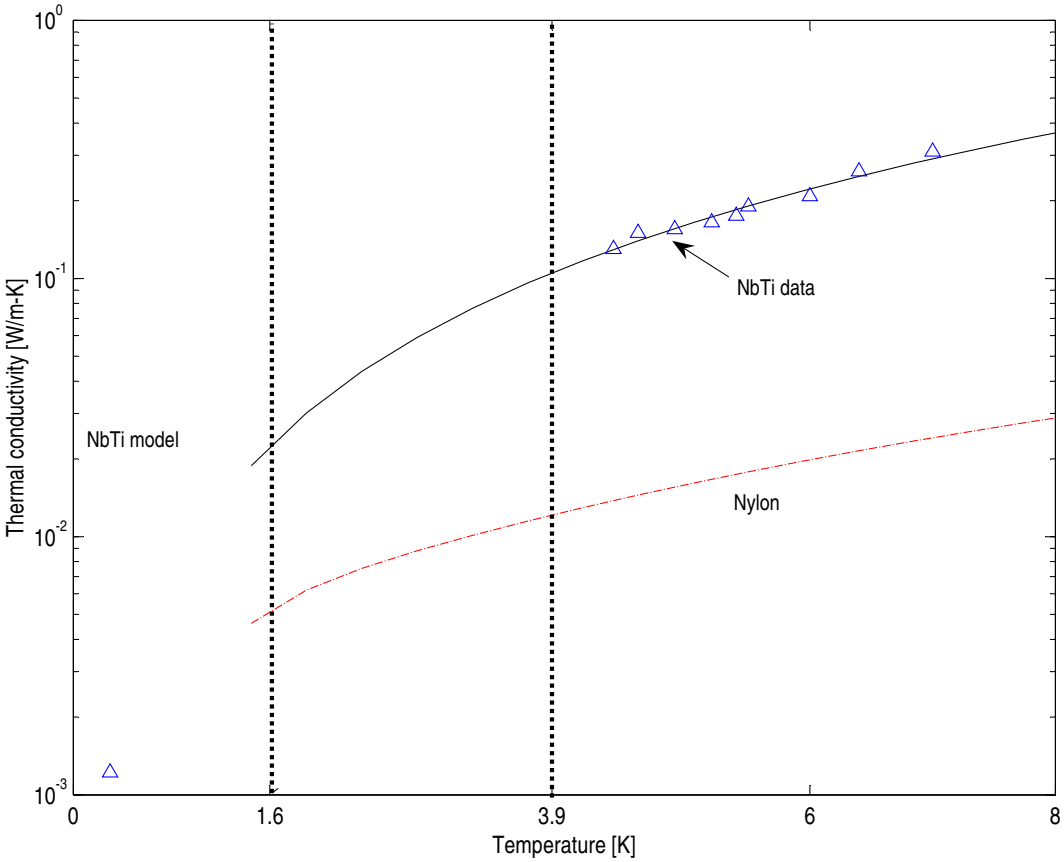

Figure 4.3: Thermal conductivity model for NbTi. The data shown with triangles are the experimental values reported in literature. The solid-line is model for a temperature range ∼1.5 - 8 K. The vertical dotted-lines shows the temperature range used for the bolometer characterization.

constant background conditions. The absorber-thermistor unit is suspended by two additional nylon supports, which have negligible contribution to the total thermal conductivity, therefore the total thermal conductance estimated for our bolometer at 1.8 K is $\sim 3 \times 10^{-9}$ W/K. Figure 4.3 shows the thermal conductivity of the materials used for the bolometer construction and this quantities are geometrically related with the thermal conductance.

4.1.4 Heat capacity and time constant

The total heat capacity is an important value because it defines the frequency response of our device ($\tau = C/G$). The area of a bolometer must be larger in order to maximize the absorption efficiency of the signal. A large area however will simultaneously increase the volume of the absorber unit and therefore the heat capacity of the bolometer. The larger the value of C, the slower the response time. The most significant contributions to the heat capacity are from the bolometer (i.e. thermistor plus absorber) and thermal epoxy. The values for the various heat capacities given in table 4.1 are uncertain due to the exact geometry of the components. For example, the application of thermal and conductive epoxies is difficult to control during the construction of the bolometer.

The total heat capacity of the bolometer is $\sim 2 \times 10^{-9}$ J/K and hence, when operating at 1.8 K, the maximum frequency response is ~ 1.5 Hz. The above is a disadvantage for the performance of the FTS-MPI. This slow response will affect the scan-speed increasing the time to record single interferogram. Therefore we are no sensitive to time scales lower than the time constant τ.

4.1.5 The bolometer absorber

The absorber has the function of improving the effective area of the bolometer and the absorption properties over the sub-mm/mm range. The absorber is a thin metallic film of bismuth with a sheet resistance $R_{\square}$ deposited on a thin transparent

dielectric substrate of sapphire (2×2 mm, 25μm thick). The sapphire is chosen to have a lower heat capacity than the thermistor. It also has a high strength that allows a very thin substrate, which conveniently reduces its volume and therefore its heat capacity.

In order to obtain a frequency-independent absorptivity, the metal film is placed away from the incident radiation (i.e. back side of the sapphire substrate) and the sheet resistance is selected to be $R_\square = Z_0/(n-1)$, where $Z_0 = 377\ \Omega$ is the free space impedance and $n \sim 3.2$ is the average refraction index of the sapphire, giving as result $R_\square = 171.3\ \Omega/\square$. The metallic film matches the free space impedance with the impedance of the dielectric substrate. This prevents reflections and hence there are no interference fringes, and therefore the absorptivity A is independent of frequency. Using Eq. 4.7 given by Nishioka et al. (1978), which takes into account the metal film and the dielectric substrate, we are able to estimate the absorptivity,

$$A = \left| \frac{4n}{(1+n)^2} \right| \frac{4 Z_0 n R_\square}{|R_\square(1+n) + Z_0|^2}. \tag{4.7}$$

For our configuration of bismuth-sapphire, we calculate that A is $\sim 49\%$. The table 4.1 summarises the physical dimensions and expected values for the thermal conductance and heat capacity.

		Dimensions					
Element	Material	X [μm]	Y [μm]	Z [μm]	Qty	Heat Capacity [pJ/K]	Thermal conductance [nW/K]
Thermistor	NTD Ge	250	250	250	1	271.453	-
Contacts	Au	250	250	1	2	0.447	-
Substrate	Sapphire	2000	2000	25	1	25.613	-
Film	Bismuth	2000	2000	0.035	1	44.164	-
Epoxy	Silver	78.9	78.9	78.9	2	27.437	-
Epoxy Th	StyCast	74.3	74.3	74.3	2	506.597	-
Wires	NbTi	-	12	5000	2	26.383	3
Supports	Nylon	-	31.8	5000	2	1200.52	-

Table 4.1: Bolometer dimension, heat capacity and thermal conductance

4.2 Detection system components

4.2.1 Cryogenics

The bolometers are devices that need to be cooled to cryogenics temperatures in order to maximize their performance. The bolometer is placed in a cryostat, which is a vacuum-tight enclosure. The cooling power of the system could be obtained by using liquid cryogens or mechanical coolers. In our case we use liquid nitrogen and liquid helium cryogens.

Our system is a 4.2 K cryogenic dewar from Oxford Instruments, Inc. (see Figure 4.4). The dewar consists of a stainless steel vacuum jacket at room temperature, a liquid nitrogen tank (LN_2) thermally attached to a radiation shield at 77 K, and a liquid helium tank (L^4He) that provides a 4.2 K stage. The L^4He tank has a vapor shield at $\sim$ 40 K. The radiation shields minimize the incom-

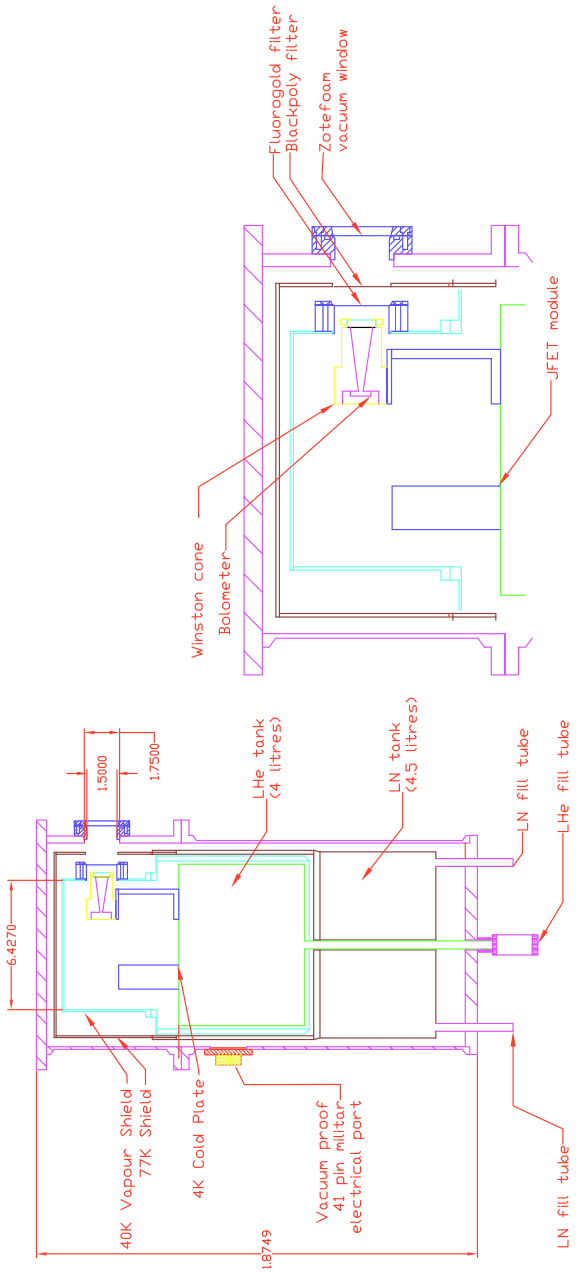

Figure 4.4: Modified experimental dewar from Oxford Instruments. Inc. The dewar is a liquid helium system with vapor-cooled and liquid nitrogen shields.

ing radiation from the warmer external stages. All the thermal stages are also super-insulated by wrapping them with many layers of aluminized Mylar. The LN_2 tank has a capacity of 4.5 liters and is suspended from the top plate of the vacuum jacket from three stainless steel supports that also act as fill tubes. The L^4He tank has a capacity of 4 liters, and is attached to the bottom of the LN_2 tank. The L^4He tank is suspended by a coaxial stainless steel tube which also serves as the fill port. Three fiberglass rods provide a rigid support to the L^4He tank and keep it centered. The 4.2 K stage is gold-plated aluminum that provides a good thermal contact and low emissivity. This stage serves as a cold bench, which we attach those components that require cooling to $\sim$1 - 4 K.

Temperatures in the dewar are monitored with diode thermometers (DT407) and are read out with a temperature monitor (Lake Shore Cryogenics Inc, model 128). Initially the bolometer was mounted at the exit aperture of a feed-horn (Winston cone), which was mounted on a copper table, thermally insulated by four G10 legs. A weak thermal link is provided between the cold stage and the copper table in order to cool the table to the cold stage temperature. The thermal link allows us to change the temperature of the copper table by mean of a heater attached to the horn. This configuration was used to characterize the bolometer unit, as is explained in section 4.6. The bolometer is protected from the unwanted optical and IR radiation by using filters on the 77 K and vapor shield stages. To conduct the blanked load curves measurements we placed a metallic cover on the input aperture of the horn, in order to provide a 4.2 K shield, and covered the cryostat window with an aluminum plate.

4.2.2 Cooling-down process

In order to reach the operational temperature of the cryostat, a set of steps should be followed, as well as an appropriate schedule to cool down the system. An important issue to consider in the cooling-down process is the vapour shield

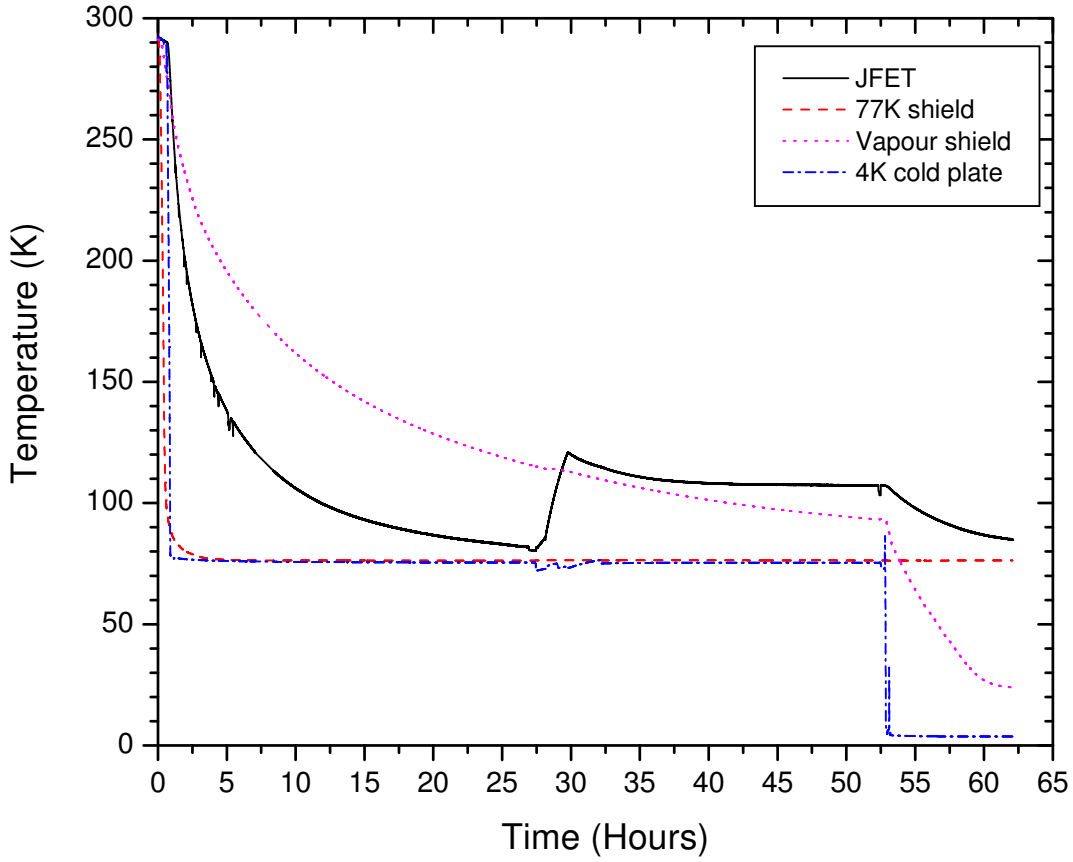

Figure 4.5: Cool down process chart of the different stages of the cryostat. The JFET is maintained at about 120 K using a heater.

stage. This thermal stage is designed to prevent thermal loading on the cold-plate. As was pointed out earlier this stage has a weak thermal link to the L^{4}He reservoir and it is cooled by the vapour produced in this reservoir. Due to this weak thermal link, the vapour shield takes several hours to reach the equilibrium temperature of $\sim$40 K. Therefore we follow the next steps to cool down the system:

1. Run the mechanical vacuum pump for at least 3 hrs to reach a vacuum level about 10^{-2} mbar.

Figure 4.6: Cooling-down process during the liquid helium transfer stage.

2. The system is then ready to be connected to the turbomolecular pump for at least 48 hrs to reach a vacuum pressure about $\sim 5 \times 10^{-3}$ mbar.

3. At this point we fill the LN and L^{4}He reservoirs with liquid nitrogen. After about 24 hrs the 77 K shield and the cold-plate reach the liquid nitrogen temperature, and the vapour shield reach a temperature about 100 K.

4. Once we reach these temperatures, we remove the liquid nitrogen from the L^{4}He reservoir by purging the tank with helium gas and wait until the base plate temperature is > 80 K to ensure any liquid nitrogen inside the reservoir has boiled off.

5. The liquid helium transfer is performed. The cooling-down takes about 18 to 20 hrs to reach a temperature of ∼3.9 K (boil-off temperature at 2200 m local altitude).

6. In case of a 1.8 K operational temperature we start pumping on the L^4He reservoir with the mechanical pump. The process takes ∼2 hrs.

The complete the cold-down process takes approximately 4 days to be ready for any experiment. Figure 4.5 shows the typical curve for the various steps involved in cooling-down process. Figure 4.6 shows a view of the laboratory during the liquid helium transfer.

4.2.3 Temperature stability at the cold-plate

When the system is working at 3.9 K the temperature of the base-plate is stable, however we have had a problem with the temperature stability at the detector. The figure 4.4 shows the mechanical drawing of the internal configuration and the position of the internal electronics on the baseplate. The bolometer is mounted at the back of the Winston cone, which is placed on a copper table close to the vapour shield. We identified that even with a good IR-blocking filtering there is a temperature gradient of ∼70 mK between the feed-horn and the base plate, which result in a strong dependence of the working temperature on the external power loading conditions. In order to solve this drawback we modified the cold optics.

The goal of the modification was to have a stable temperature across the body of the feed-horn and define a new field of view for coupling with the FTS-MPI. Greater thermal stability was achieved by placing the field optics directly to the cold plate. The original f/2.4 Winston cone however is not suitable for this option because the large acceptance angle (i.e. ∼ 22 degrees). Hence we designed a new feed-horn with smaller acceptance angle (∼12 degrees) than the

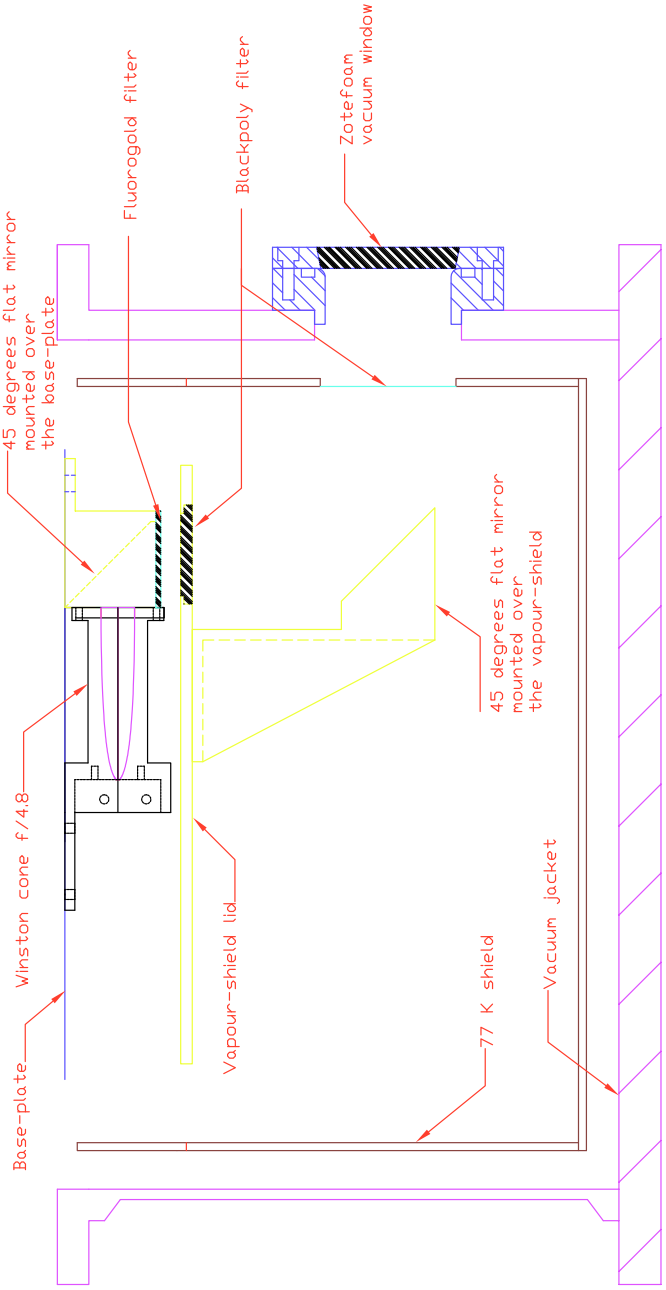

Figure 4.7: Modified configuration of the cold optics, to provide greater temperature stability of the bolometer and feed-horn.

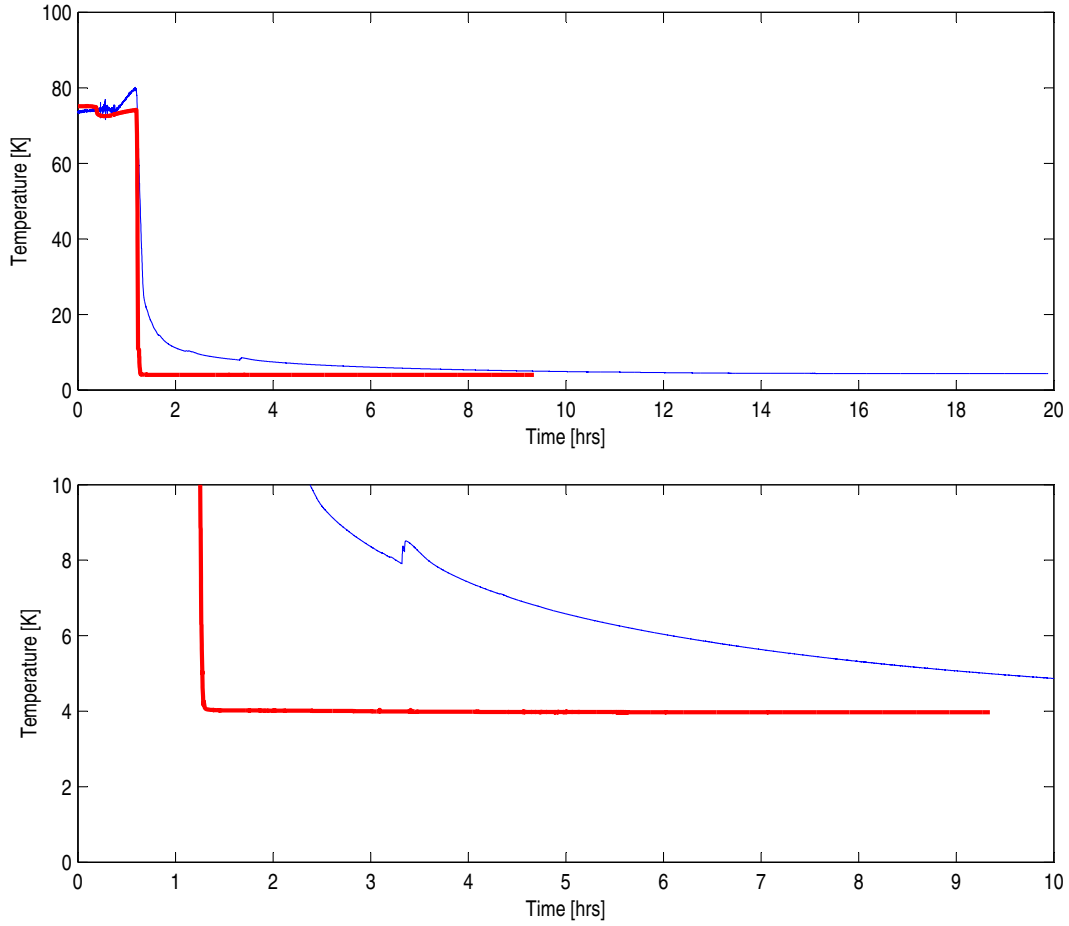

Figure 4.8: Cooling-down process. Base plate behavior during the cooling with the liquid helium transfer.

previous one. The characteristics of the new horn are described in Chapter 5. Figure 4.7 shows the details of the modifications in the internal optics. The fluorogold filter is placed over the base-plate 45 degree mirror in order to cool the filter to the bath temperature, and hence the re-radiation from the fluorogold filter will be reduced. Figure 4.8 shows the behavior of the cool down process after the improvements. The top panel shows the all the cooling-down process, the stabilization time is close 2 hrs after the liquid helium transfer, in comparison

with the old configuration that takes close to 12 hrs to be stable (see Fig. 4.5).

4.2.4 Read-out electronics

Figure 4.9 shows the basic scheme for the biasing and the readout of the sensor. The bolometer is biased with two 10 MΩ load resistors, R_L, in series. The resistor chain is symmetric in order to provide differential measurements. The bolometer is mounted at the exit aperture of the feed-horn and the load resistances package are screwed at the back of the horn on a small PCB circuit. In order to improve the power absorption of the bolometer we installed an aluminum plate to act as a back-short. The back-short also will allow better thermal conduction between the feed-horn and the load resistor package. The load resistor unit is at or close to the bath temperature in order to minimize its contribution to the Johnson noise and it is physically close to the bolometer unit in order to minimize the microphonic noise. The bolometer is connected to the high impedance pre-amplifier stage, which is a coupled pair SST/U401 JFET transistor configured in a differential follower mode in order to have high noise rejection.

The noise density contribution reported by the manufacturer is ∼5 nV/Hz$^{1/2}$. The JFET pre-amplifier is mounted on the cold stage (∼ 4.2 K), but is thermally isolated by a G10 tube. The working JFET temperature (∼ 120 K) is achieved by mean of a heater attached directly to the JFET module. The JFET pre-amplifier stage is also placed close to the bolometer unit in order to reduce the length of the connection wires and hence reduce microphonic pick-up through the wires. The detector is connected to the pre-amplifier stage with twisted pair of manganin wires in order to null the magnetic interference and these twisted pair were made as short as possible and held in place with Stycast 2850. The next stage is an amplification system (at room temperature), which provides a gain to the output signal coming from the JFET module. The amplifier uses an instrumentation amplifier AD624AD from Analog Devices, designed to have both AC and DC

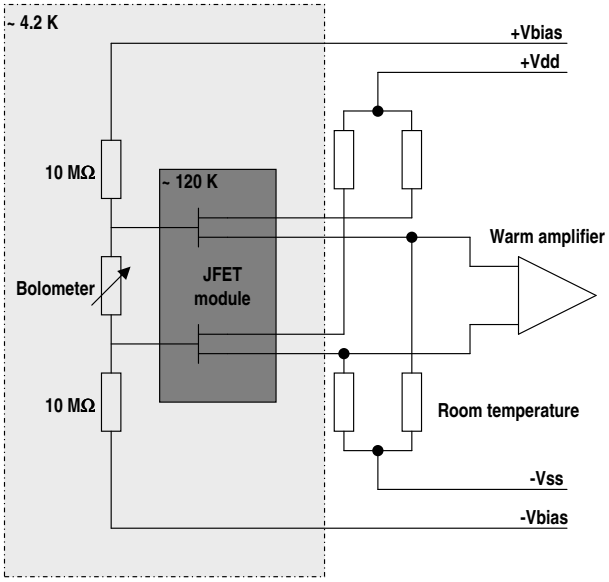

Figure 4.9: The bolometer schematic circuit for biasing and readout. The gray boxes show the different temperature stages.

outputs. The AC stage provides a differential output with selectable gains (i.e. 1, 2, 5 and 10). The AC output pass through an active bi-quad bandpass filter, designed to provided an additional gain of ~ 2.5.

The signal from the second amplification stage is then digitized by a digital acquisition (DAQ) system from National Instruments. The PCI-6024E DAQ is a 200 Ks/s, 12-bit system, that allows us to have 16 single-end and 8 differential analog inputs. The DAQ system is fully supported by the graphical program LabView, which we used to develop our graphical interface for control and data acquisition. A brief description of the acquisition and control software will be given in section 4.2.7.

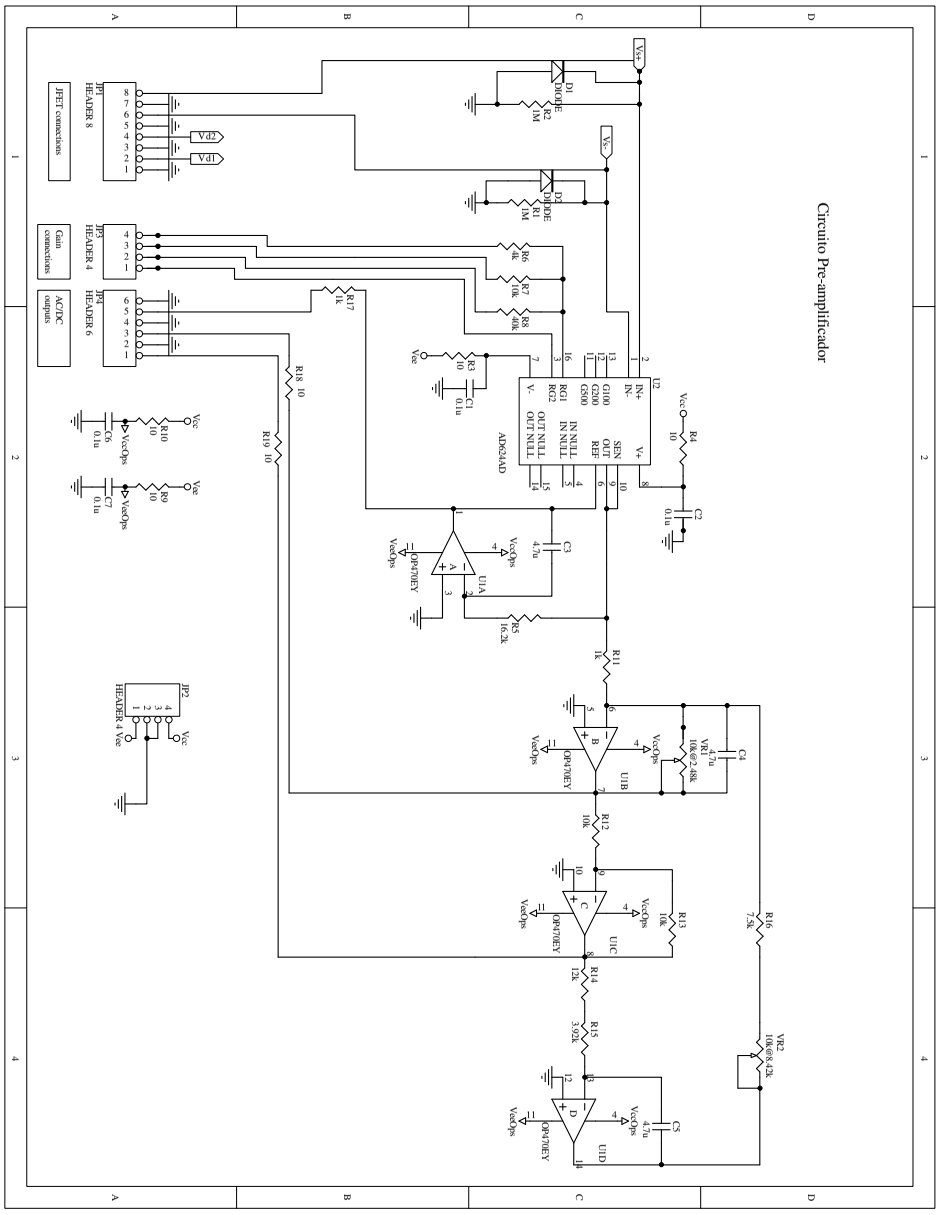

Figure 4.10: Schematic circuit of the warm amplifier stage. The stage composed with the AD624AD is the differential amplification stage which is coupled to a bi-quad bandpass filter builded with the OP470Y operational amplifier.

4.2.5 IR/FIR optical filtering

During the system tests where the bolometer is exposed to a source of radiation, the optical path is through the radiation shields and the vacuum window. The cryogenic dewar has a ∼25.4 mm thick Zotefoam vacuum window that transmits the incident power to the feed optics. That window also produces a thermal-loading on the base plate components, and it is infrared radiation that needs to be blocked. The IR-blocking can be achieved using a material that is transparent to sub-mm and mm waves and, at the same time, is very opaque to shorter wavelengths (i.e. optical and IR). The main characteristics of the IR filter are a low dielectric constant and minimal absorption at sub-mm and mm waves in order to minimize reflective and dissipative losses (Lamb, 1993). At IR wavelengths the filters should be highly absorptive to reduce the transmission of the IR radiation and with low emissivity to avoid re-radiation to colder stages. Therefore the IR filter has to be thermally attached to the cold stages, i.e 77 K stage and/or vapor-cooled shield at 40 K. Another characteristic and requirement of the filters is a high thermal conductivity in order to have a strong thermal link between the filter and the cold-stage, which provides a low thermal impedance path to the incoming radiation.

The need to optimize the physical properties (i.e. refraction index, absorptivity, thermal conductivity, etc.) of the IR filters requires a careful selection from a variety of materials: e.g. PTFE (Teflon), StyCast HiK, fused quartz, crystalline quartz and Fluorgold (glass-filled Teflon), HDPE (High Density PolyEthylene), Zitex (expanded PTFE), GoreTex (expanded PTFE), which have been used widely in sub-mm/mm, microwave and radio wavelength instruments. Table 4.2 summarizes the sub-mm and mm waves properties for the most of the above materials.

Due to our availability of materials we decided to use a $\sim$ 0.25 mm thick black-polyethylene (as IR blocking filters) at the 77 K stage and at the 40 K

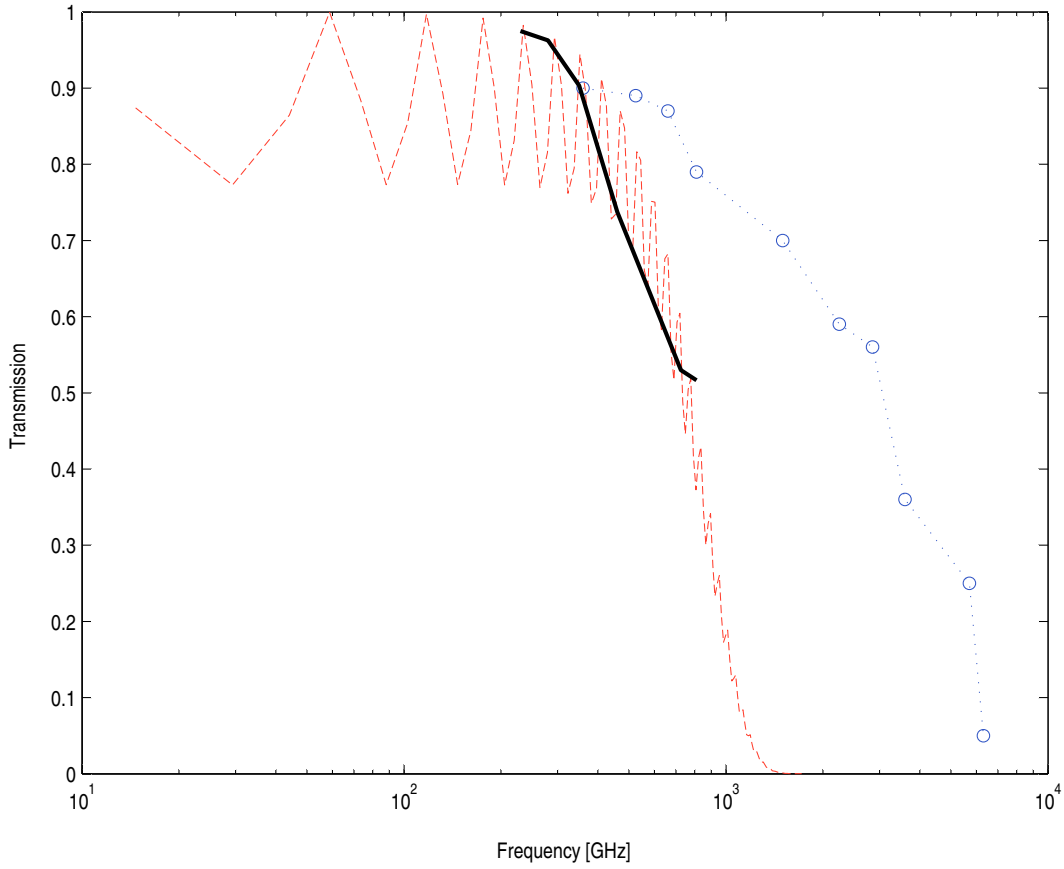

Figure 4.11: Transmission characteristic for materials used for FIR/IR filters in the detection system camera. The red-dashed line is the model for fluorogold transmission with a thickness of ∼1.25 mm (Halpern et al., 1986); the circle data shows the transmission characteristic of the black-polyethylene (Blea et al., 1970); the solid line is a modified data of the Zotefoam losses reported by Kooi et al. (1998).

Material	Refractive index	Losses	Frequency
Fluorogold	1.62 (parallel to grain)	6×10^{-3}	300 GHz
	1.60 (perpendicular to grain)	4×10^{-3}	300 GHz
Fluorsint	1.87	5×10^{-3}	300 GHz
PTFE	1.44	2×10^{-4}	90 GHz
Quartz, crystalline	2.11 (ordinary)	8×10^{-4}	900 GHz
	2.16 (extra ordinary)	5×10^{-3}	600 GHz
Quartz, fused	1.95	3×10^{-3}	600 GHz
StyCast HiK	2	-	

Table 4.2: Parameter used for model bolometer

vapor shield. For the cut-on filter we used ∼1.2 mm thick fluorogold cooled to the same temperature as the bolometer (i.e. the bath temperature). For the vacuum window we selected a Zotefoam (nitrogen-filled polyethylene foam). Zotefoam has excellent transmission over the frequency range 300 GHz to 900 GHz, and good vacuum properties. The black polyethylene is used as a low-pass filter which reduces the thermal load on the cold stage and helps to define the wavelength range of the radiation reaching the bolometer. The 40 K vapor shield filter is also necessary to reduce the thermal re-radiation load from the previous stage and again helps to define the bandwidth of the instrument. Figure 4.11 shows the transmission characteristic of our filtering system.

4.2.6 Coupling optics

Due to the increase of heat capacity with area, and the dependence of the bolometer time constant on heat capacity, the device becomes slow to respond. On the other hand the radiation absorption increases with an increase in the size. Therefore, a large concentration of the incident radiation is required to increase the absorptivity, without increasing the size of the detector.

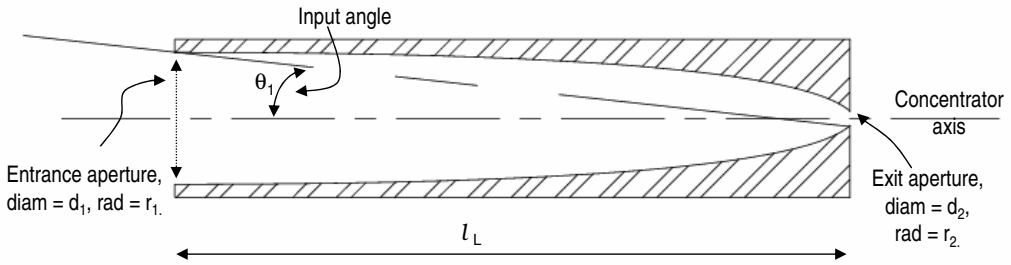

Figure 4.12: Winston cone geometry. The field of view is defined by the acceptance angle θ, which depends on the total length of the cone and on the diameter of the entrance and exit apertures.

The Winston cone is a light concentrator commonly used in FIR astronomy, which maximizes the solid angle of a multimode throughput. This concentrator rejects the background power which arrives from larger angles than the cut-off angle θ_1. Therefore the Winston cone defines the field-of-view as well as the throughput the system. Figure 4.12 shows the schematically the physical parameters of the concentrator and figure 4.13 shows the photo of the machined feed-horn at INAOE, as well as the fluorogold IR-blocking filter and the JFET pre-amplifier module.

The physical dimensions of the concentrator for particular application are fixed by the choice of the f number of the optical system. The acceptance angle θ_1 is matched to the focal ratio f_{system} by the expression

$$\theta_1 = arcsin(\frac{1}{2f_{system}}). \tag{4.8}$$

The entrance aperture, which is defined by the radius r_1, is obtained by

$$r_1 = \theta_b f_{system} d_{system}, \tag{4.9}$$

where θ_b is the desired field-of-view, and d_{system} is the diameter of the coupling mirror. The above expression are taken as initial parameters, then the remaining relevant physical dimensions are the diameter of the exit aperture,

$$d_2 = \frac{d_1}{2f_{system}}, \tag{4.10}$$

and the length of the of the feed-horn,

$$l_L = \frac{(d_1 + d_2)}{2tan\theta_1}. \tag{4.11}$$

In order to match the concentrator to the optical system we require $\theta_1 = \theta_b$. Finally, we have to take into account the losses at the diffraction limit for a Winston cone, which has a wavelength dependence. The losses can be reduced by keeping the radius of the exit aperture, r_2, smaller than the diffraction disk,

$$r_2 \leq 1.22\lambda f_{system} \tag{4.12}$$

The final geometry of Winston cone used in the detection system is explained in detail in chapter 5 as part of the optical coupling to the detector, the mechanical and optical design of the FTS-MPI.

4.2.7 Acquisition and control software

The interferogram can be measured with the FTS-MPI in two modes, as was explained in Chapter 2. The step-scan mode was selected for its easy implementation. The translation track is a microprocessor-controlled servo-motor that allows serial communication protocol. The control interface was implemented with a graphical program LabView. The interface allows us to select the spectral resolution as well as the spectral range. These are the input parameters to

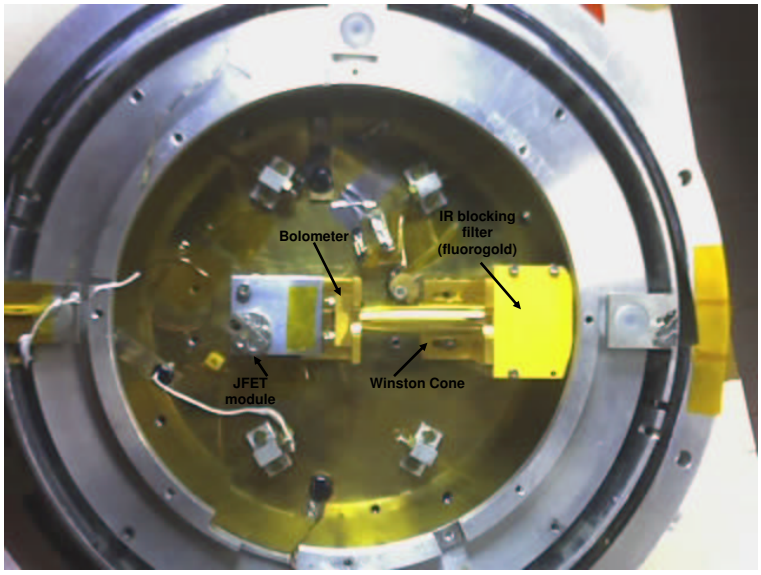

Figure 4.13: Inside view of the base plate of the criostat with the coupling optics and the IR-blocking filtering mounted in place.

calculate the size of step and the length-trip of the track. The program allows to us to manage the file storing directory and the name for data files adding a time reference to the record. The acquired data is plotted in a chart panel that allow us to inspect the data on real-time. Once the program has performed the scanning of the interferogram, it calculates the inverse Fourier transform of the data and plots the results in a second chart panel.

4.3 Expected performance

In order to determine the expected NEP, responsivity and time response, we must first understand the theoretical behavior for the bolometer based on the design parameters.

The V-I curve enables us to determine most of the performance parameters for the device. The power dissipated by the bolometer, due to the Joule effect, is

$$\begin{aligned} P &= I_{bias}^2 R_{bol} = V_{bol} I_{bias} \\ \text{and so,} \qquad I_{bias} &= \sqrt{P/R_{bol}}, \qquad \text{or} \qquad V_{bol} = \sqrt{P \cdot R_{bol}} \end{aligned} \tag{4.13}$$

The rate of heat flow out of the bolometer W,

$$W = P_{bias} + Q, \tag{4.14}$$

where P_{bias} is the power dissipated by the bolometer due to the bias current, and Q is the incident power. On the other hand, we know that in a steady state condition the thermal conductance G_0 depends on the bath temperature. The heat flow W passing through the thermal link is equal to the thermal conductance times the temperature gradient through the thermal link,

$$W = G_0 \cdot (T - T_0) \tag{4.15}$$

The dynamic thermal conductance G_d, which measures the change in the rate of heat flow W, caused by a change in the temperature T, is derived by taking the derivative of Eq. 4.14. In the case of a constant incident power we have,

$$G_d = \frac{dW}{dT} = \frac{dP_{bias}}{dT} \tag{4.16}$$

Using Eq. 4.16 and 4.14, we get the power dissipated by the bolometer,

$$P_{bias} = \int_{T_0}^{T} G_d dT - Q \tag{4.17}$$

Now, from Fig 4.3, we know that the thermal conductivity could be described by the power-law $G_0(T/T_0)^\beta$ and hence we can calculate the electrical power dissipated as follows,

$$P_{bias} = G_0 \left(\frac{T}{T_0}\right)^\beta (T - T_0) - Q \tag{4.18}$$

Using Eq. 4.18 we calculate the bias current and bolometer voltage as function of the temperature change of the bolometer. For a given set of parameters (β,

R_0, T_g, G_0 and Q) we can model a synthetic V-I curve at a bath temperature T_0. In the same way, the responsivity and NEP as function of the bias current can be modeled. The table 4.3 shows the model parameters.

Parameters	Values
β	1.7
R_0	68746.83651 Ω
T_g	38.41097708 K
G_0	7.7 nWK^{-1} at T_0
Q	0 (no optical loading)

Table 4.3: Parameters used for bolometer model in simulated V-I curves.

The parameters R_0 and T_g are physical parameters of the thermistor, which were obtained by linear fitting of the data showed in the Fig. 3.4 for the NTD Type-B thermistor from Haller-Beeman. The R-T characteristics of the thermistor are well described by the Eq. 3.6, with $n = 1/2$. The thermal conductance is modeled as a power law with $\beta = 1$, in the case of a metallic-link, or 3 for a crystalline dielectric-link. The thermal link consist mainly of two material (NbTi and Nylon) and that the thermal conductivity is dominated by the NbTi leads. Therefore, we adopted a value of $\beta = 1.7$ that results of fitting a power-law to the experimental data for NbTi, reported by D'yachkov (1979) (see Fig. 4.3).

The DC responsivity can be easily determined by substituting the impedance Z = dV/dI for a given load curve into Eq 3.15. Note that we are modeling the load curve without noise and with no optical loading. Figure 4.14 shows an example of the synthetic load curve for the parameters shown in table 4.3. The simulated load curve does not show the typical roll-off at higher bias expected for this device since the thermal conductance is defined to be constant as the temperature change. In contrast the roll-off shape of the experimental V-I curve, which results from the change of the resistance of the bolometer due to the heating of the Joule effect is present (see Fig. 4.18). The DC responsivity has a strong

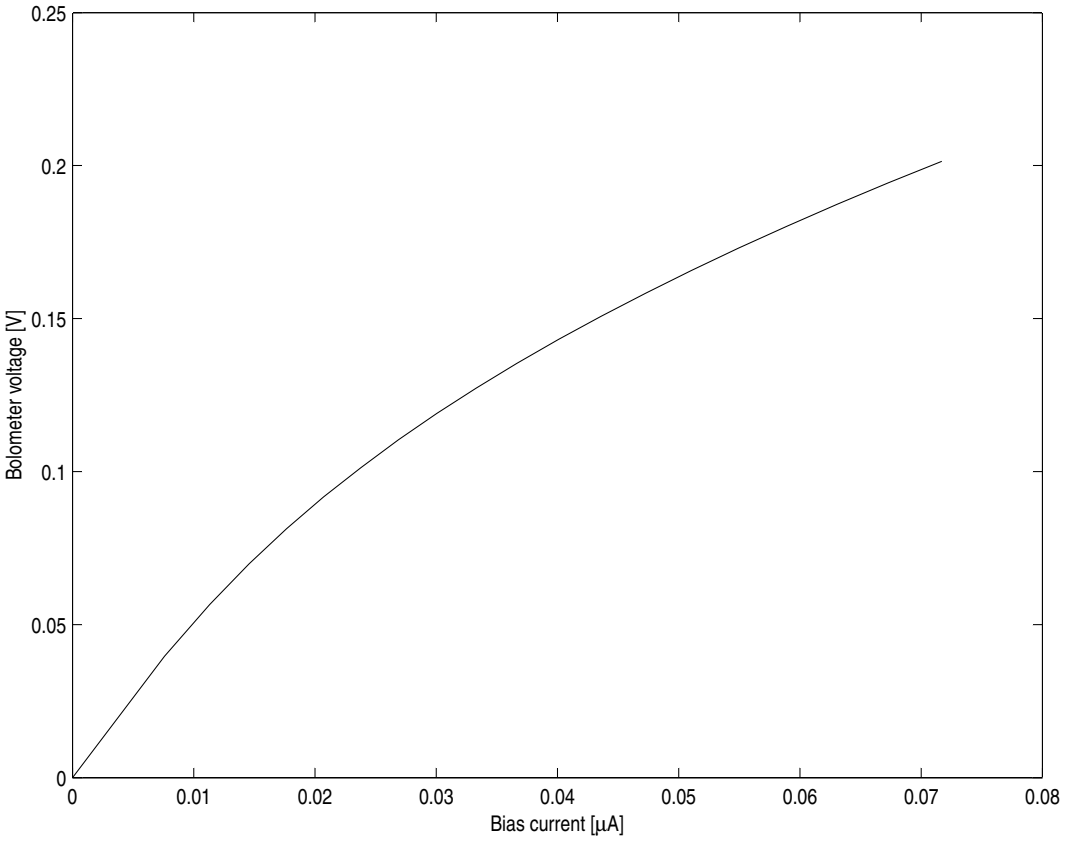

Figure 4.14: Synthetic voltage-current characteristic (load-curve) obtained using the model parameters in table 4.3, for temperature of 1.8 K.

dependence on the bias current (see Fig. 4.15). The higher values are in the low bias regime, where we get responsivity values close to $\sim 10^7$. The responsivity is not only a function of the bias current, but also of the background power Q. The NEP however shows lower values at higher bias current, and the NEP has a small dependence on the background power. Fig. 4.16 shows the NEP vs. bias current for the case of no optical loading. An important conclusion is the that current bias regime, used to optimize the behavior of the bolometer, which in this simulation is close to the $\sim 40 \times 10^{-9}$ A, gives values of S$\approx 4.5 \times 10^6$ V/W and

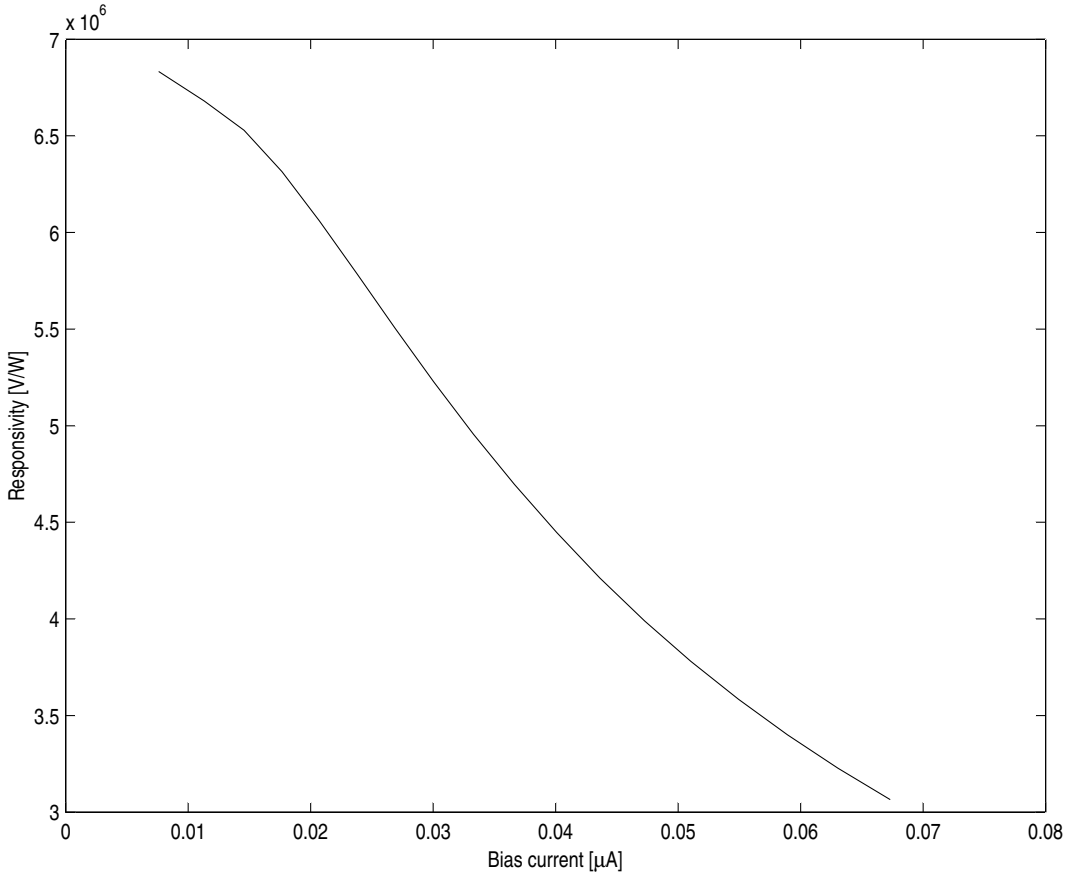

Figure 4.15: Responsivity vs. current obtained from the synthetic load-curve shown in Figure 4.14, for a temperature of 1.8 K

a NEP$\approx 4.5 \times 10^{-15}$ W$/Hz^{-1/2}$. The experimental characterization will allow us to verify the above values in order to determine whether the bolometer is able to measure the sky background. In the next section we examine the expected response on the FTS-MPI with the characteristics obtained in the simulation.

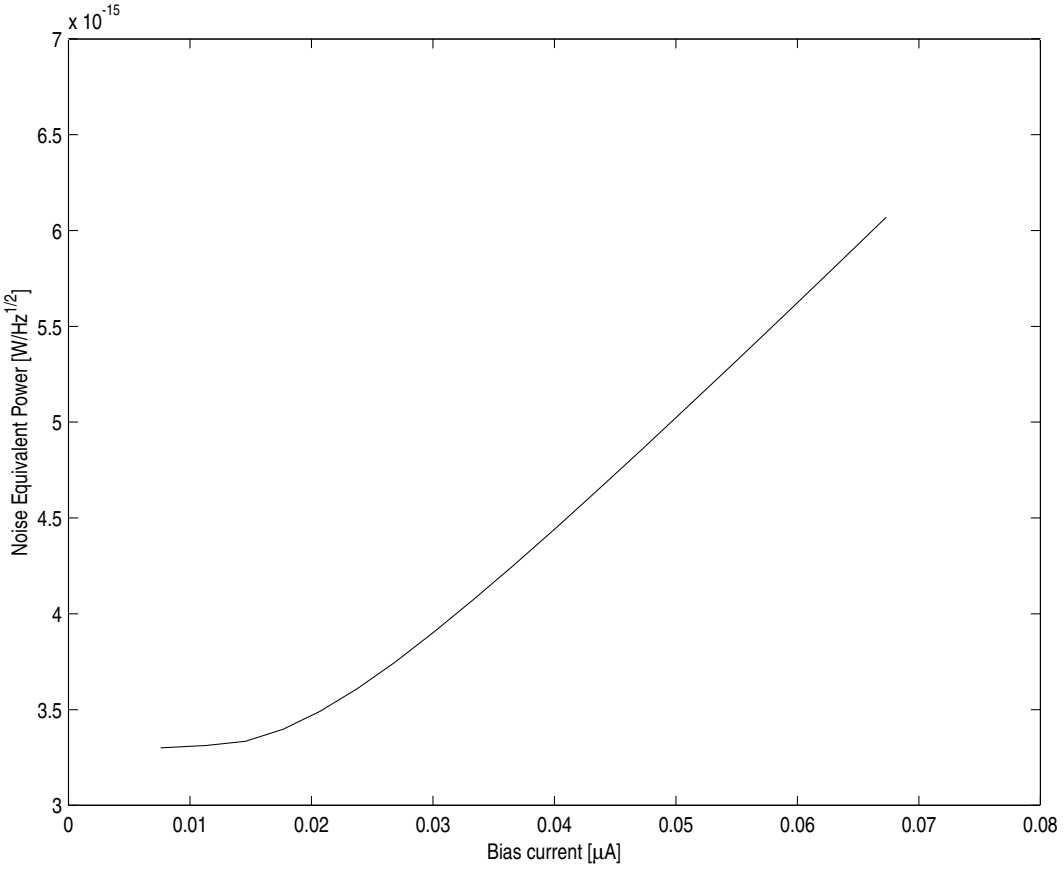

Figure 4.16: Noise Equivalent Power (NEP) vs. current, obtained from the synthetic load curve at T_0=1.8 K, the low bias regime was removed from the plot for clarity.

4.4 Experimental characterization of the bolometer

The goal of the bolometer characterization is to experimentally determine the physical parameters and the figures of merit (responsivity and NEP). In order to perform such characterization, blanked load curves (no optical load) were measured over a range of bath temperatures ($\sim 1.4 - 4.2$ K). We describe in sec-

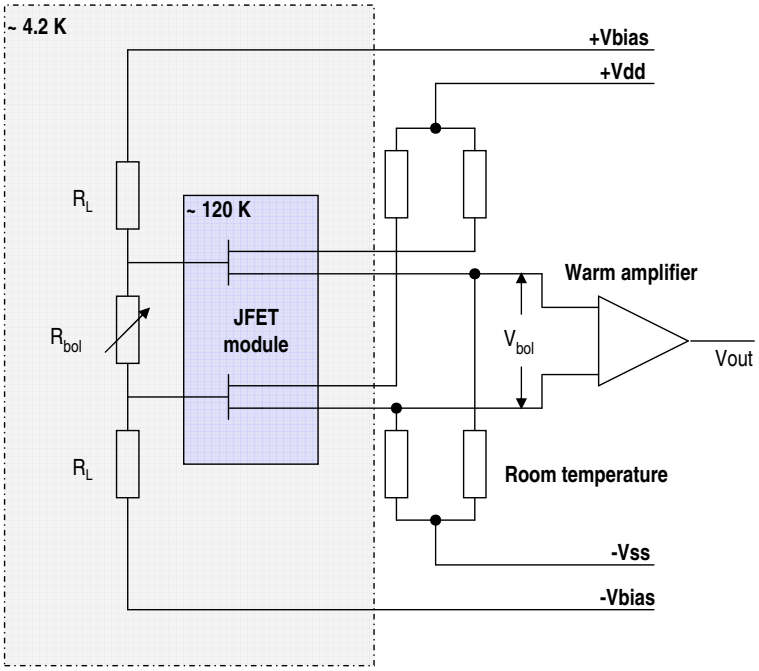

Figure 4.17: The bolometer block diagram for biasing and readout electronics. The bias current is obtained by measuring the V_{bol} at different values of V_{bias}.

tions 4.6 and 4.5 some experimental details to obtain the $R-T$ characteristic as well as the physical parameters of the thermistor used.

4.5 V-I curves

The voltage-current curves (V-I) allow us to determine the intrinsic characteristics of the bolometer. The V-I curves are obtained by measuring the voltage across the bolometer at different bias currents. Figure 4.17 shows a schematic of the circuit used to measure the V-I curve, where R_{bol} is the resistance of the bolometer at the bath temperature, and V_{bias} is the voltage across the resistor chain that produces the bias current I_b. The value of R_L (i.e. 20 MΩ) is chosen to be larger than R_{bol} in order to provide a constant current-bias circuit.

All the voltage measurements were made with the read-out electronics and the acquisition software system described in section 4.2.4. We automatized the V-I data measurement process by using the PCI-6024E DAQ board with a graphical interface programmed in LabView. The program sends a digital-ramp signal for biasing the bolometer circuit and records the output voltage signal from the read-out electronics. Then the voltage across the bolometer is related to the output voltage by,

$$V_{bol} = \frac{V_{out}}{A}, \tag{4.19}$$

where A is the total gain of the amplification system. The bias current is obtained by solving the loop formed by the two resistances R_L, R_{bol} and the bias source,

$$I_b = \frac{V_{bias}}{2R_L + R_{bol}} \tag{4.20}$$

or

$$I_b = \frac{V_{bias} - V_{bol}}{2R_L}. \tag{4.21}$$

Combining the Eq. 4.19 and 4.21 the bias current is,

$$I_b = \frac{V_{bias} - [V_{bol}/A - V_{off}]}{2R_L}, \tag{4.22}$$

where V_{off} is the voltage offset at the output when 0 volts are applied to the bias circuit. A set of V-I curves were recorded under conditions of no optical loading, whilst varying the bath temperature in order to derive the resistance-temperature characteristic, as well as, the performance parameter of the device.The load curves were measured at temperatures between $\sim$ 1.4 K to $\sim$ 4.2 K (see Fig. 4.18).

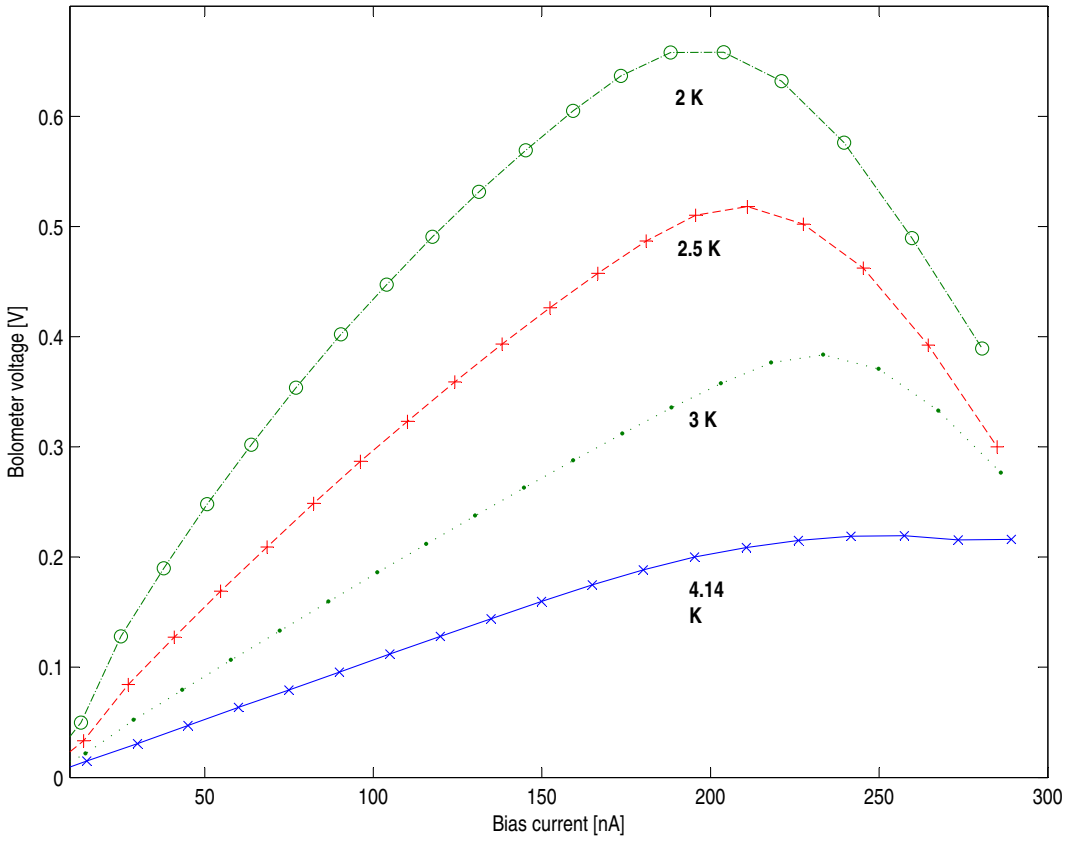

Figure 4.18: Load-curves set, for different bath temperatures: i) cross-blue line 4.14 K; ii) dotted-green line 3 K; iii) plus-red line 2.5 K; iv) circle-green line 2 K.

4.6 Resistance vs. Temperature

The temperature of the bolometer was changed with a heater attached to the horn. By stepping the bias voltage applied across the bolometer bias circuit and measuring the output voltage, we obtain each load curve. We are assuming a very good thermal contact between the horn and the bolometer, so that $T_b \approx T_{horn}$. The zero bias resistance R_0, at each temperature is determined by a linear fit to the low bias current regime of the load curve. The lowest temperature load-curves (< 4 K) were obtained while pumping down continuously with a

mechanical vacuum pump directly on the L^{4}He reservoir. As a result we are potentially sensitive to additional sources of external microphonic noise entering the cryostat. As we mentioned before, the resistance R_{bol}, is expected to vary with the temperature T (Eq. 3.6), then applying a linear fit to the log(R) vs. $1/T^{1/2}$ data, we are able to determine experimentally the values of R_0 and T_g. Fig 4.19, shows the linearized resistance vs. temperature characteristic of the

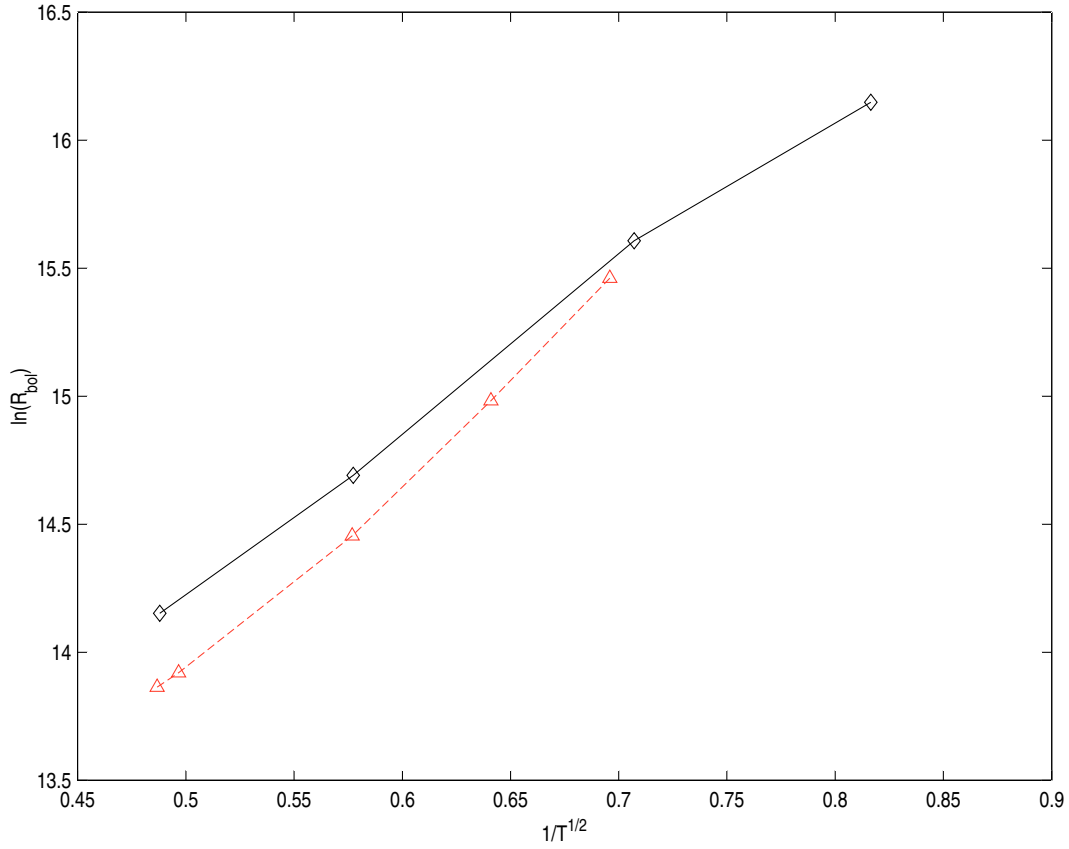

Figure 4.19: Log(R) vs. $1/T^{1/2}$ characteristic. The diamond points show the expected data from Haller type B thermistor; the triangle points show the experimental data for which $R_0 = 25412.59$ [Ω] and $T_g = 57.50$ [K] were obtained.

bolometer. These data are also compared to the reported data for a type B

thermistor from Haller-Beeman. The differences between the experimental data and Haller-Beeman data are still consistent within the errors in the measurements. The device does not show any significant heating from IR radiation leakages or thermal conduction leakages due to the wiring. Thus from the experimental data we obtained values of $R_0 = 25412.59$ [Ω] and $T_g = 57.50$ [K]. That does not affect the performance of the bolometer because the resistive coefficient is consistent with that obtained with the reported data.

4.7 Electrical responsivity

It is very important to establish the operating point of the detector in order to maximize the responsivity. The maximum responsivity is achieved for a value of Z ≈ 0, where the responsivity is $S(0) = -1/2I$. From the experiment measurements at $\sim$ 1.9 K and $\sim$ 4.1 K, we showed that the responsivity has a monotonically behavior.Fig 4.20 shows the responsivity versus bias-current at bath temperatures of $\sim$ 4.1 K and $\sim$ 1.9 K. The responsivity at $I_{bias} \sim 40$ nA for a temperature of $\sim$ 4.05 K is $\sim 1.4\times10^7$ V/W, and for a temperature of $\sim$ 1.9 K we derive $\sim 1.75\times 10^7$ V/W which represents just as small responsivity increment, that is because the results at $\sim$ 1.9 K were obtained pumping the L^4He reservoir, that process introduces noise due to large variations in the baseplate temperature. However the experimental value of the responsivity is at least one order of magnitude larger than that obtained by the simulation for about the same bias-current condition, i.e for a bias-current of $\sim$40 nA is $\sim 4.5 \times 10^6$ V/W.

4.8 Noise Equivalent Power

The measured NEP is related to the electrical and thermal noise contribution to the system. In principle all the sources of noise should be lower than the thermal noise, in order to achieve a background-limited system. From the blanked load

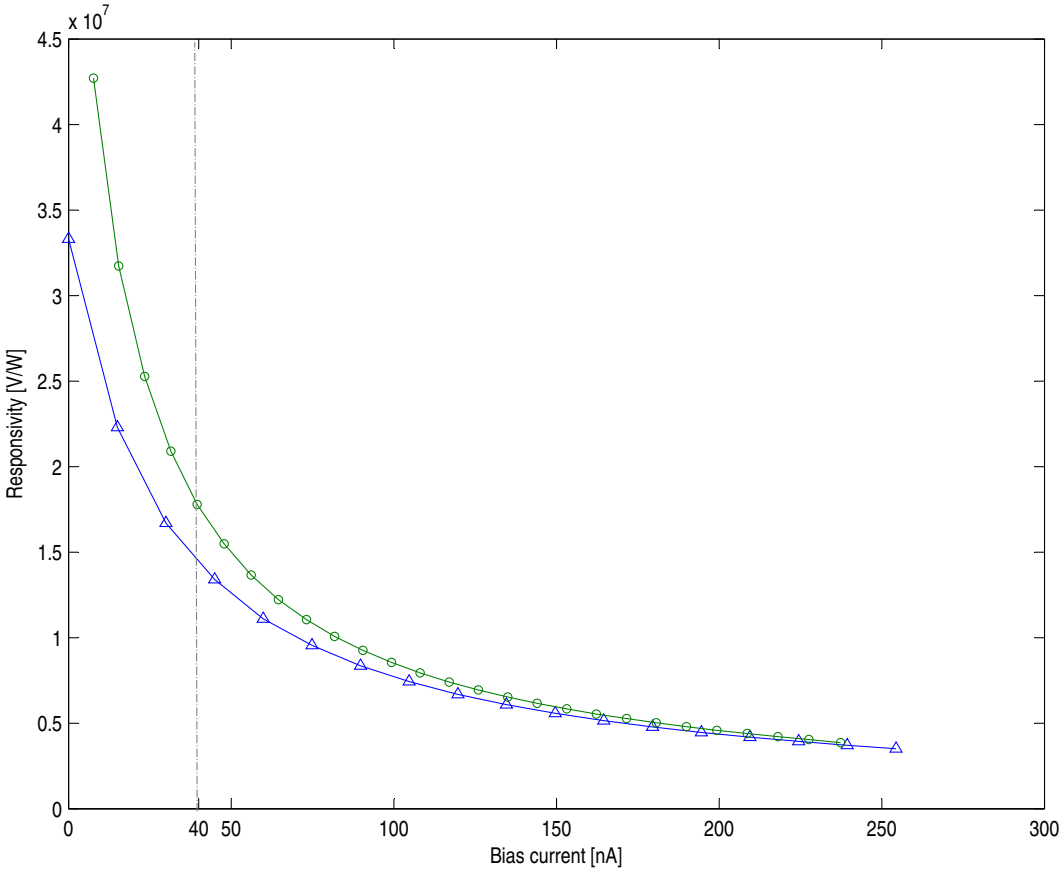

Figure 4.20: Measured responsivity vs. bias current for a bath temperatures of 1.9 K (green-circle line) and 4.05 K (blue-triangle line). The vertical-dashed line shows the operation point used for comparinson.

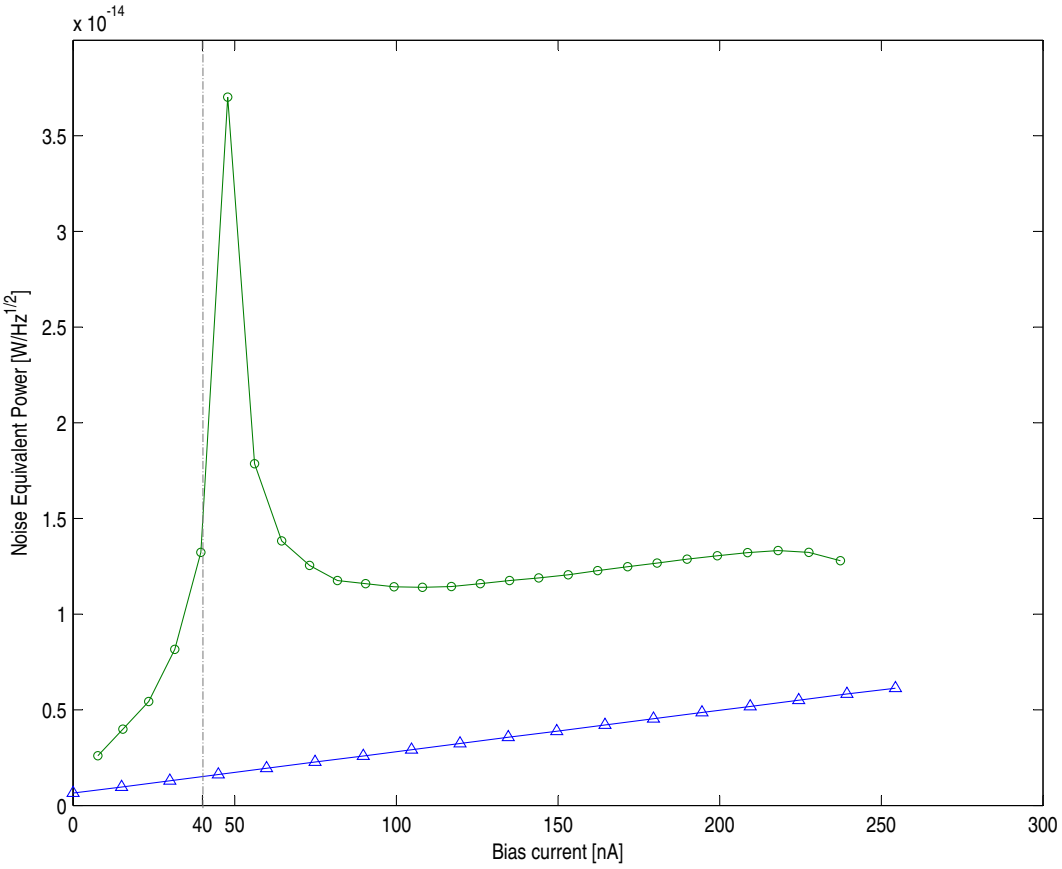

Figure 4.21: Total noise equivalent power vs. bias current, for different bath temperatures. Green-circles show NEP vs. I_{bias} at 1.9 K. The blue-triangles show the NEP vs. I_{bias} at 4.1 K. Operation point is shown with the vertical-dashed line.

curve at $\sim$ 4.2 K, we find an electrical (Johnson) noise excess, which degrades the total NEP. Figure 4.21 shows the total NEP contribution of the system for 1.9 K and 4.1 K bath temperatures. The green-circle line shows a not typical NEP curve, which is a clear effect of the bath temperature instability during the measurements. However the NEP for those experimental temperatures are in the order of $\sim 10^{-14}\, W/Hz^{1/2}$. Therefore it is clear that the best bath temperature to operate the FTS-MPI system is at $T_0 \approx 4.2$ K due to the more stable behavior of the system.

4.9 The bolometric system on the FTS

Finally we examine the behavior and suitability of the bolometer in the context of acting as the cryogenic detector for the FTS-MPI. As was explained in chapter 3 if the bolometer is operating in a steady-state, the power falling on the bolometer from a thermal source must equal the power dissipated through the thermal link G_0, which connects the bolometer unit to the heat sink (see equation 4.15).

In our case, that power, which the bolometer first measures, travels through the interferometer. The FTS-MPI can be used in a two-input port configuration, with one port looking at the source (e.g. room temperature baffles, the sky, etc.), and the second port looking simultaneously at a polystyrene cup of liquid nitrogen at $\sim$77 K, i.e. as a reference load. We can describe the power that reaches the bolometer, as a function of the optical-path differences, δ, as

$$I(\delta) = \frac{1}{2}(I_{LN} + I_{sky}) \pm \frac{1}{2}(I_{LN} - I_{sky})cos(\sigma\delta). \tag{4.23}$$

The first term represents the constant power which imposes a background on the detector. The second term is the signal of the interest that is detected by the readout electronics. The constant term in equation 4.23 is important because it will affect the temperature at which the bolometer operates, and therefore

its resistance. The second term which measures the difference between the two sources also contains the required information to calculate the power spectrum.

In order to know the change in the temperature of the bolometer due to a change in the incoming power we solve the equation 4.15 for temperature, i.e.

$$T = \frac{W}{G_0} + T_0 \tag{4.24}$$

Therefore variations in the incoming power will produce a change in the resistance of the bolometer. Using the R-T characteristic described by the Eq. 3.6 and the parameters used for modeling the theoretical behavior of the bolometer, and using Eq. 4.24, we calculate ΔR_{bol}. Using the Haller-Beeman R-T curve, the type B thermistor suggest a resistance-temperature ratio of $\frac{\Delta R}{\Delta T} \approx 0.98\ M\Omega/K$. Hence at $T_0 \approx 4.2$ K the expected value of ΔR_{bol}, when the interference term shows the maximum contrast, is $\sim 1.5\ M\Omega$. Therefore the bolometer has an expected $\frac{\Delta R}{\Delta T} \approx 1\ M\Omega/K$, which is in agreement with the thermistor chosen for the bolometer design.

Chapter 5

FTS: System Design and Integration

Fourier transform spectroscopy is a well established technique that is used in many research areas such as gas spectroscopy, optical materials, etc. Due to its ability to sample and study a wide frequency range, Fourier transform spectroscopy in astronomy has also become an ideal tool for atmospheric site characterization at sub-mm/mm wavelengths.

In Chapter 2, we have introduced the fundamentals in the analysis of data (i.e. interferograms) taken with a Fourier transform spectrometer. In Chapters 3 and 4 the basic theory of bolometers and the fundamental blocks of the detection system have been presented, as well as some details of the system integration and characterization. In this chapter we shall describe details behind the selection of the components integrated into our polarizing Martin-Puplett interferometer. Results of the laboratory tests will also be shown and discussed, as well as the analysis of synthetic spectra that allow us to evaluate the best strategy for the data reduction, and which help to understand the performance of the real system.

5.1 Fourier transform spectrometer design

A Martin-Puplett interferometer is a well-known configuration used in several fields of spectroscopy. Our goal is to build an interferometer with the appropriate characteristics to work in the areas of atmospheric spectroscopy, as well as optical material characterization at sub-mm/mm wavelengths.

From the point of view of an ideal spectrometer, a high resolution and large throughput system is desired. Large throughput will provide a good signal-to-noise ratio, by collecting more radiation power from a larger solid-angle. On the other hand, high resolution allow us to resolve fine spectral features. We should be careful to understand the final application however, in order to avoid unnecessary financial costs for the final system.

5.1.1 Spectral Resolution

We define spectral resolution by the frequency width that allows us to separate two spectral lines. Generally it is defined in terms of the maximum optical path difference δ. In practice we have to decide on a resolution that allows us to recover the profile of the atmospheric water-vapour emission lines (i.e. 183 GHz, 325 GHz, etc). For example the 183 GHz emission line has a FWHM of 5 GHz (Delgado et al., 2000) and, since we will use at least 5 point to describe the line profile, then $\Delta\nu \sim 1$ GHz. At this resolution we can define the maximum length of the translation stage, which is obtained from,

$$L = \frac{c}{2 \times \Delta\nu} = 15 \text{ cm}. \tag{5.1}$$

The length will increase if we take into account the apodization for the same resolution.

For the translation stage we use a linear-track from Servo System Co. with a useful length of 17 cm and a 1.27 mm pitch which was the minimum commercially

available pitch size. The motion is realized with a SmartMotor system which is a fully integrated control that features a servo motor.

5.1.2 Spectral range

The spectral range is given by the minimum mechanical resolution of the linear-track. Physically this is not always the true since effects introduced by the quality of the optical components will reduce the available spectral range.

In practice we define the highest frequency that we are able to resolve due to the optical elements. Mainly this high frequency cut-off occurs because the diffraction limit is imposed by: i) surface roughness; ii) physical dimension of the wire-grid polarizer; iii) uniformity of the grid.

Let us define the highest frequency first in terms of the wire-grid polarizer, where d is the wire grid spacing. Theoretically grids are expected to be efficient polarizers when $d/\lambda << 1$, but in practice, it is found that a better empirical relation is when $d/\lambda \leq 0.5$, which in agreement with measurements (Chambers et al., 1988). We are interested in the study of the atmospheric transmission profiles up to 1000 GHz. This high frequency cut-off is because of the larger atmospheric opacity at shorter wavelengths and because it is beyond the expected operational spectral regime of the LMT. Therefore, using $\nu = 1000$ GHz, we need a wire-spacing of 150 μm. However, we propose also to use the FTS-MPI for optical material characterizations, as an alternative application. In that case the surface quality of the optics will impose the highest frequency limit.

For material characterization applications, we also desire a wider spectral range in order to understand the optical properties of different materials over a wide range of frequencies. Based on the Raleigh criteria, which states that "the maximum wavefront error must not exceed a quarter-wave", we can determine the highest frequency of the system based on the surface quality. All the reflection optics were machined by the CNC machine of the INAOE Aspheric Laboratory.

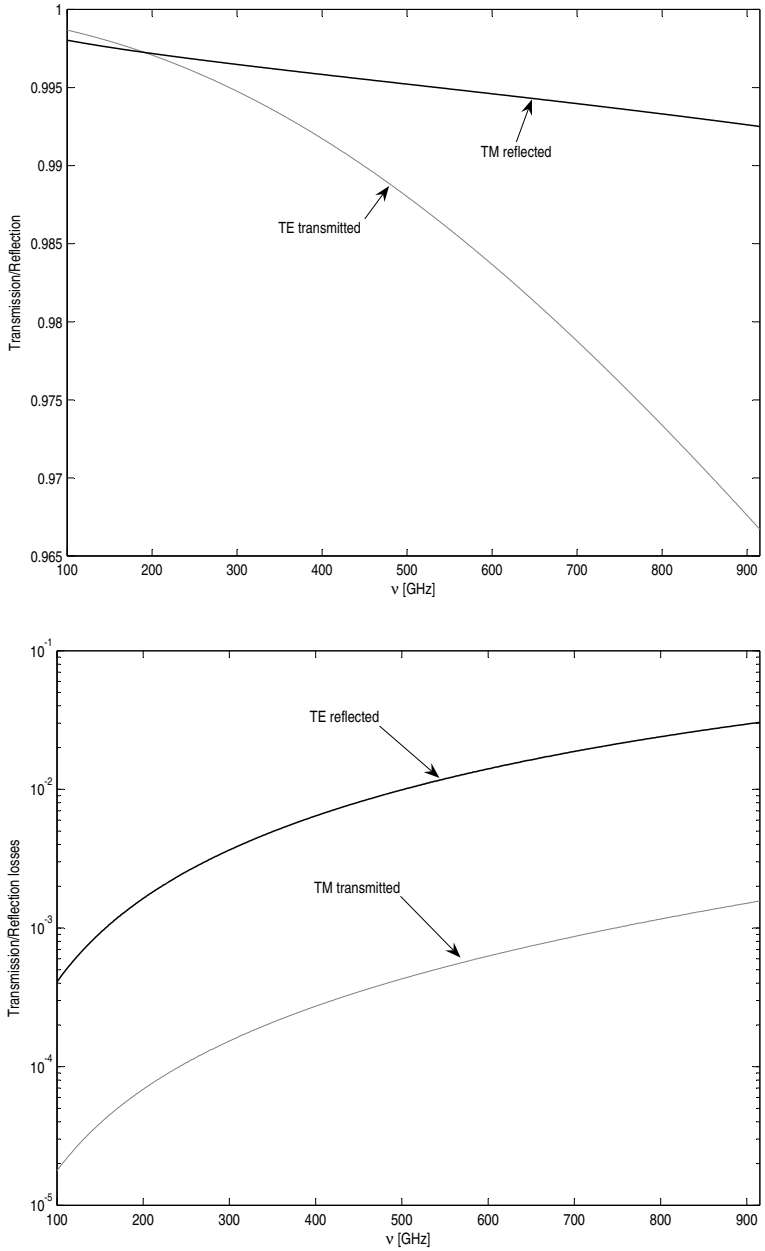

Figure 5.1: TE wave transmission and TM wave reflection characteristic for a incidence radiation at 45 degree.

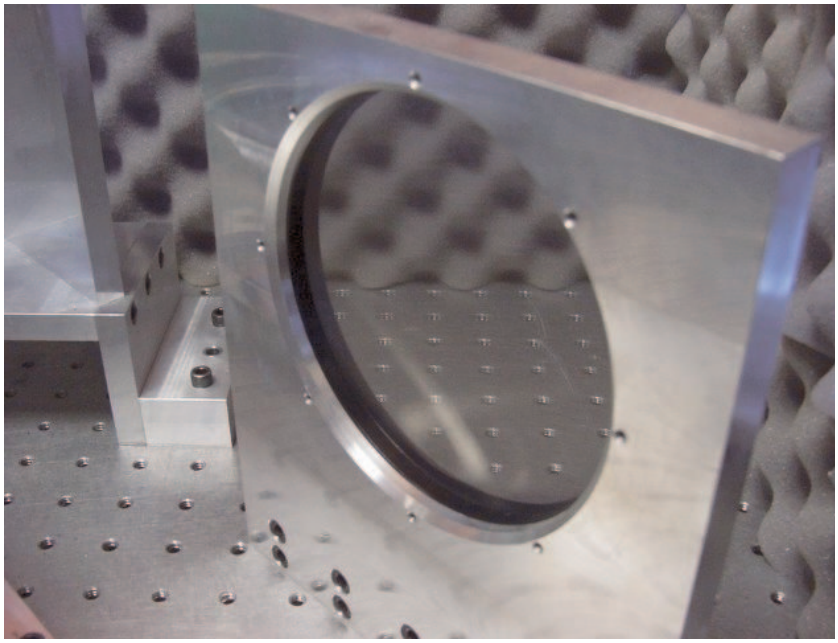

Figure 5.2: The 140 mm diameter tungsten wire-grid polarizer used as beam splitter for the FTS-MPI. Installed on aluminum mount.

The rms surface error of our optics is expected to be 10 μm which is due to the best finishing of the CNC machine. Therefore the maximum frequency at the diffraction limit will be 7.5 THz. Optical designers use a 1/10 wavelength "rule of thumb" in the most critical optical parts, which will reduce the spectral range, giving a frequency of 3.5 THz. Therefore the polarizer wire-spacing required for this limit is $\sim$43 μm. Unfortunately, we were not able to obtain the wire-grid polarizer with the required dimension, due to the unavailability in the commercial stock. The final dimensions of the tungsten wire-grid spacing is 75 μm, with a wire diameter of 25 μm, which implies a $f_{max} = 2$ THz (see Figure 5.2). Figures 5.1 show the expected performance of the wire-grid polarizer used as a beam-splitter (i.e. 45 degree input wave incidence) in the interferometer.

5.1.3 System throughput of the system

Initially the coupling optics of the system used a feed-horn with a focal ratio of 2.4 and an acceptance angle of 12 degrees. For this large acceptance angle, we had to use a copper table to raise the feed-horn and place it closer to the vacuum window in order to avoid vignetting. As was explained in section 4.2.3, this configuration is prone to temperature instability. The effective focal length of the system must be short in order to avoid a large-diameter optics that feed the concentrating horn with a 12 degrees acceptance angle. The use of large-optics is not really inconvenient, but it increases the cost of the system, due mainly to the polarizers which are the most expensive items. Consequently the size of the interferometer optics will be driven by the design of a good thermal stabilization of the detection system, and for a suitable frequency range that constrains the useful dimensions of the feed optics. Thus, in order to have a thermally-stable system, the coupling optics should be placed in direct contact to with the cryostat base-plate. The large acceptance angle of the original feed-horn however will cause the vacuum window to vignette the beam. Therefore we decided to change the coupling optics in order to have a clean beam through the vacuum window.

We establish the diameter of the focusing optics to be a value of 127 mm and the focal distance to be 610 mm. Therefore the f-number of the focusing optics is 4.8. With these parameters we are able to obtain the Winston-Cone dimensions. The acceptance angle of the Winston-cone feed-horn is

$$\theta_1 = arcsin\left(\frac{1}{2f_{fo}}\right), \tag{5.2}$$

where f_{fo} is the focal ratio of the focusing optics. Then fixing the angular diameter of the field of view to 1 degree, we can calculate the diameters of the input and output apertures, and the feed-horn length, using Eqs. 4.9, 4.10 and 4.11. The physical dimensions are shown in table 5.1.

The focusing mirror is a 90 degree off-axis parabolic mirror with an effective

Entrance aperture	10.16 mm
Exit aperture	1.0922 mm
Length	52.0325 mm
Input angle	6.17 deg
Focal ratio	4.8

Table 5.1: Dimesion of the $f/4.8$ Winston cone.

focal length (EFL) of 610 mm. The parent focal length (PFL) is 305 mm. The next expression describes the profile of the parabola center at (0,0,0),

$$z = \frac{x^2 + y^2}{4 \cdot PFL} - PFL. \tag{5.3}$$

Finally we have to specify the diameter for the wire-grid polarizers. The size could be fixed to the size of the 127 mm beam that travels through the interferometer. That however implies a diameter for the polarizer of ∼180 mm due to a beam incidence of 45 degrees. We decided to optimize the size of the optics using the consideration that a monochromatic gaussian-beam is propagating through the interferometer. Because the beam diameter is a function of the wavelength, we use the longest wavelength of the spectral range for the design which provides the upper limit for the physical dimension of the wire-grid polarizer. Assuming a feed system that has a focal ratio $f/4.8$ and $\lambda = 1.4$ mm, we expect a beam-waist of

$$\omega_0 = \frac{\lambda}{\pi\theta}, \tag{5.4}$$

where $\theta = 1/2 \cdot f_{fo}$, hence $\omega_0 = 4.3$ mm. The incident beam is collimated by the optics which are placed into the beam where the beam-waist is ω_0. The wire-grid polarizer is then placed at a distance of ∼230 mm from the collimating optics. With this arrangement we get a beam diameter of 48 mm. Therefore the recommended optics diameter for a 45 degree incidence is $2.82 \cdot \omega \approx 135$ mm.

The available size for the wire-grid polarizer was 140 mm, which was sufficiently close to the required size.

5.2 Optics machining

All the reflecting optics of the interferometer were fabricated at the Aspheric Laboratory of INAOE. The roof mirrors were fabricated into two sections in order to have a better definition of the *roof-line*. After machining they were polished at the optics shop to improve the flatness, the reflection, and consequently, the optical surface quality.

The interferometer has two identical off-axis parabolic mirrors for collimating and focusing. Both mirrors were fabricated with a CNC machine. The surface generation was provided by spline fitting of the CNC to the data points, which we provided. This method gave as result the best optical quality. Figure 5.3 shows the first step of the machining process, and figure 5.4 shows the final surface quality achieved by the CNC. We avoided polishing these mirrors because we were not able to test the surface quality during the process.

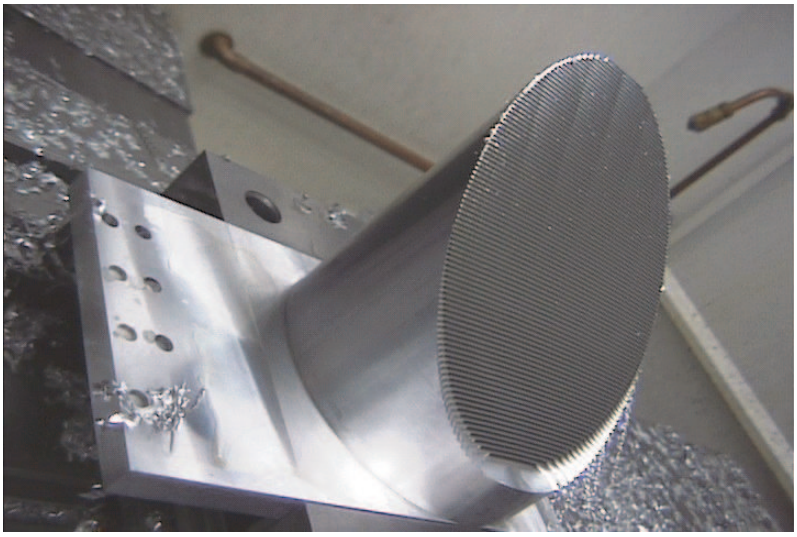

Figure 5.3: Off-axis parabolic mirror machining at CNC machine. The machine grooves are still visible after the first cut.

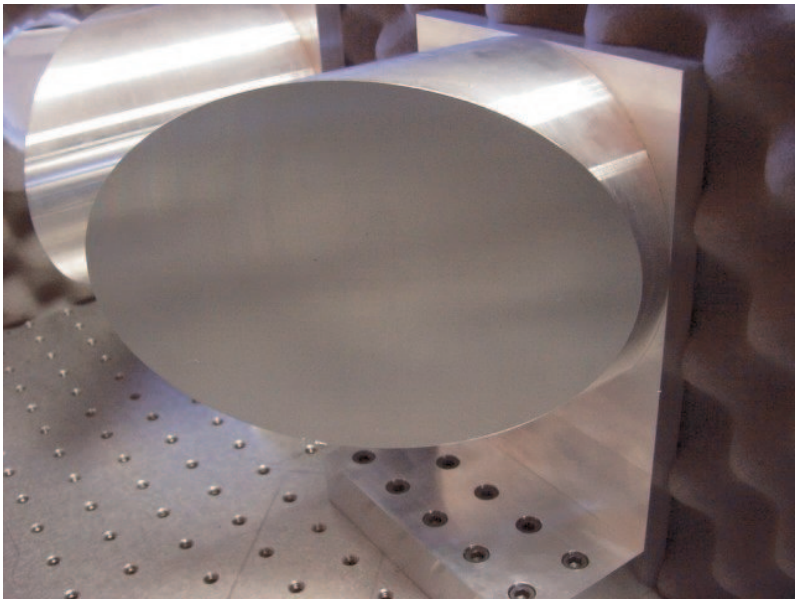

Figure 5.4: A 127 mm diameter, f/4.7 off-axis parabolic mirror showing the final surface quality.

Figure 5.5: Mylar beam-splitter, held in a 140 mm diameter aluminum ring, used for the aligning process.

5.3 Optics alignment

The only piece in the system that is not located at some fixed position is the detection system, and hence it was necessary to verify the alignment with a laser. The wire-grid polarizer at the shortest wavelengths (i.e. $\lambda < 150$ μm) behaves as diffraction grating. It is therefore impossible to use diffracted light for the alignment, and so we built a dielectric beam splitter using a sheet of transparent mylar. The mylar was tensioned and glued between two bolted aluminum rings with the same dimensions as the wire-grid polarizers(see figure 5.5).

The roof mirrors have sufficiently reflectivity for the laser, but in the case of the off-axis parabolic mirrors, these were temporarily covered with aluminum-coated mylar-tape in the central region in order to improve the reflectivity of the surface and to provide a brighter spot at the camera window.

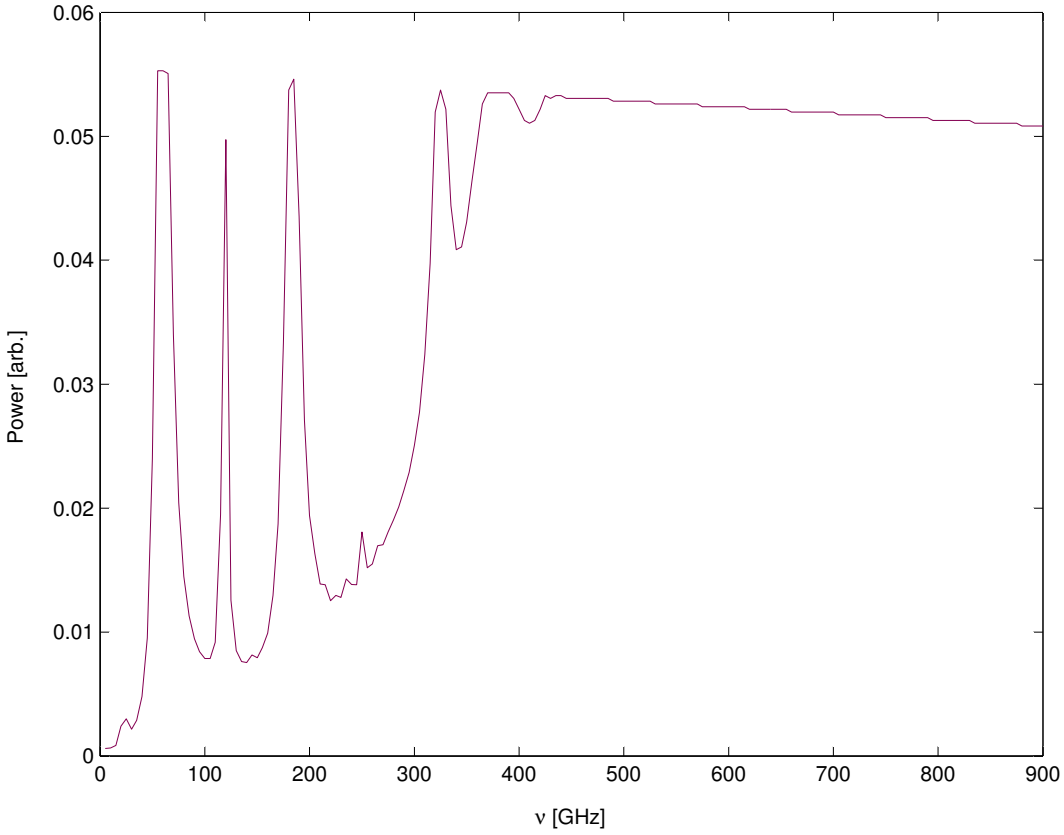

Figure 5.6: Power spectrum of the local atmosphere derived from the ATM code for 11 mm of PWV and ∼5 GHz of resolution.

5.4 Analysis of the spectral effect of Fluorogold filter

From section 4.9 we know the minimum characteristics of the detection system for the case of ideal blackbody point-like sources placed at the input ports. However, in this section we examine the effect of an extended greybody source, i.e. the sky and the blocking-IR filters. The development of this analysis is important because it will allow us to better understand the calculated spectrum.

Figure 5.6 shows the modeled power spectrum of the sky above INAOE (To-

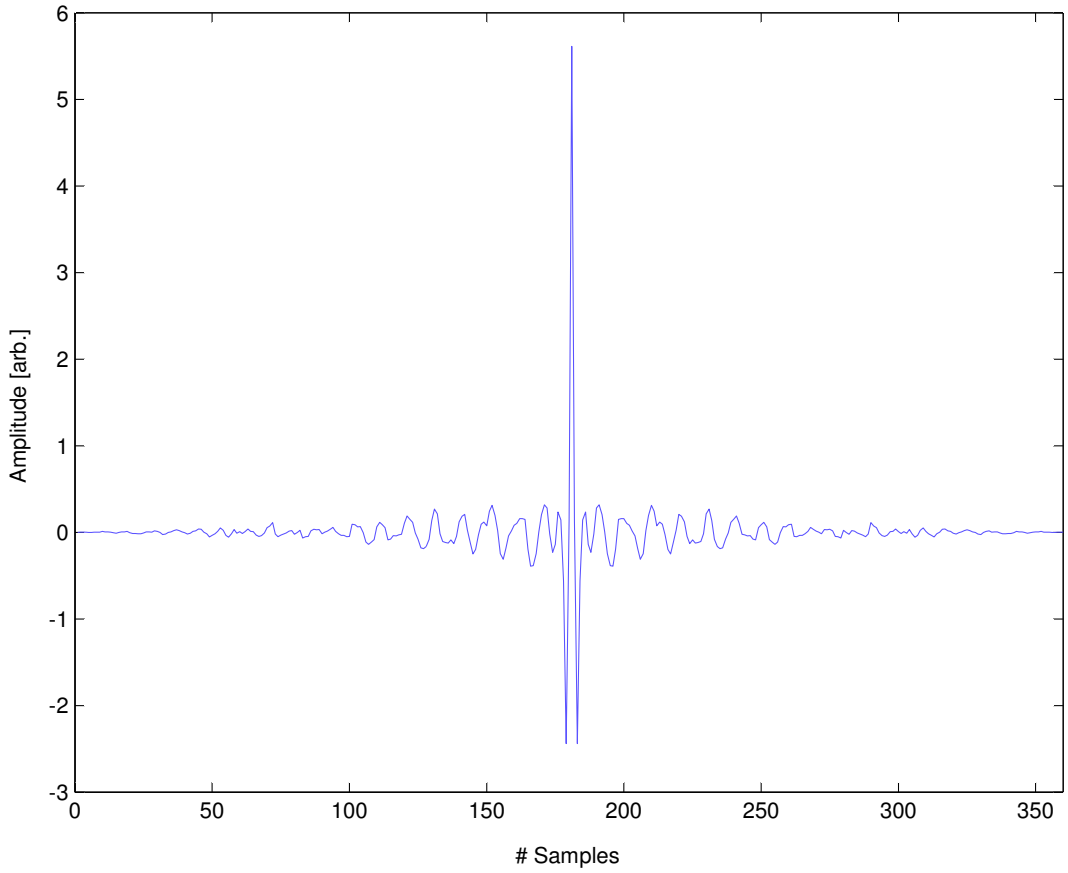

Figure 5.7: Simulated interferogram, obtained from transmission spectrum of the atmosphere derived from the ATM code, shown in figure 5.6.

nantzintla, Puebla at ∼2200 m). The model was obtained using an atmosphere that includes molecules of H_2O, CO_2, O_3, N_2O, CO, CH_4 and O_2. The model also assumes 11 mm of PWV in order to provide an spectrum with strong vapour water features, and a resolution of ∼5 GHz in order to match the spectral resolution of the fluorogold measured data. This sky power spectrum is convolved with the blocking-IR filter transmission spectrum (i.e. fluorogold). The transmission characteristic of the fluorogold was calculated using the data obtained during our previous experiments (i.e. 2002) with an FTS at the University of Pennsylvania.

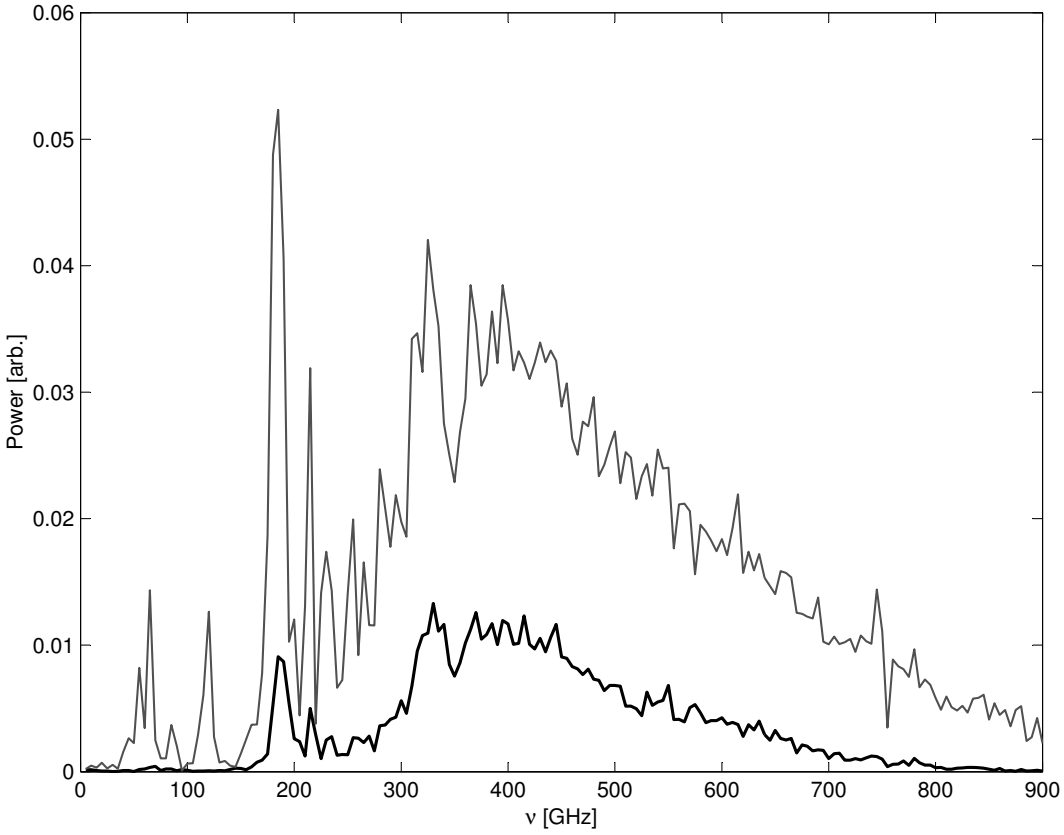

Figure 5.8: Power spectrum (solid-line) obtained by inverse FFT of the simulated of the real part of the interferogram in figure 5.7, which results in reduced signal strength. The dotted-line is the atmospheric power spectrum convolved with the fluorogold transmission characteristic.

The convolved spectrum is then Fourier-transformed in order to produce an interferogram. Figure 5.7 shows only the real part of the computed interferogram, since this is exactly what we measure with a detection system.

In order to compute the power spectrum from this simulated interferogram we then applied the phase correction method already described in section 2.1.6. Figure 5.8 shows the computed spectrum which has been attenuated with respect to the original convolved spectrum. The reduced power is because we intentionally

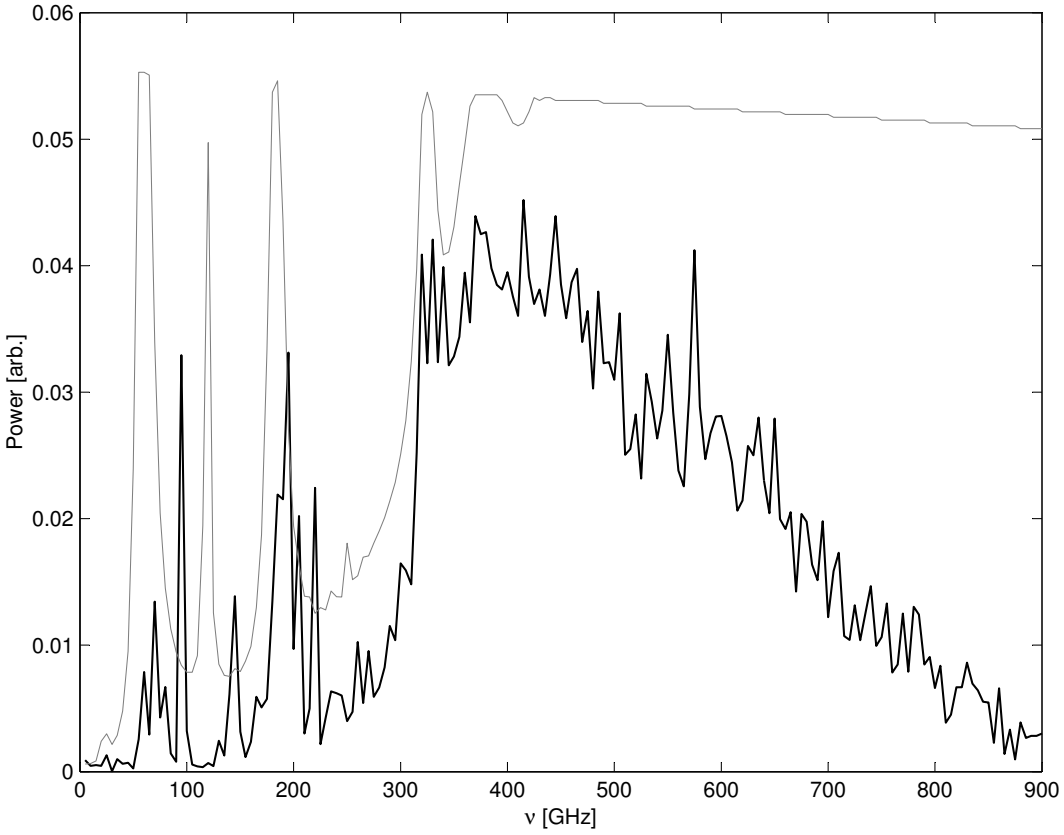

Figure 5.9: Power spectrum deconvolved with the fluorogold transmission characteristic (solid line). The original spectrum is also shown for comparison (solid-gray line).

remove the imaginary part from the computed interferogram, which results in a significant loss of signal strength in the computed final spectrum.

The computed power spectrum, shown in figure 5.8 (solid-line), is still convolved and includes the effect of the fluorogold filter. After deconvolving the fluorogold filter we obtain the power spectrum in figure 5.9 which has a significant variation with respect to the original power spectrum which is also shown for comparison. However, now it is clear that the shape of some spectral features are more defined than those present in the convolved spectrum.

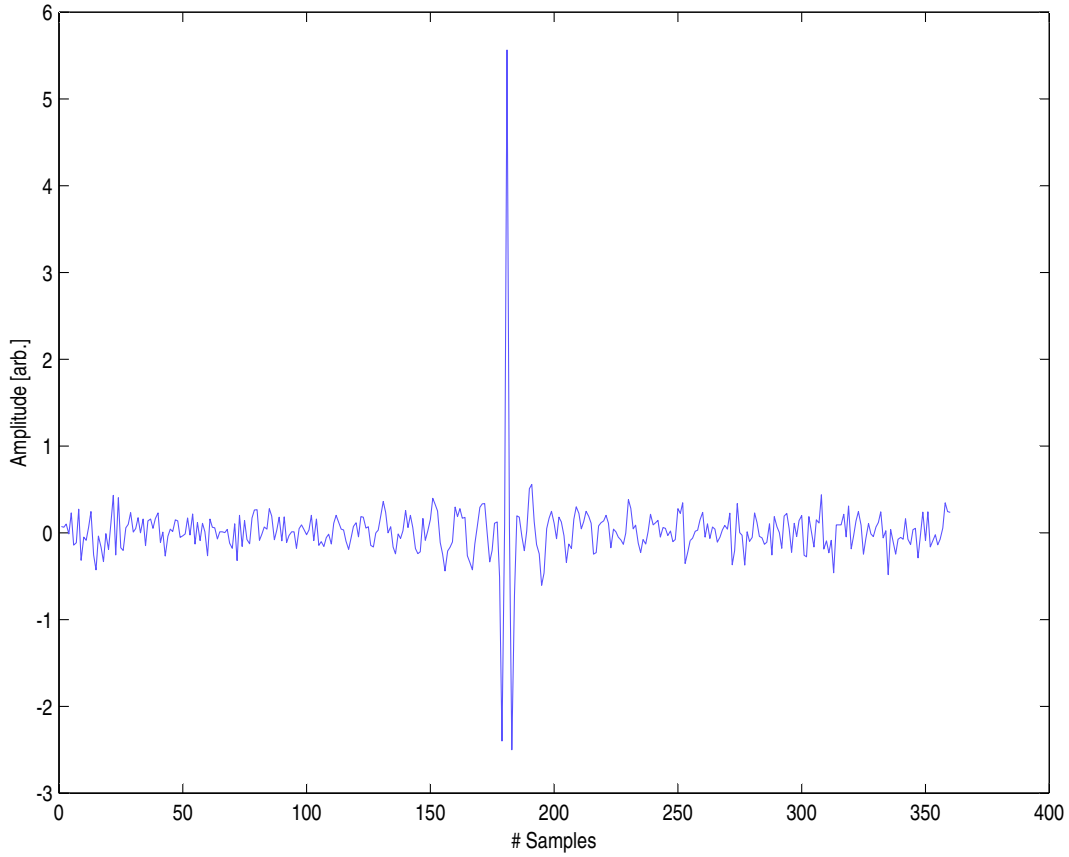

Figure 5.10: Simulated interferogram (i.e. atmosphere convolved with the fluorogold characteristic) plus normally distributed noise in oder to introduce asymmetries and reduce the S/N ratio.

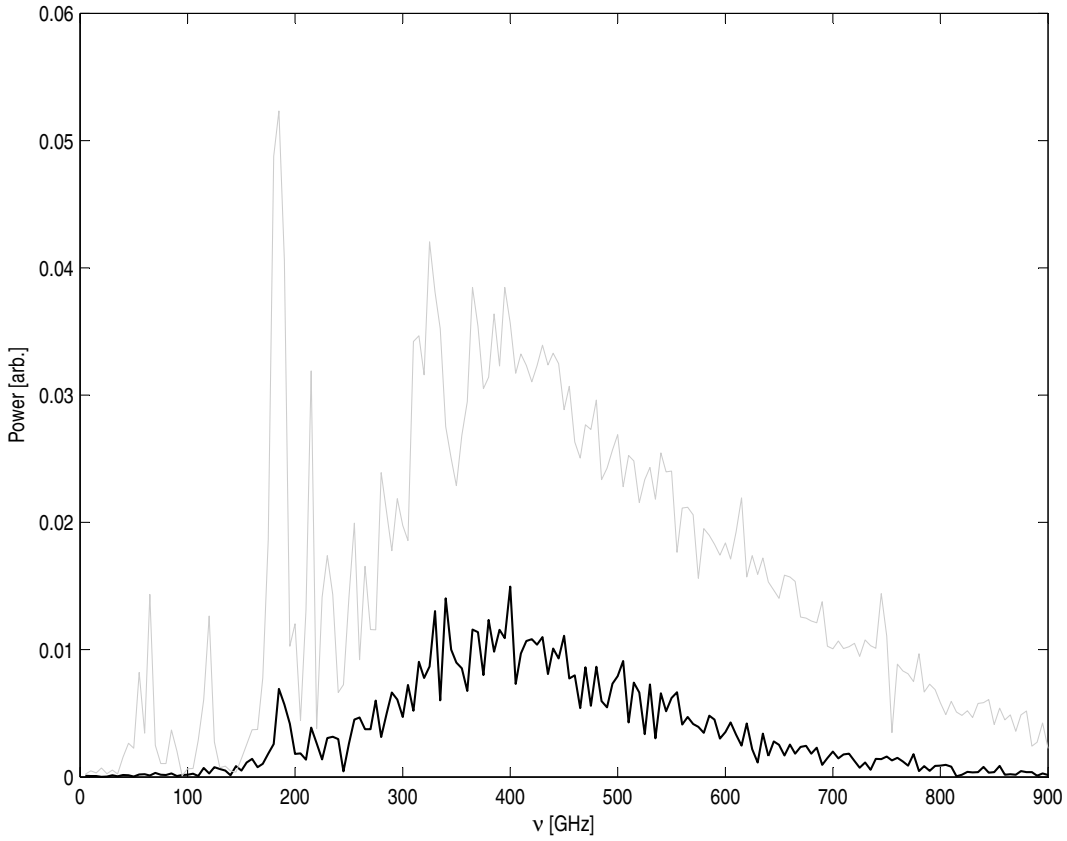

Figure 5.11: Recovered power spectrum from the noisy interferogram (i.e. Fig. 5.10 recovered (solid-line). The gray-line is the power spectrum which was obtained from the ATM code convolved with the fluorogold characteristic.

This simulated analysis, which does not take into account any noise, showed how the final spectrum is strongly affected by the blocking-IR filter. In order to have a more realistic case, we added noise to the computed interferogram to understand the effect of reducing the S/N ratio in the data. Figure 5.10 shows the interferogram with the addition of sufficient noise to introduce asymmetries in the data. Applying the same process to these data, that had been applied to the clean interferogram we obtain the convolved and the deconvolved noisy spectra shown in Fig 5.11 and 5.12.

The low S/N in the recorded interferogram produces a computed spectrum which is more affected by the noise at higher frequencies (i.e. $>$ 400 GHz) introducing a frequency shift of the spectral lines and also a significant amount of fake spectral features. From this analysis we have demonstrated that in order to recover a clean spectrum we require high sensitivity (i.e with noise level $\sim$1/100 of the bright central fringe) in order to be sensitive to the small variations present at the extremes of the interferogram that contribute to the detailed structure of the final computed spectrum.

5.5 Experimental setup

Figure 5.13 shows the experimental setup used for the first test of the FTS-MPI. The interferometer was mounted on an optical bench completely enclosed with an acrylic box. The box was purged with nitrogen gas in order to reduce the relative humidity inside the box to $\sim$5%, and hence avoiding high absorption of the input radiation. The cryogenic detection system was initially operated at a temperature of 4.2 K. The interferometer was configured to use two input ports. The source was a room temperature absorber (i.e. Eccosorb) placed at the input port 1, modulated against a cold source load (i.e. liquid nitrogen). The output port 2 was terminated using a piece of Eccosorb at a room temperature.

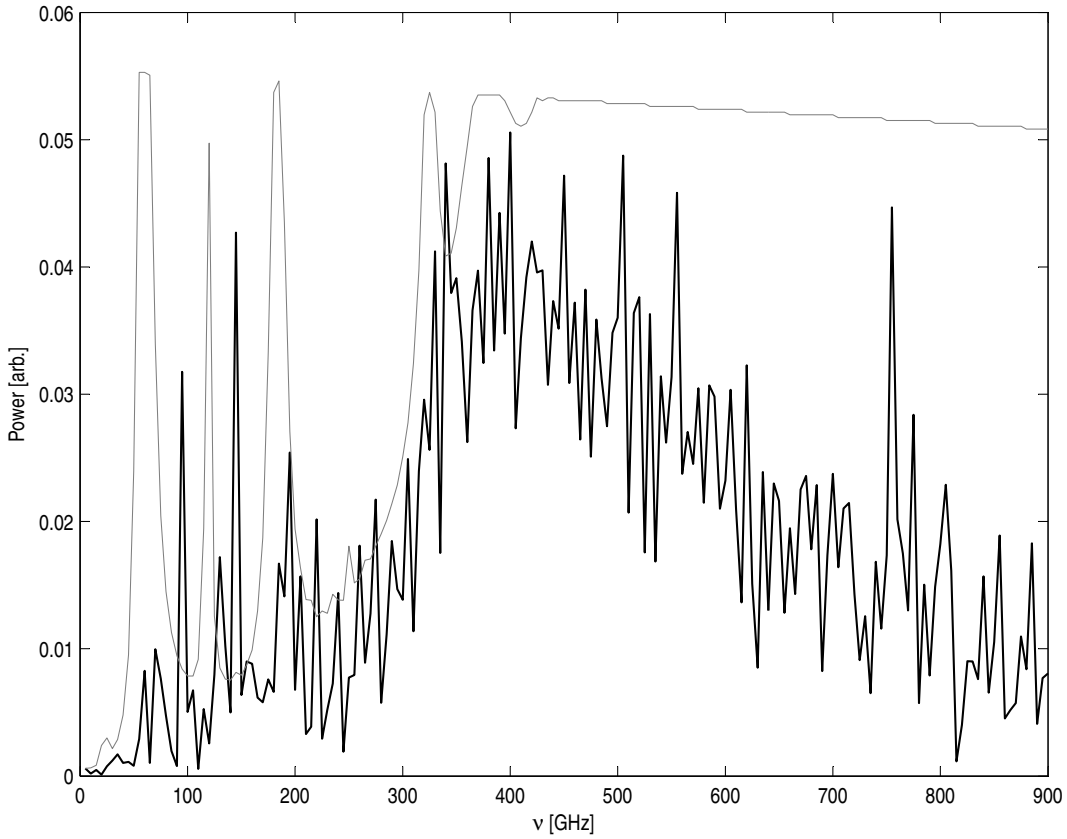

Figure 5.12: Power spectrum from noisy interferogram deconvolved with the fluorogold transmission characteristic (solid-line). The original atmospheric power spectrum shown for comparison (gray-line).

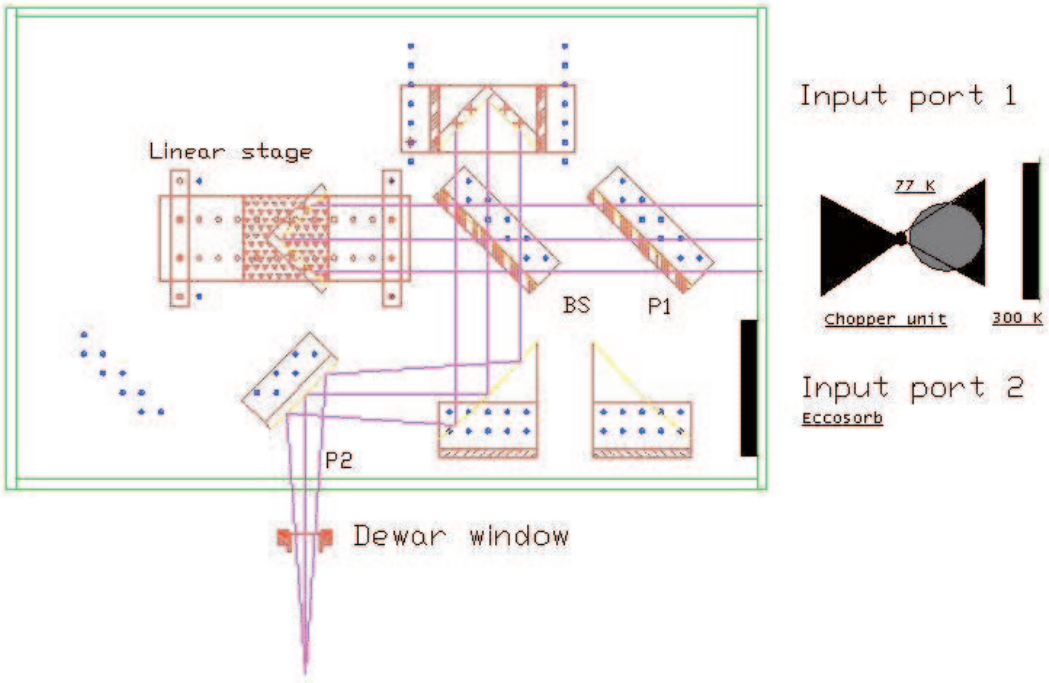

Figure 5.13: Schematic setup of the first experiment with FTS-MPI. P1 is the input polarizer; BS is a polarizer used as beam-splitter; P2 is the output polarizer.

5.5.1 Chopper Stability

Before describing the results obtained during the initial tests with this setup, it is necessary to present some effects of the frequency stability for the chopper. In

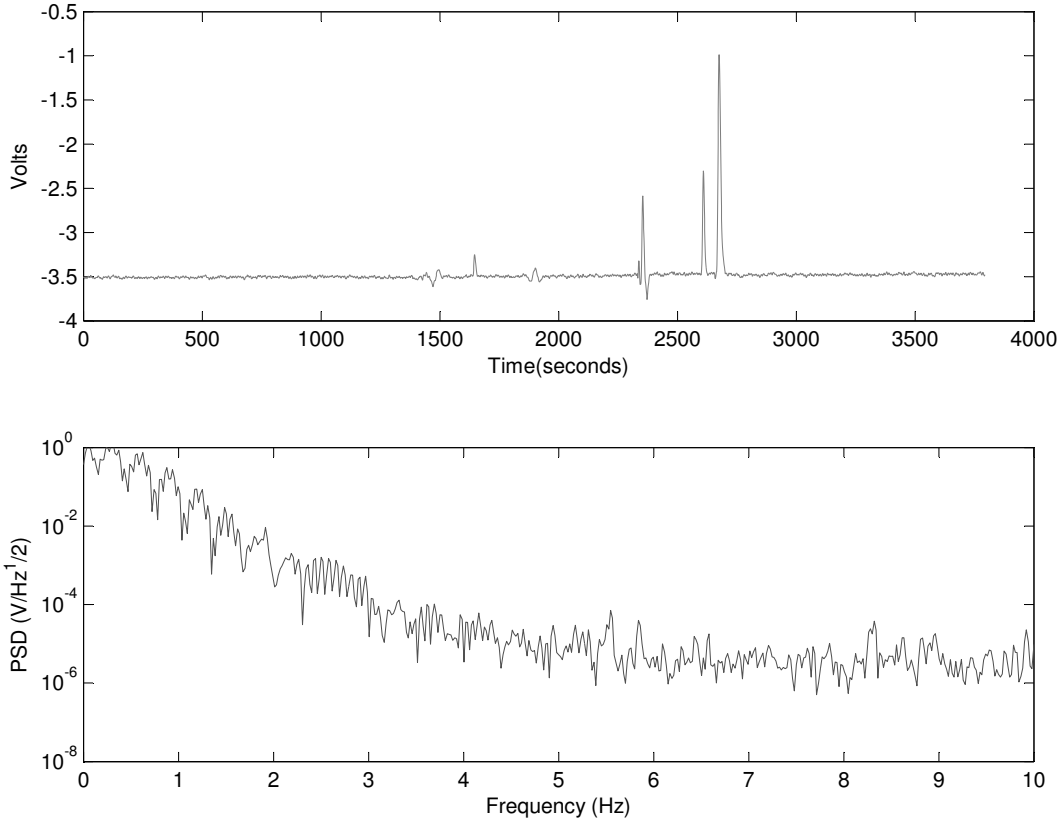

Figure 5.14: Top panel: Interferogram record which shows large spikes due to an unlocked signal events. These events are related to a bad reference signal generation. Bottom panel shows the PDS of the interferogram record.

order to have a better sensitivity and noise-rejection of the incoming signal, we use a phase-sensitive device (PSD) amplifier. This device demodulates the signal that only matches the reference frequency. Hence any other signal, at different frequencies will not be amplified.

In the experiment, the rotating chopper produces a modulated signal at the spinning frequency of ∼1 - 8 Hz. A reference frequency should therefore be measured directly from the chopper. We measure this reference by using a slot photosensor mounted so that the chopper blades produce a signal with the frequency of the spinning motion. This reference frequency is then feed back to the PSD-amplifier and it is used to demodulate the signal. The reference signal should be stable enough to allow the PSD-amplifier to respond to the modulated signal. When the reference signal is not "locked", i.e. moves outside the ±0.1 % window, then an incorrect signal is delivered by the amplifier. This condition contributes significant noise to the recorded signal. Figures 5.14 shows an interferogram that is highly affected by reference signal variations. We were seriously affected in this experimental setup by the chopper instability that produces a voltage fluctuation in the recorded interferogram will then produce a large DC level on the final computed spectrum. The power density spectrum (PDS) of the spiked interferogram shows a large electronic power contribution from the frequencies <4 Hz and therefore some power will leak into the interferogram signal that is modulated at 3.8 Hz. In order to solve this instability from the chopping system we decided to change the scheme of modulation, as explained in the section 5.6.

5.5.2 Continuous-scan mode results

For this initial test we employed a continuous-scan mode with a constant velocity of 40 μm/s. The interferogram was acquired at a sample-rate of 7 Hz which is twice the modulation frequency. Figure 5.15 shows a single recorded interferogram that has an unexpected voltage drift. It is also clear that a non-symmetric recording is obtained. The voltage-drift present in the recording is most likely due to the temperature variation of the chopper blades, since during the experiment the liquid nitrogen bucket was placed very close (within ∼5 cm) to the chopper.

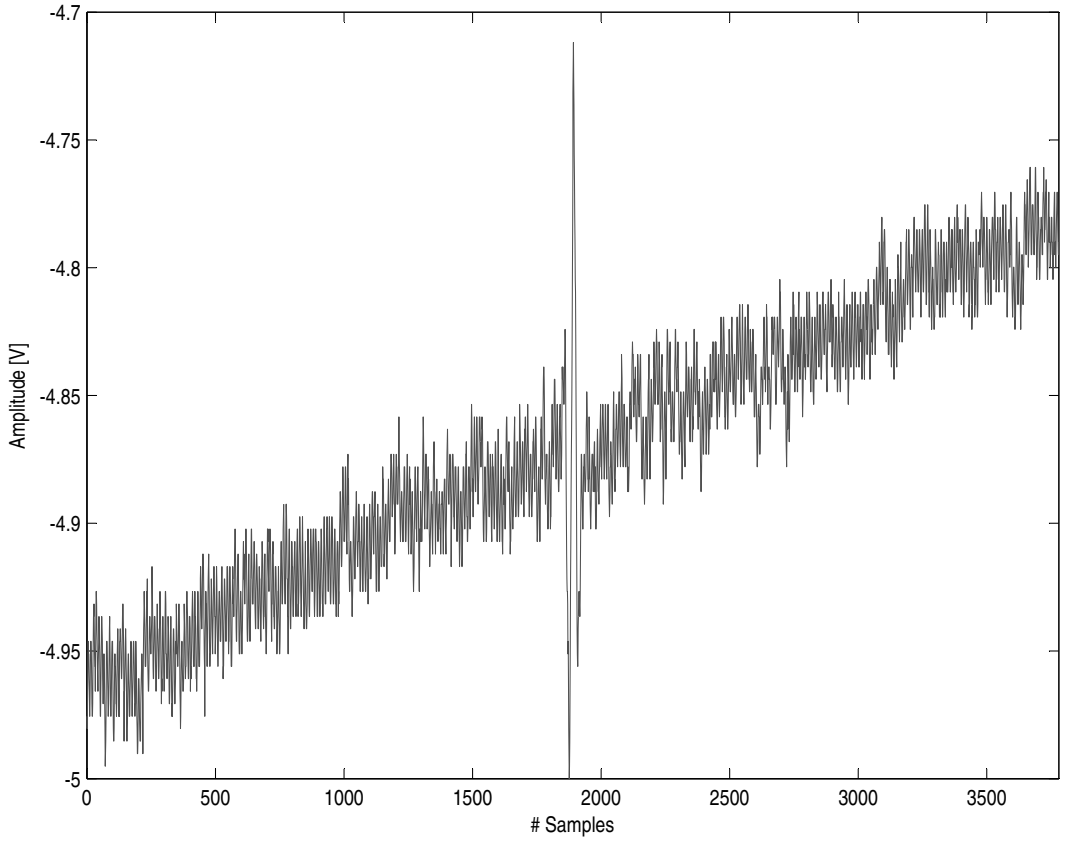

Figure 5.15: Interferogram record showing the voltage drift present in all the interferograms recorded in the original setup of the FTS-MPI.

This reduced the temperature of the chopper blades and hence a change in the power emitted towards the interferometer.

We also observe a low S/N ratio at the position of the secondary lobes of the interferogram, which will have a negative impact on the final computed spectrum, as explained in section 5.4. In order to improve this situation we co-added multiple interferograms which improve the S/N ratio of the secondary lobes. Figure 5.16 shows the details around of the central bright fringe of a combined set of 4 interferograms (top-right panel) that demonstrate a great amount of constant features which, by means of co-addition, can improve the interferogram.

In order to compute the spectrum we first remove the voltage drift and the voltage DC level of each interferogram which has the effect of eliminating the unwanted large DC component in the final computed spectrum. We performed the voltage-drift correction by taking equally-spaced points (i.e. 20 samples) along the entire interferogram, to which we applied a linear fit. This simultaneously removes the voltage drift as well as the DC level. The bottom-left panel in Figure 5.16 shows a fully processed interferogram (averaged from 4 records and DC corrected) which improves the S/N ratio around the central bright fringe, although there is still noise at both ends of the interferograms as well as significants drifts in the signal on scales of 200 - 300 samples (i.e. $\sim$1 to 1.5 mm of movement along the track). This does not implies that the screw-thread is not constant because, the effect is not present in the step-integrate scan mode. Figure 5.17 shows a set of averaged interferograms obtained during the continuous-scan mode tests. The first, the second and third row are records looking at the sky and the fourth row shows a record looking at a room temperature absorber. Each one is the average of 5 interferograms recorded in period of 5 minutes. Each averaged interferogram is then Fourier-transformed in order to compute its spectrum. Figure 5.17 also shows the respective spectrum without phase correction and frequency calibration. From the graphs we see a constant shape that is the result of the instrument profile plus the transmission profile introduced by the flourogold

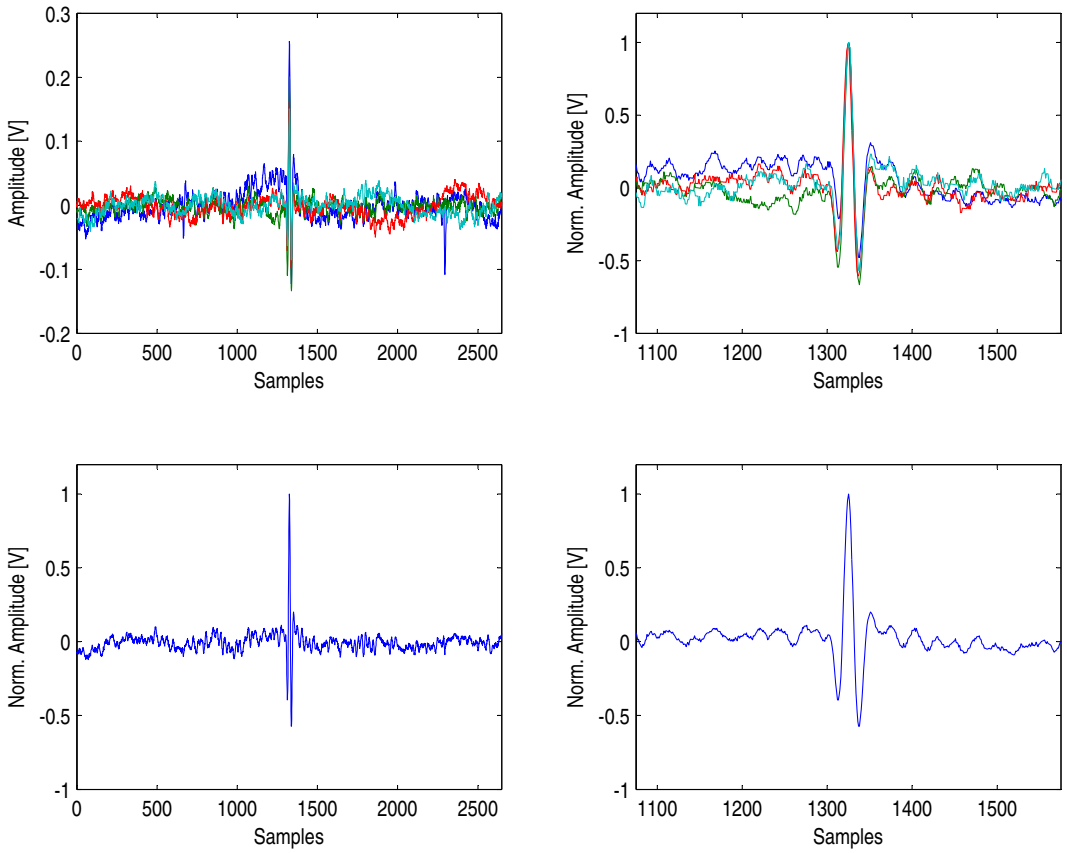

Figure 5.16: Various interferograms used to improve the S/N ratio. The top-left panel shows the set of 4 interferograms used to calculate the average of those interferograms obtained with the original experimental setup shown in Figure 5.13. Top-right panel shows a detail of the central region of the individual interferograms. Bottom-left panel is the average of the 4 interferograms and bottom-right is a detailed view of the central region of the average interferogram.

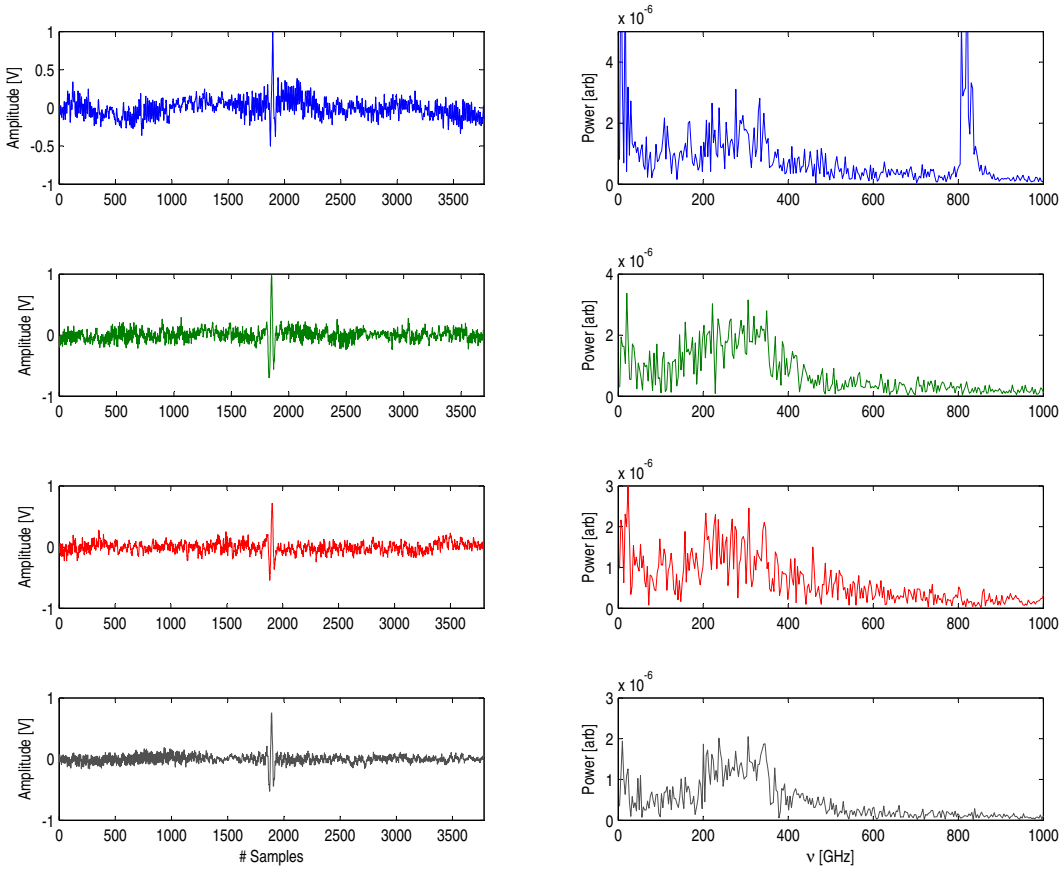

Figure 5.17: Computed spectra obtained after inverse Fourier transforming the average from 5 interferograms set which represent different hours during day in which the experiment was conducted (from the morning to evening).

filter as shown in the simulated spectrum from section 5.4 (see Fig. 5.11).

5.6 Modified experimental setup

Until this point we have explained the preliminary results of the first experimental setup for the FTS-MPI system. Based on that experience we decided to modify some aspects of the system to improve the noise introduced by the chopper in-

stability, which we considered one of the most important sources of noise in the final recorded interferogram. Figure 5.13 shows the original configuration used in previous experiments. For this new test we modified the SRS540 optical chopper in order to place the blades at output port of the interferometer. This modulates the combined signal from both input ports (see Fig. 5.18). We used the same electronic control of the SRS540 to produce a stable reference frequency for the PSD amplifier.

In this setup the two input ports are completely available to be used with any source. However we keep input port 1 as the input for the signal under study. Input port 2 is used as a reference port, and the reference source for this port is liquid nitrogen or a room temperature Eccosorb. In addition we built an extension to install a flat mirror at 45 degrees and fold the input beam toward the sky. This last modification allowed us to perform a measurement of the sky and verify the capabilities of the system by measuring the power spectrum of the sky.

5.7 Data sampling: step-integrate mode

All the data recorded during this modified experiment were acquired using the step-integrate mode. We observed that this sampling mode allowed us to improve most significantly the S/N ratio of the recorded interferogram, because this is increased as $\sqrt{N}$ where N is the number of samples at a given path difference δ. Figure 5.19 shows an example of one recorded interferogram, which presents an improved symmetry compared to those records obtained using the continuous-scan mode with the previous configuration. The interferometer is illuminated with a power signal of $\sim$30 nW. Most of the power in the interferogram lies in the central fringe, the rest of the power is distributed into the secondary lobes. Our detection system in practice is able to resolve power contained in the central fringe, but in the case of resolving the power contained at the extremes, which is

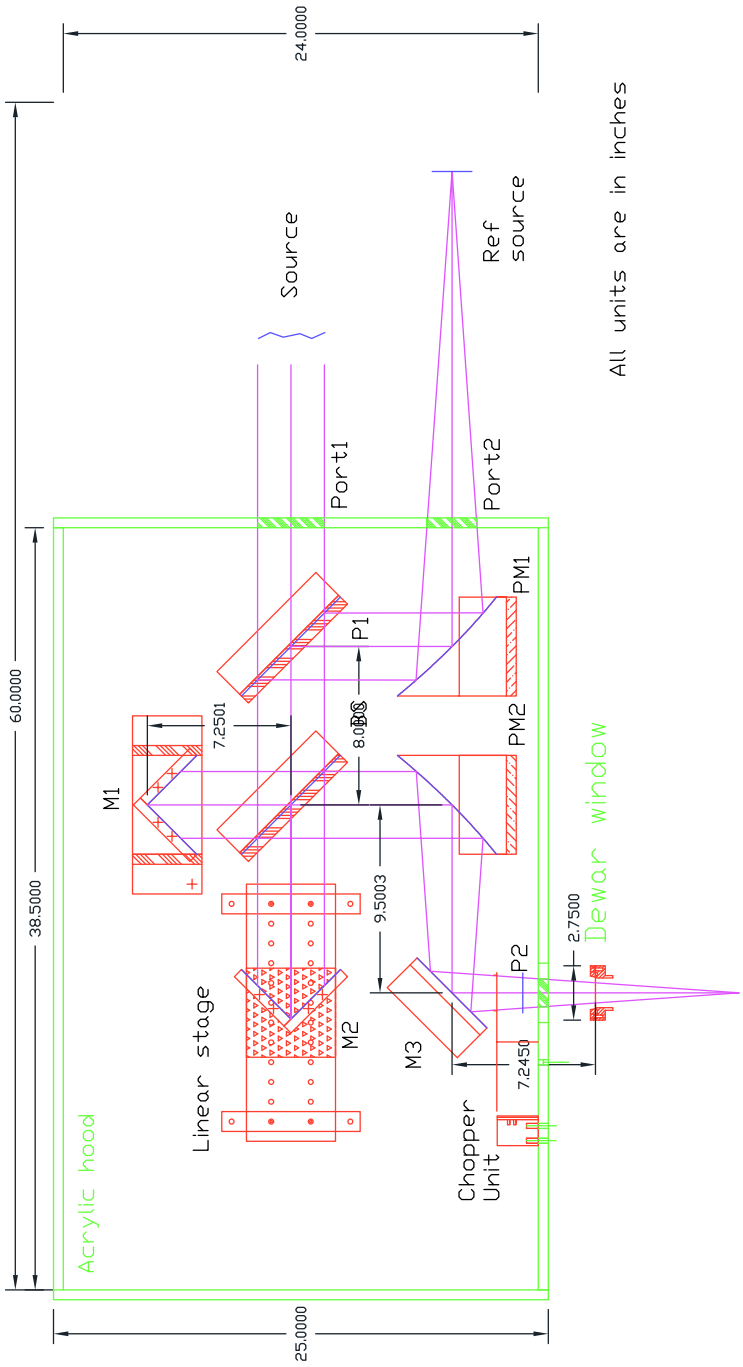

Figure 5.18: Current configuration of the FTS-MPI.

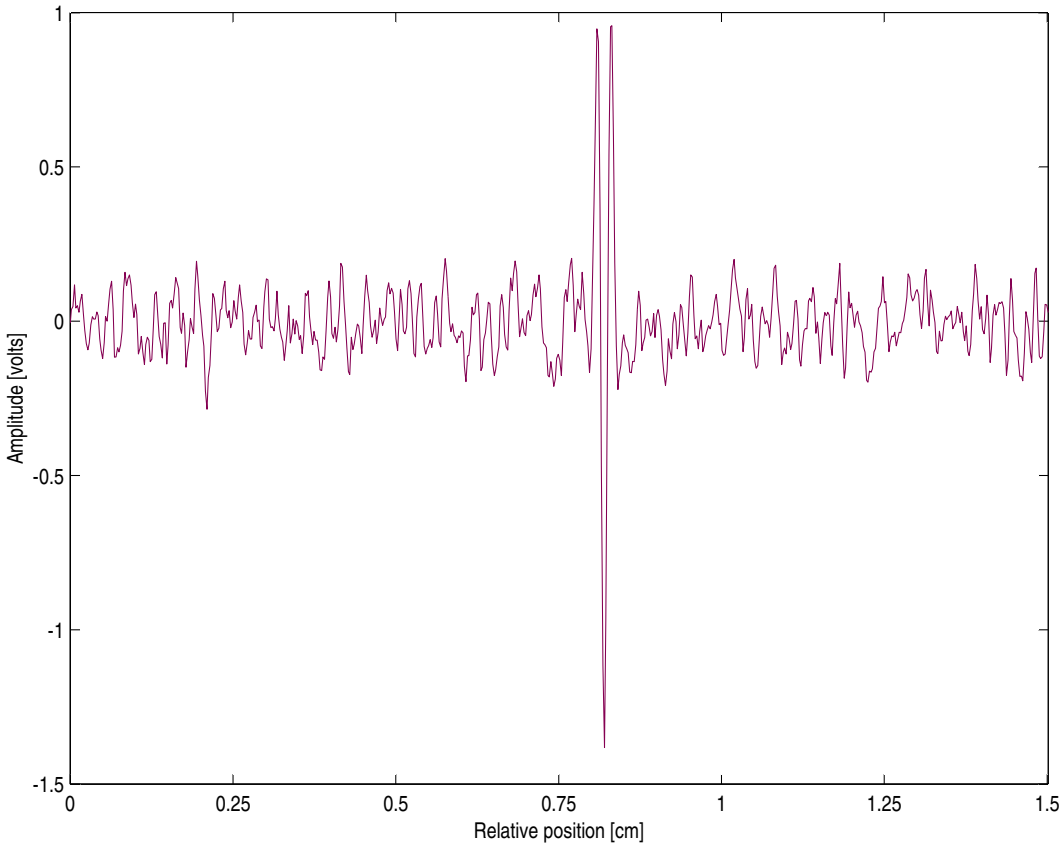

Figure 5.19: Interferogram recorded using step-integrate mode, looking the sky.

about to 3×10^4 smaller than the central fringe, we expect to be at the limit of the detection system. The expected power contained at the extremes is ∼1 pW. The NEP, in terms of a required S/N∼4, should then be $\sim 1 \times 10^{-13}$ W/Hz$^{1/2}$. The measured NEP of our detection system at 3.9 K is $\sim 1.5 \times 10^{-14}$ W/Hz$^{1/2}$ which in practice should provide ∼70 times the required S/N. Figure 5.20 shows the signal to noise ratio of each sample as a function of its position in a single interferogram record. The faintest ends show that the S/N ratio is below the required value to resolve completely the interferogram. This implies the existence of a extra source of noise which has not yet been identified. The mean S/N ratio is ∼ .06

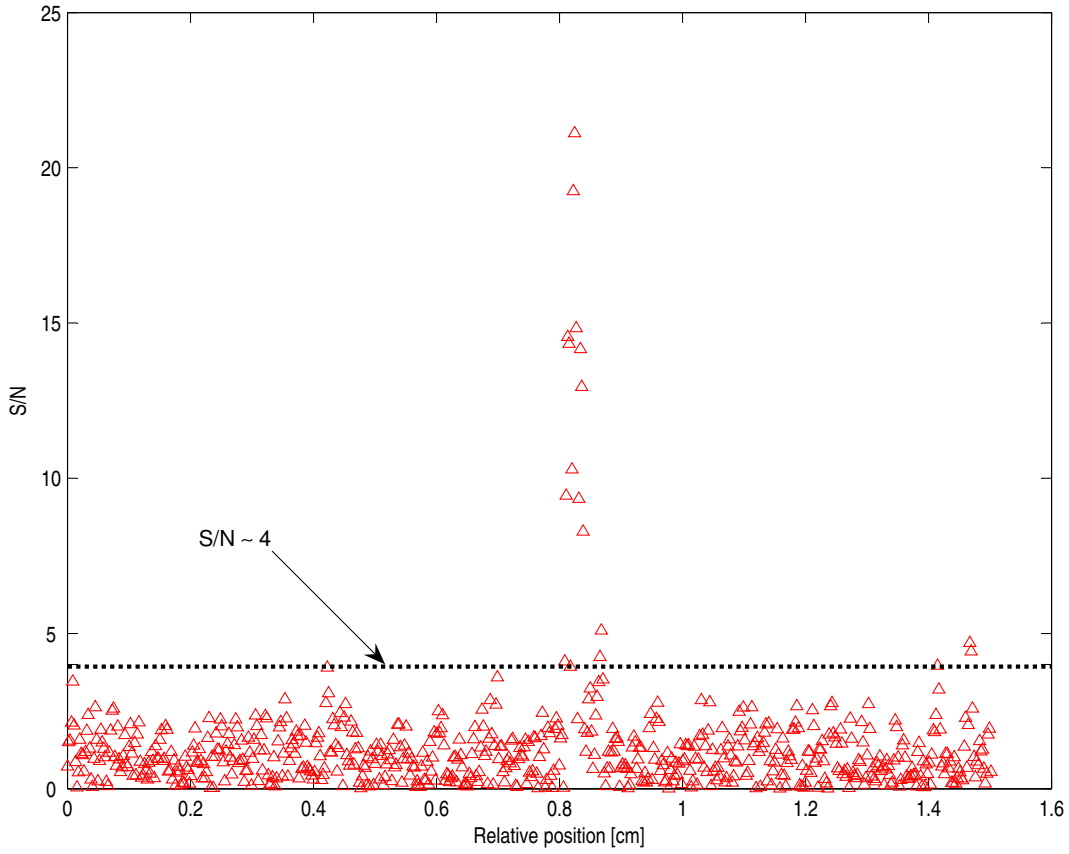

Figure 5.20: Signal to noise ratio of the interferogram. The dotted line shows the required level of the S/N ratio.

which is 66 times smaller than the required S/N ratio for the extremes of the interferogram signal.

5.8 Zero path difference variability

Another important result from the modified experiment, with the step-integrate mode, is the variability of the zero-path difference position along the record, which of course is not due to the actual setup. This effect becomes more evident using

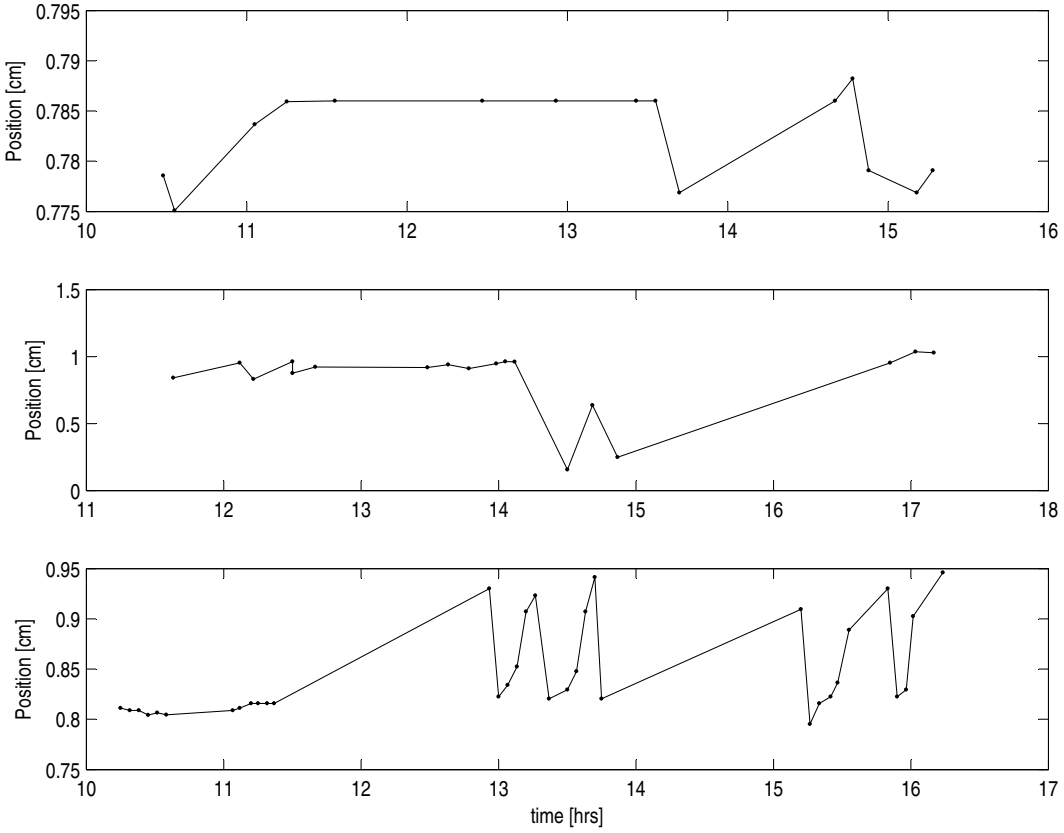

Figure 5.21: Position vs. time of the central bright fringe. Top-panel data obtained using liquid nitrogen as a source. Middle-panel data obtained looking at the sky. Bottom-panel data obtained using a variable blackbody source.

the step-integrate mode that allows us to record the relative position for each sample. The importance of this behavior is due to the fact that it affects the final spectral resolution of the computed spectra by reducing the effective length of the measured interferogram. Figure 5.21 shows the effect of the variability under the different loadings conditions (i.e. looking the sky, liquid nitrogen and a blackbody source with a variable temperatures, 243 - 423 K) with which the interferograms were taken. The points represent the position of the bright fringe plotted against the time at which the interferogram was recorded. The data shown in the top

panel corresponds to interferograms recorded using a liquid nitrogen as a source, during a ∼5 h period of time. The same period of time is shown in the middle panel, in which the source is now the sky. The position of the bright fringe is more variable than in the previous configuration and 5 times broader. Additionally large variations were present at the end of the measurements. Finally the bottom panel shows data taken using a blackbody calibration source with large position variations during the experiment. We assume that this variability is due mainly to turbulence in the air close to the input ports. This effect of interferogram-motion is compared with the observed effect in a laser-illuminated Michelson interferometer, in which air turbulence in any of the two interferometer arms or at the input, produces vibrations in the interferogram image. We use liquid nitrogen as the reference source at input port 2. Because the source is outside the acrylic box, it will produce local air turbulence due to the convection and the mixing of hot air and cold nitrogen gas around the container. Also variations in the power emitted by the source are introduced due to the ice build-up which changes the transmission properties of the container. This interferogram-motion effect reduces the effective length of the interferogram and consequently it will reduce the spectral resolution; furthermore variations in shorter times scales will produce a noisy interferogram and therefore a low S/N spectrum. The above should be taken into account in order to improve the performance of the FTS-MPI. All the modifications to improve the system will have to be done as part of the future work.

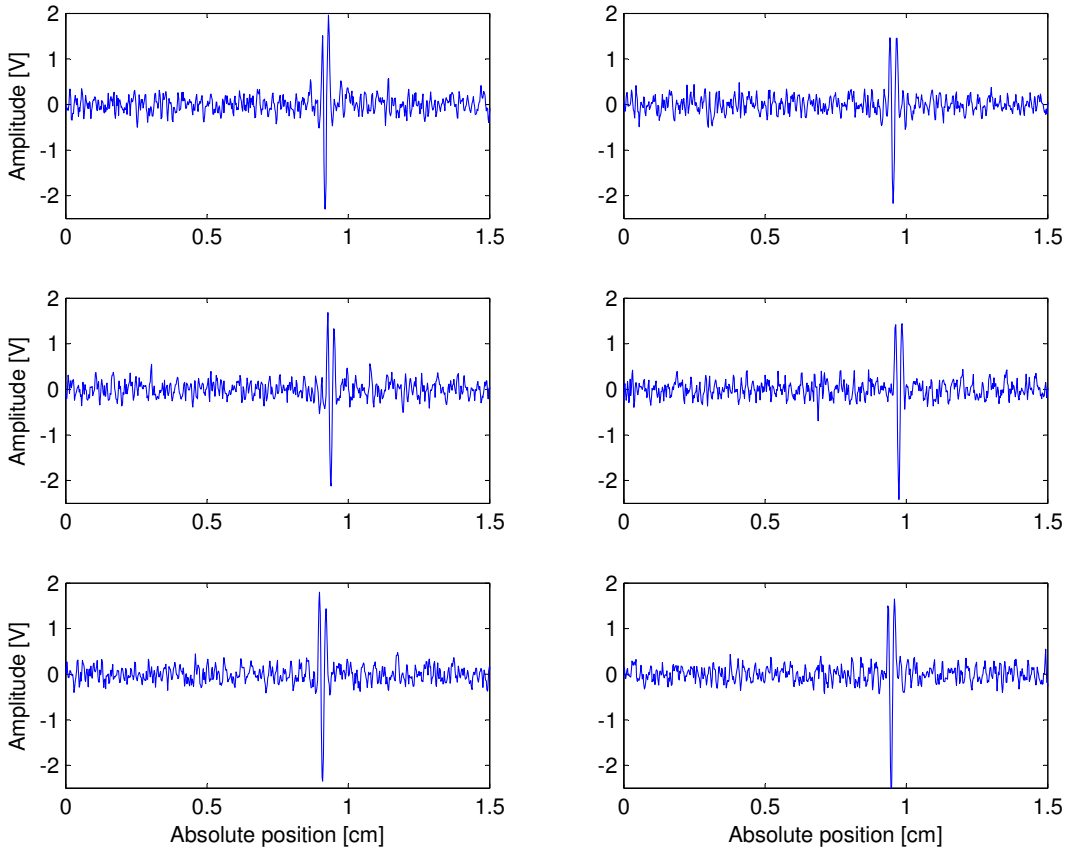

Figure 5.22: Set of measured interferograms obtained in the last run experiment. The FTS-MPI system was illuminated with the sky power signal and referenced with liquid nitrogen sources.

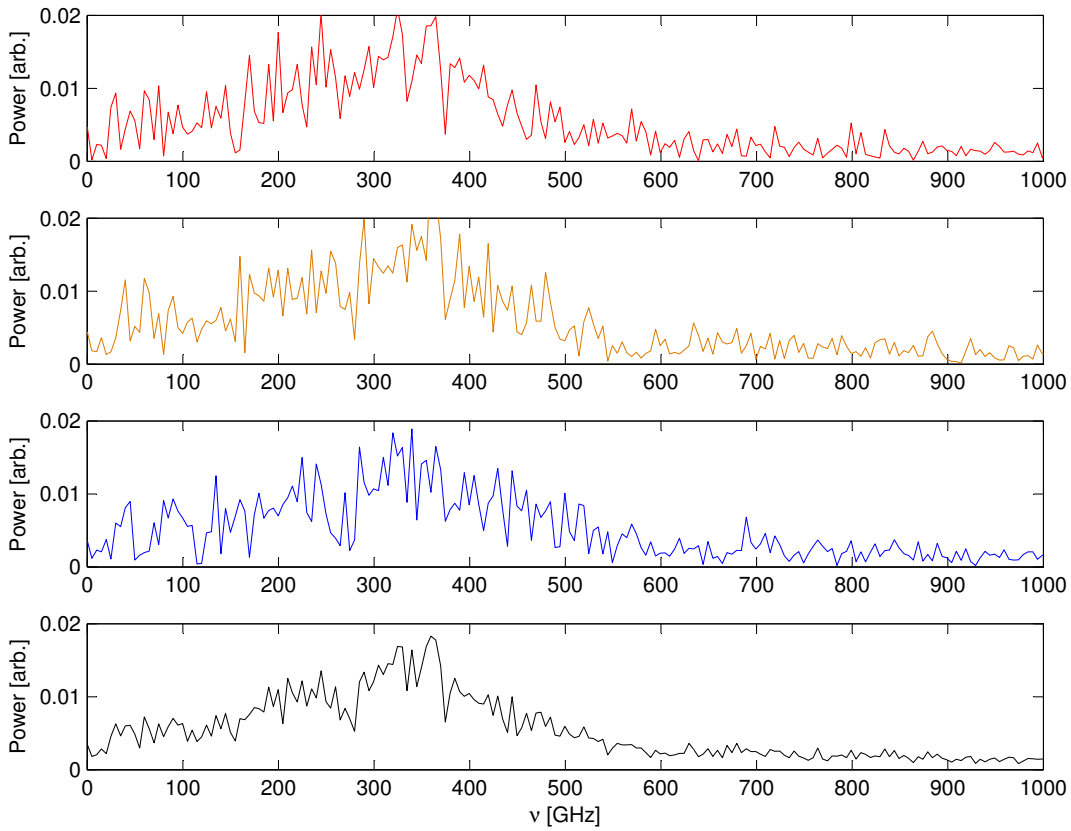

Figure 5.23: Computed power spectra from the measured interferograms shown in Figure 5.22. From the top, the first three panels show the computed spectra from single interferogram record, the last panel shows the average of 5 spectra.

5.9 Computed spectra

In section 5.4 we simulated synthetic spectra of the sky emission from which we obtained information of the energy distribution as a function of the spatial frequency (i.e. optical path differences). From these simulations we quantified the expected S/N ratio for the interferogram, and therefore the quality of the computed spectrum. Based on the discussion in section 5.7, the computed spectra from the interferograms, with the observed characteristics, result in low S/N spectra. Figure 5.22 shows several examples of single measured interferograms during the last experimental run in which the FTS-MPI was illuminated with the sky power signal through the input port 1, and the reference source through the input port 2 (i.e. liquid nitrogen). All the interferograms show constant features through the observing period which demonstrate the repetitively of the measurements. The above is an advantage because no systematic features will be removed by averaging process. Due to the Fourier transform, which is a linear transformation, the result will be the same if we transform the average interferogram or we average the computed spectra. We averaged the computed spectra because we avoid to align the central fringe to a fix position in order to average all the interferograms. Figure 5.23 shows the computed spectra by taking the inverse Fourier transform of the interferograms shown in Figure 5.22. The amplitudes of the spectra are shown in arbitrary units, because no calibration process has been applied to the data due to lack of a well known reference spectrum obtained from the FTS-MPI. The reference spectrum is used to remove the instrumental profile and to calibrate the power amplitude. The above is an important issue that must be implemented to improve the experimental analysis shown up to here.

The spectra show a constant shape for different periods of time during day demonstrating the instrumental profile. Also the computed spectra from the measurements are similar, and these are compared to those computed from simulations. The bottom panel from Figure 5.23 is the average spectrum from 5

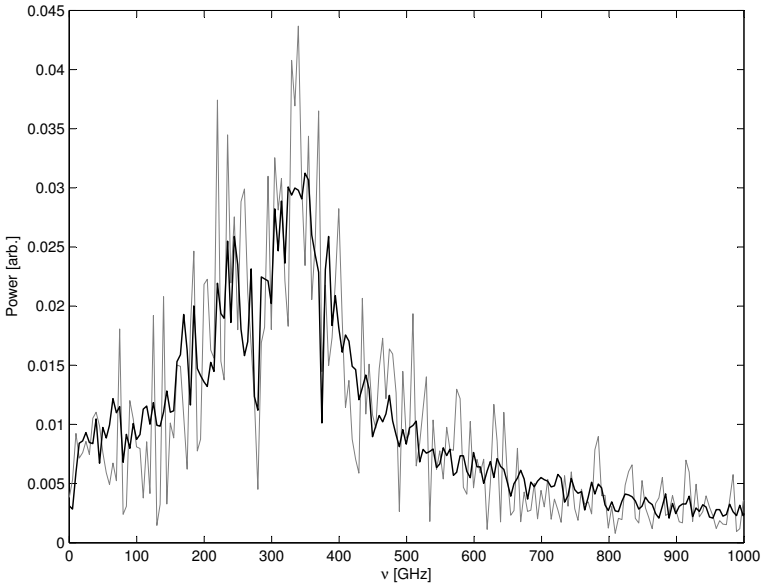

Figure 5.24: The solid dark line is the computed spectrum from 5 spectra average. The solid gray line shows a single computed spectrum which is also for comparison.

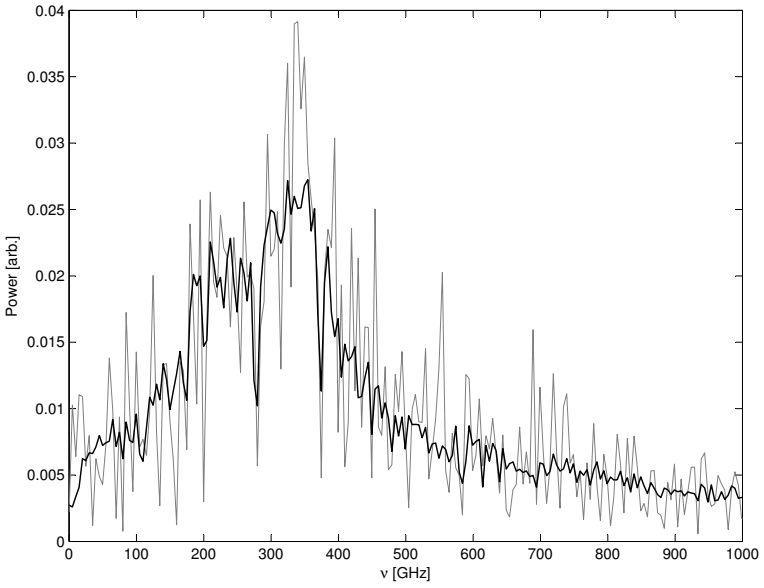

Figure 5.25: Similar to the figure 5.24 the solid dark line is the computed spectrum from 10 spectra average process.

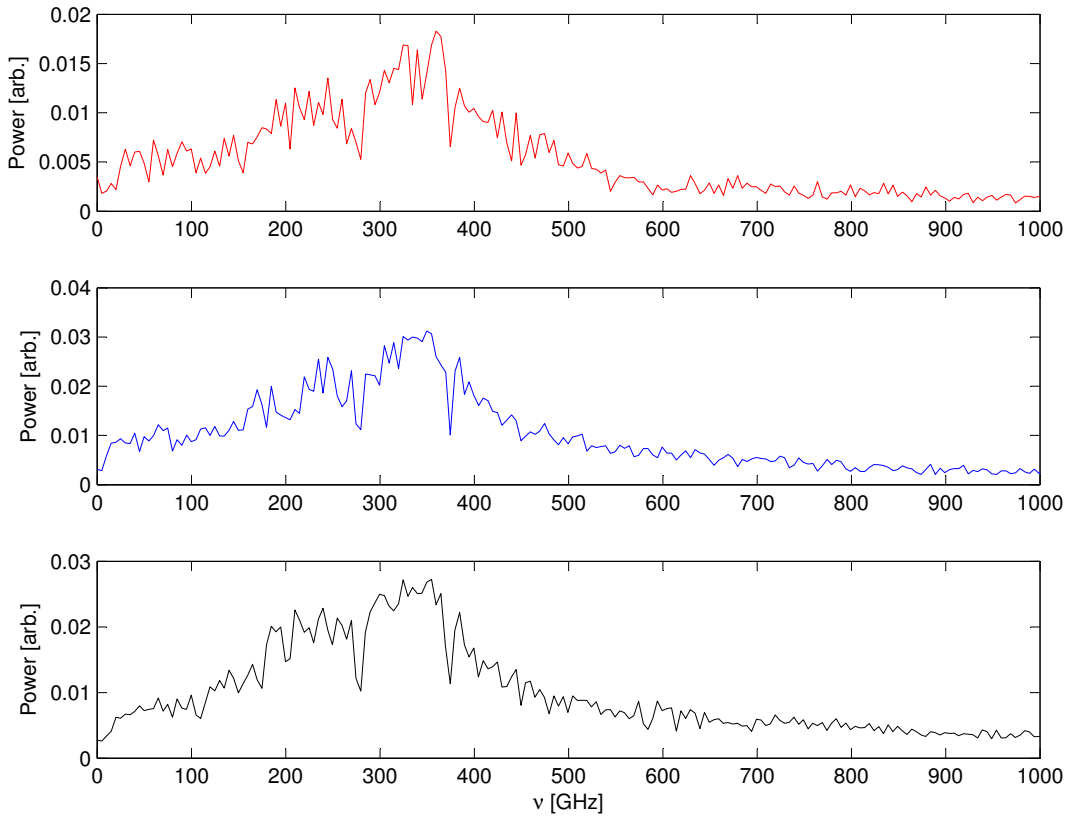

Figure 5.26: Average spectra for different stages of the experiment during the day. The top panel is the average of 10 spectrum from measured interferograms recorded during the morning. The middle panel is the average of 10 spectrum for noon and the bottom panel is the average spectrum for the evening.

computed spectra obtained from measurements in period of 15 minutes all. We see clearly that the averaging smooths the shape of the spectrum and eliminates fake spectral features. We show in Figure 5.24 a single computed spectrum and the average spectrum for comparison. Also, in Figure 5.25 the average spectrum from 10 computed spectra are shown to illustrate that heavy averaging improves the S/N ratio of the spectrum as expected. Figure 5.26 shows the average spectra for different stages of the experiment during the day. As a result we see, after the

averaging process, that three spectral lines which are always present in all computed spectra. We identified one spectral line to be the 183 GHz water-vapour line which is indicated in figure 5.27. The emission water-vapor line shape is shown for comparison in order to establish the validity of the detection. Another line lies close to the strong 385 GHz water-line blend which provides high opacity in the atmospheric spectrum. In the same way we show the emission line at this frequency to illustrate the identification. A third line is indicated by the emission line at 325 GHz. There is also a non-identified line at ∼280 GHz and therefore we believe that is a possible effect of the fluorogold filter used in the system. Observing all these lines and comparing with the spectral characteristic of the fluorogold filter we see an overall spectral shape introduced by the filtering.

Unfortunately it is clear that from a single interferogram record it is not possible to obtain a high quality spectrum because we are totally affected by the noise in the experimental system, as was shown in the previous analysis in section 5.7. Therefore we conclude that a possible external source of noise introduces variability into the interference pattern, reducing the computed quality of the final spectrum. However, as we observed from figure 5.27, the FTS-MPI system is able to measure the power spectrum from the sky over a bandwidth of ∼100 -1000 GHz. We have identified a spectral region that corresponds to the blending of lines at 385 GHz. The detection of these spectral lines under the conditions of low S/N and without proper scheme of calibration, indicates that we have developed an experimental set-up that will provide a useful site characterization instrument for the LMT project, provided we are able to upgrade our cryogenic capability to a colder and more sensitive 300 mK system. Our future work will therefore focus on improving the actual system, as well as the opportunity to apply the skills learned during this work to propose the design an spectroscopic system for the LMT.

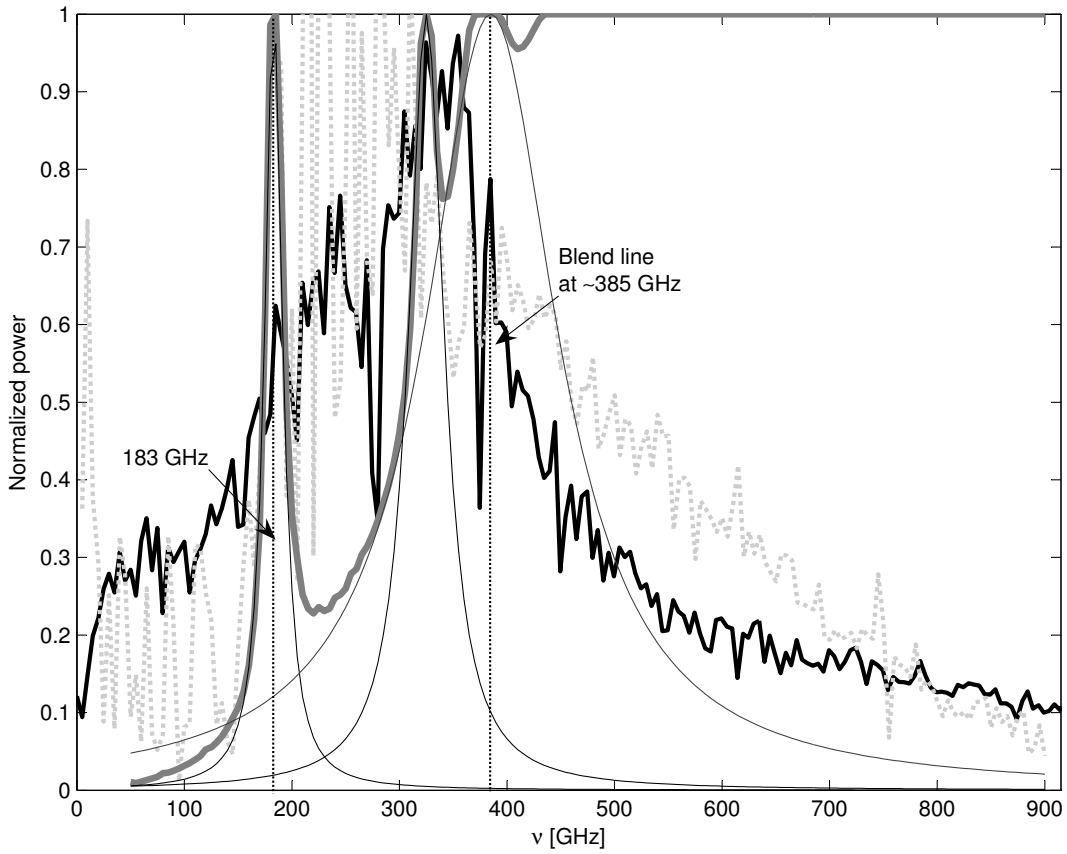

Figure 5.27: Average spectrum from full set of interferograms obtained in the experimental run observing the sky (solid-dark line). The 183 GHz water-vapour line and 380, 382, 386 390 and 391 GHz water-vapour blend lines. The vertical-dotted lines show the position of the central frequency of the measured lines.

Chapter 6

Conclusions and Future Work

The goal of the present work was to create the facilities to develop the basic cryogenic instrumentation for sub-mm/mm wavelengths and to develop basic instruments based on bolometric detectors to work in the sub-mm/mm wavelength regime.

Since this kind of technology has not previously been developed in México, it was necessary to first learn the experimental skills in this area. Thus first I started my training with other international groups with great experience in system design and integration of cryogenic instrumentation. In 2001 I worked for almost one year at the University of Pennsylvania (UPenn) with the Prof. Mark Devlin's group. During this period I was learning the basic skills in cryogenic systems ($\sim$ 4.2 to 300 mK), vacuum techniques, bolometer characterization, low-noise read-out electronics as well as optical materials for optical-FIR blocking filters, and basic skills in mechanical design for cryogenic systems. In 2002 we spent two months working on a Far-Infrared Fourier Transform Spectrometer system. I worked on the optical alignment of the FTS and debugging the data acquisition and control software for the system.

The experience obtained during the period 2001-2002, allowed us to begin establishing the millimetric-instrumentation laboratory at INAOE in 2002. With the initial MI-Lab facilities I fully characterized a composite bolometer to temperatures down to ∼1.5 K. The bolometer is the critical component of our millimetric camera, used in the FTS-MPI, which was designed as part of the Total Power Sky-Monitor. The composite bolometer was designed with an NTD:Ge thermistor from Haller-Beeman Inc. In order to improve the thermal conductance for operational temperature of ∼1.8 K, we designed a bolometer that used 12 μm diameter, 5 mm length NbTi leads. As result of this characterization we found that the thermal conductance of the bolometer using these leads at 1.8 K is $\sim 5.5 \times 10^{-8}$ W/K, a larger value than the prediction from the design i.e. 3×10^{-9} W/K. This resulted in a less sensitive device and a slower time response. However this experimental result contributes to the knowledge of the thermal properties of the NbTi leads at temperatures in the range of 1.5 - 3.9 K. I still expected however that the sensor would be sensitive enough to be used as part of the FTS-MPI system, since the power-loading conditions are higher than those conditions for the Total Power Sky-Monitor.

I have presented the development and the design of a Fourier Transform Spectrometer of the Martin Puplett type to work at sub-mm/mm wavelengths. In order to couple the cryogenic camera with the interferometer optics, I modified the cold optics, which allowed us to eliminate temperature fluctuations present in early configurations. The coupling was obtained by designing a new aluminum feed-horn with a f/4.8 focal ratio. The feed-horn and all the interferometer optics were made at INAOE. This is an important fact to report because it demonstrates our capabilities to produce complex optics for future sub-mm/mm instruments.

I have shown an analysis of the impact that the IR-blocking filters have on the instrument response, as well as the techniques used to compute the power spectrum from the recorded interferogram. An important conclusion from this analysis is the relation between the S/N ratio and the final computed spectrum.

A high S/N ratio in the secondary lobes will naturally produce a computed spectrum with higher fidelity. The step-integrate and the continuous sampling were tested in order to determine the most suitable technique for sampling of the interferogram. Due to the simplicity of the step-integrate technique I decided to program the acquisition and control software based on this observing mode. The data acquisition and control software was developed in LabView, which also provides the interface to the servo-motor microprocessor unit, to control the moving mirror.

The FTS-MPI has been built and tested in the laboratory. The Martin-Puplett optical configuration used for the FTS allows for a simple design and fast implementation with our limited financial resources. The FTS-MPI is the first system to which we applied our detection bolometric system. The sensitivity of the sensor is improved by cooling down up to 1.49 K. This reduction in temperature however sacrifices the hold time of the dewar from $\sim$1 week to 48 hrs before re-filling the system, in a such way that is not practical for a long term experiment. Additionally no significant increment in the responsivity was obtained as result of the reduction of temperature (see Chapter 4).

The results from the experiments conducted with the FTS-MPI are described and analyzed to verify the performance of the system in Chapter 5. The recorded interferograms have a low S/N ratio in the vicinity of the secondary lobes. The slow time response of the detector and the low sensitivity contribute to the low S/N interferograms. That implies, as was demonstrated in the analysis, that the computed spectrum has a profile with many fake spectral features as a result of the noise present in the interferogram. Therefore, the system is not able to record a high quality interferogram to compute the power transmission spectrum of the sky. As was shown in section 5.8 the position of the bright fringe has a temporal variation, which is a probe of the variability of the source intensity. In our case the reference source of liquid nitrogen is more susceptible to produce these variations, and therefore it is most likely to be a source of noise.

All the spectra shown have not been calibrated and corrected for the instrumental response, because we do not have a proper reference (i.e. stable, absolutely calibrated) spectrum measured with FTS-MPI system. This makes difficult to correctly interpret the computed spectra. However, we find in all the measured spectra a constant spectral shape which is the instrumental profile plus constant discrete features due to the observed source (i.e. the atmosphere)

Im confident that we have identified three spectral lines related with to water-vapour emission at frequencies of 183, 325 and 385 GHz. Another spectral feature was identified as a constant systematic instrumental response may due to the fluorogold filter. A more careful study, via an independent measure of the spectral response of our fluorogold filter, must be conducted in order to understand the response of our FTS-MPI.

System	ν range [THz]	$\Delta\nu$ [GHz]	Detector	NEP [W $Hz^{-1/2}$]	Cost
FTS-MPI	$\sim$.2 -1	0.5	NTD:Ge	1.73×10^{-14}	$\sim$8000 USD
IRLABS	$\sim$.09 -3	–	Silicon	1.5×10^{-13}	$\sim$16,000 USD
FTS (Paine et al)	$\sim$.3 -3.5	3	Silicon	1.2×10^{-12}	– USD

Table 6.1: Comparison of Fourier transform systems. The comparison is made against comercial FTS from IRLabs Inc. and a scietific system for atmospheric characterization of ALMA site (Paine et al).

Although I have identified problems in the detection system, I have also made significant progress towards providing a useful instrument for the atmospheric characterization of the LMT site. The table 6.1 shows a comparison of FTS systems, which shows that I obtained between 10 to 100 more sensitive system used for the same purpose. Also, the cost of the system is reduce to the half respect to the commercial system. Therefore, a sensitive and cheaper FTS system was achieved.

Based on results of the sky opacity at 215 GHz of the LMT site, measured by the Microwave Laboratory and the analysis reported by Ferrusca (2006) show, the dynamic behavior of the atmosphere above the LMT site. A continuous moni-

toring of the broadband atmospheric characteristic is therefore necessary in order to operate the telescope efficiently and establish the various observing strategies throughout the year (i.e. optimization of the bandpass filtering, telescope time, engineering time, etc.). In order to continue this effort I describe briefly in the next section some ideas for improving the current FTS-MPI system, as well a proposal to design a simple instrument for the LMT.

6.1 Future work

As it has been exposed in this work the Fourier transform spectroscopy has played an important role in site characterization techniques for determining the sky transmission spectrum over a wide band (e.g $\sim$ 215 - 3000 GHz). However this is not the unique application given to this technique. The Fourier transform spectrometers have been used in sub-mm/mm spectroscopy to study planet atmospheres (Weisstein, 1996), FIR studies of complex molecules (Kim & Yang, 1998) and currently new developments of 2D imaging FTS (Swinyard et al., 2000) as an example of the this technique. Therefore, we propose to design and develop a basic Fourier Transform spectrometer as part of the astronomical instruments of the LMT.

In order to have an spectroscopy instrument for the LMT we need to improve the current FTS-MPI in order to achieve a high resolution and large S/N instrument. These improvements can be achieved following two strategies: i) new design of the cryogenic detection system and, ii) large throughput interferometer.

6.1.1 He^3 bolometric system

A bolometric detection system at He^3 (i.e.$\sim$ 300 mK) will inmediately allow us to improve the performance of the bolometer. A bolometer with a total voltage noise of 10 nV/$Hz^{1/2}$ and large responsivity $\sim 10^9$ V/W (i.e. to make the Johnson noise

and amplifier noise contributions negligible), will have a noise equivalent power on the order of 10^{-17} W/Hz$^{1/2}$, which is ~ 100 times better than we obtained at 1.8 K and the responsivity would also be $\sim 10^3$ times greater.

Operational temperatures < 1 K are just possible using a refrigeration system. The most common system used is the $^4He:\,^3He$ closed-cycle fridge which provide a low microphonic-noise environment, because no mechanical pumps are used. Also another advantage of these systems is the long hold-times e.g ~ 72 h, which require little or no operator intervention, and which in practice is very suitable for long-time operation of the FTS-MPI system.

A $^4He:\,^3He$ closed-cycle fridge has two main stages: i) the ^4He refrigerator which pre-cools the heat exchanger to a temperature of 2.7 K to condense the ^3He into the reservoir; ii) and the ^3He refrigerator which has a very similar design to the ^4He stage. The vapor pressure of this stage allow us to obtain temperatures close to 0.3 K.

The complete refrigerator must be installed in a cryostat with the appropriate dimensions that allow us to allocate the coupling cold-optics and the bolometric sensor. The required cryostat will have the same configuration as the current system, with an additional 4.2 K radiation shield that provides a low background environment to the components (i.e. JFETs, thermometers, heaters, refrigerator, etc.) installed on the cold-stage.

An example of the system would be the HDL-12 or HDL-14 from IRLABS, which are 12 and 14 inches cold-plate diameter respectively. The HDL line of liquid helium dewars contains two cryogenic reservoirs, arranged in the same mechanical configuration that our cryostat. The cryostat hold-time of this models are 55 h and 78 h respectively. Custom modifications are possible in order to accomodate our needs. Figure 6.1 shows the mechanical drawing of the HDL-14. The cost of the systems are respectively in the range of $ 10,000.00 USD to $20, 000.00 USD for these models.

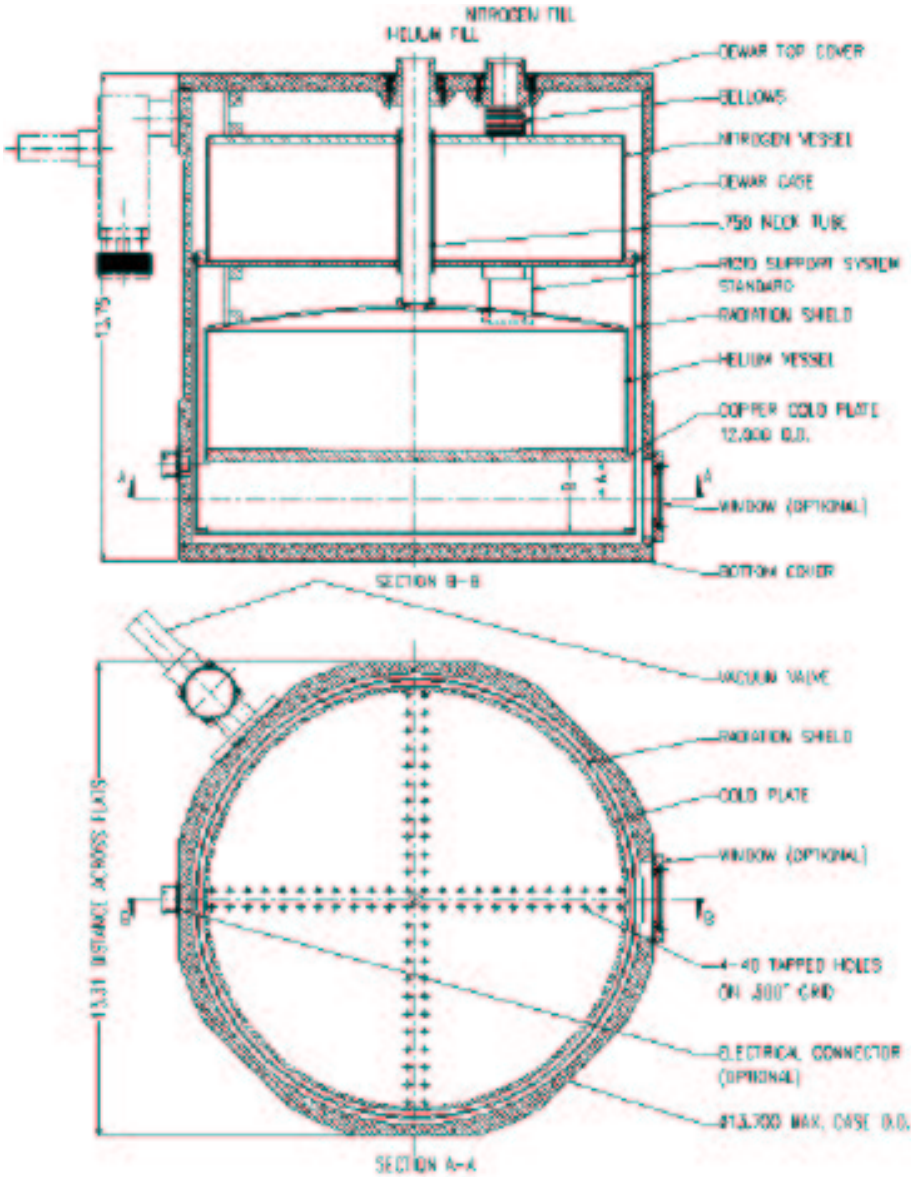

Figure 6.1: TE wave transmission and TM wave reflection characteristic for a incidence radiation at 45 degree.

6.1.2 Single pixel or pixel array?

The detection system could be a single pixel or small array. The main objective in this topic is the choice of the bolometer technology, e.g. silicon nitride composite bolometers with NTD Ge thermistor or a TES. It does not matter which technology will be used as long as the final performance parameters will be improved, such as the thermal conductance, heat capacity and hence the final NEP, responsivity.

The state-of-the-art in the field of silicon-nitride composite bolometers is represented by the Spider-Web bolometer. In this technology the absorber is a metallised silicon-nitride web structure with a small NTD germanium thermistor bump-bonded to the center. Instruments such as BoloCAM and recently AzTEC have successfully used these kind of sensors, achieving background-limited performance at temperatures of 100 - 300 mK. BoloCAM at 300 mK reported a NEP 3×10^{-17} W/Hz$^{1/2}$ and time constant of 10 ms. This technology could be explored as the next natural step for future developments at INAOE. In principle we are able to develop silicon nitride micro-machined structures in cooperation with the INAOE Department of Electronics. This facility will allow us to start testing silicon nitride spider-web devices in arrays of a few pixels.

Another investigation topic to be explored in the area of sensor technology is the use of antenna-coupled microbolometers described by Mees et al. (1991) that have some attractive features for array applications. These devices use planar lithographed antennae to coupled the radiation into a thermally active volume. The advantage of this approach is that the full array can be fabricated onto the same chip. The ultimate values of NEP are obtained by minimizing the thermal conductance G, for example G = 9×10^{-10} W/K at 450 mK giving a detector NEP of 3×10^{-16} and a time constant of ~ 0.2 ms. As well as for micro-machined structures, the planar lithographed antennas can be developed in cooperation with the Microwave Lab and the Department of Electronics.

No matter which technology we adopt, it is clear that by decreasing the temperature T_0 and minimizing the thermal conductance G, of the device we obtain a considerable gain for the detector responsivity. Therefore these lines of investigation on the silicon spider-web bolometer and TES bolometers will be explored as future work for the MI-LAB.

6.1.3 Large aperture FTS-MPI system for the LMT

In order to improve the signal-to-noise ratio it is very important to focus all the efforts toward a large throughput system. This can be achieved by using larger size optics to provide a large solid angle for collecting the light. The interferometer will be designed to be mounted at one of the available spaces of f/10.6 number of the LMT. The size of the beam passing through the system may be defined in terms of the detector beam, which in principle is modified by a focusing optics placed at the detector-port aperture-plane. The radiation entering the interferometer is collimated to reduce the divergence.

I propose to use the same Martin-Puplett interferometer scheme for the FTS. However we must focus our efforts into producing a better surface quality in all the optical components. In order to improve the quality of the optics, the optical surface will be coated with a aluminum to enhance the reflectivity. Another important issue is to provide a effective method for optical tests at sub-mm/mm wavelengths that provide information on the final optical quality of optics systems. To make improvements to the current system and to allow new designs to be realized we need to implement an alignment tool and aligning process, because any misalignment introduces phase errors and reduces the fidelity of the final computed spectrum.

Finally for the rest of the sub-systems (i.e. FTS-control, Data acquisition and processing software) no great modifications or improvements will be necessary, since we understand the basics of the FTS spectroscopy, any refinement to the

sub-systems of our 2nd generation FTS will depend on the final application.

To conclude, we have designed, built, integrated and tested a spectroscopic instrument designed to operate at millimeter wavelength. This experimental development has played an important role in the creation of the initial infrastructure and consolidation of a millimetric wavelength laboratory at INAOE. The Gran Telescopio Milimétrico (GTM) will rely heavily on the continued development of this laboratory, its resources and the acquired technical skills. The results from the initial laboratory tests demonstrate that the FTS will be capable, after improvements, of measuring the seasonal variations in the atmospheric transmission above Sierra La Negra, the site of the GTM.

Bibliography

Alpher, R. A., Herman, R., & Gamow, G. A. (1948). Thermonuclear Reactions in the Expanding Universe. *Physical Review*, *74*, 1198–1199.

Alsop, D. C., Inman, C., Lange, A. E., & Wibanks, T. (1992). Design and construction of high-sensitivity, infrared bolometers for operation at 300 mK. *Applied Optics*, *31*, 6610–6615.

Bennett, C. L., Banday, A. J., Gorski, K. M., Hinshaw, G., Jackson, P., Keegstra, P., Kogut, A., Smoot, G. F., Wilkinson, D. T., & Wright, E. L. (1996). Four-Year COBE DMR Cosmic Microwave Background Observations: Maps and Basic Results. *Astrophisical Journal Letters*, *464*, L1+.

Blain, A. W., Smail, I., Ivison, R. J., Kneib, J.-P., & Frayer, D. T. (2002). Submillimeter galaxies. *Physics Reports*, *369*, 111–176.

Blea, J. M., Parks, W. F., Ade, P. A. R., & Bell, R. J. (1970). Optical Properties of Black Polyethylene from 3 to 4000 cm-1. *Journal of the Optical Society of America (1917-1983)*, *60*, 603–+.

Chamberlin, R. A., Martin, R. N., Martin, C. L., & Stark, A. A. (2003). Submillimeter atmospheric FTS at the geographic South Pole. In Phillips, T. G. & Zmuidzinas, J. (Eds.), *Millimeter and Submillimeter Detectors for Astronomy.*

Edited by Phillips, Thomas G.; Zmuidzinas, Jonas. Proceedings of the SPIE, Volume 4855, pp. 609-620 (2003)., (pp. 609–620).

Chambers, W. G., Costley, A. E., & Parker, T. J. (1988). Characteristic curves for the spectroscopic performance of free-standing wire grids at millimeter and submillimeter wavelengths. *International Journal of Infrared and Millimeter Waves*, *9*, 157–172.

Coble, K., Dragovan, M., Kovac, J., Halverson, N. W., Holzapfel, W. L., Knox, L., Dodelson, S., Ganga, K., Alvarez, D., Peterson, J. B., Griffin, G., Newcomb, M., Miller, K., Platt, S. R., & Novak, G. (1999). Anisotropy in the Cosmic Microwave Background at Degree Angular Scales: Python V Results. *ApJL*, *519*, L5–L8.

Delgado, G., Otrola, A., & V., B. (2000). The determination of pricipitable water vapour at llano chajnantor from observations of the 183 ghz water line. *Technical report. NRAO*.

Dicke, R. H., Peebles, P. J. E., Roll, P. G., & Wilkinson, D. T. (1965). Cosmic Black-Body Radiation. *Astrophisical Journal*, *142*, 414–419.

Dragovan, M., Ruhl, J. E., Novak, G., Platt, S. R., Crone, B., Pernic, R., & Peterson, J. B. (1994). Anisotropy in the microwave sky at intermediate angular scales. *ApJL*, *427*, L67–L70.

D'yachkov, E. I. (1979). Thermal Conductivity and Electrical Resistivity of NbTi (HT-50) as fuction of temperature and Magnetic Field . *Preprint of the Joint Institute of Nuclear Research*.

Efros, A. L. & Shklovskii, B. I. (1975). Coulomb gap and low temperature conductivity of disordered systems . *Journal of Physics C Solid State Physics*, *8*, L49–L51.

Estrada, J., Meza, J., & Torres, A. (2002). Mediciones de opacidad atmosferica en el volcan sierra negra. *Technical report. INAOE/GTM, Tonantzintla, Puebla.*, *RT0545*.

Ferrusca, D. (2006). A Cryogenic ^{4}He bolometer system for detecting (sub-)-millimeter wavelength radiation.

Franceschini, A. (2001). The Cosmic Star-Formation History: The Far-IR and Sub-mm View. In *Starburst Galaxies: Near and Far*, (pp. 328–+).

Guilloteau, S. (2000). The ALMA Project (Invited Review). In Garzón, G., Eiroa, C., de Winter, D., & Mahoney, T. J. (Eds.), *ASP Conf. Ser. 219: Disks, Planetesimals, and Planets*, (pp. 645–+).

Hagmann, C., Benford, D. J., Clapp, A. C., Richards, P. L., & Timbie, P. (1992). A broadband THz receiver for low background space applications. In *Michigan Univ., The Third International Symposium on Space Terahertz Technology: Symposium Proceedings p 678-687 (SEE N93-27726 10-31)*, (pp. 678–687).

Haller, E. E., Palaio, N. P., Rodder, M., Hansen, W. L., & Kreysa, E. (1982). NTD germanium: A novel material for low-temperature bolometers. *NASA STI/Recon Technical Report N*, *83*, 28412–+.

Halpern, M., Gush, H. P., Wishnow, E., & de Cosmo, V. (1986). Far infrared transmission of dielectrics at cryogenic and room temperatures - Glass, Fluorogold, Eccosorb, Stycast, and various plastics. *Applied Optics*, *25*, 565–570.

Hughes, D. H. (2005). The Large Millimetre Telescope (LMT): tracing the evolution of structure in the early universe. In *Revista Mexicana de Astronomia y Astrofisica Conference Series*, (pp. 97–100).

Hughes, D. H. & Dunlop, J. S. (1999). Continuum Observations of the High-Redshift Universe at Sub-millimetre Wavelengths. In Carilli, C. L., Radford,

S. J. E., Menten, K. M., & Langston, G. I. (Eds.), *ASP Conf. Ser. 156: Highly Redshifted Radio Lines*, (pp. 99–+).

Hughes, D. H., Serjeant, S., Dunlop, J., Rowan-Robinson, M., Blain, A., Mann, R. G., Ivison, R., Peacock, J., Efstathiou, A., Gear, W., Oliver, S., Lawrence, A., Longair, M., Goldschmidt, P., & Jenness, T. (1998). High-redshift star formation in the Hubble Deep Field revealed by a submillimetre-wavelength survey. *Nature*, *394*, 241–247.

Ishiguro, M., Kanzawa, T., & Kasuga, T. (1990). Monitoring of atmospheric phase fluctuations using geostationary satellite signals. In Baldwin, J. E. & Wang, S. (Eds.), *URSI/IAU Symposium on Radio Astronomical Seeing*, (pp. 60–63).

Kim, C. & Yang, J. (1998). Quantitative FT-IR Analysis for Chondritic Meteorites: Search for C_60 in Meteorites. *Journal of Astronomy and Space Sciences*, *15*, 151–162.

Kooi, J. W., Schaffer, P. L., Bumble, B., Leduc, R., & Phillips, T. G. (1998). Heterodyne instrumentation at the CSO. In Phillips, T. G. (Ed.), *Proc. SPIE Vol. 3357, p. 22-32, Advanced Technology MMW, Radio, and Terahertz Telescopes, Thomas G. Phillips; Ed.*, (pp. 22–32).

Kovac, J., Dragovan, M., Schleuning, D. A., Alvarez, D., Peterson, J. B., Miller, K., Platt, S. R., & Novak, G. (1997). Anisotropy in the Cosmic Microwave Background: Results from Python IV. *Bulletin of the American Astronomical Society*, *29*, 1394–+.

Lamb, J. W. (1993). Infrared filters for cryogenic millimeterwave receivers. *International Journal of Infrared and Millimeter Waves*, *14*, 959–967.

Lange, A. E., Hayakawa, S., Matsumoto, T., Matsuo, H., & Murakami, H. (1987). Rocket-borne submillimeter radiometer. *Applied Optics*, *26*, 401–409.

Lay, O. P. & Halverson, N. W. (2000). The Impact of Atmospheric Fluctuations on Degree-Scale Imaging of the Cosmic Microwave Background. *ApJ*, *543*, 787–798.

Lee, S.-F., Gildemeister, J. M., Holmes, W., Lee, A. T., & Richards, P. L. (1998). Voltage-Biased Superconducting Transition-Edge Bolometer with Strong Electrothermal Feedback Operated at 370 mK. *Applied Optics*, *37*, 3391–3397.

Low, F. J. (1961). Low-Temperature Geranium Bolometer. *Journal of the Optical Society of America (1917-1983)*, *51*, 1300–+.

Mather, J. C. (1982). Bolometer noise: nonequilibrium thoery. *Applied Optics*, *21*, 1125–1129.

Mather, J. C., Hauser, M. G., Bennett, C. L., Boggess, N. W., Cheng, E. S., Eplee, R. E., Freudenreich, H. T., Gulkis, S., Isaacman, R. B., & Janssen, M. (1990). Early results from the Cosmic Background Explorer (COBE). In *Liege International Astrophysical Colloquia*, (pp. 25–31).

Matsuo, H., Sakamoto, A., & Matsushita, S. (1998). FTS measurements of submillimeter-wave opacity at Pampa la Bola. In Phillips, T. G. (Ed.), *Proc. SPIE Vol. 3357, p. 626-637, Advanced Technology MMW, Radio, and Terahertz Telescopes, Thomas G. Phillips; Ed.*, (pp. 626–637).

Matsushita, S., Matsuo, H., Pardo, J. R., & Radford, S. J. E. (1999). FTS Measurements of Submillimeter-Wave Atmospheric Opacity at Pampa la Bola II : Supra-Terahertz Windows and Model Fitting. *PASJ*, *51*, 603–+.

Matsushita, S., Matsuo, H., Sakamoto, A., & Pardo, J. R. (2000). FTS measurements of submillimeter opacity and other site testing at Pampa la Bola. In Butcher, H. R. (Ed.), *Proc. SPIE Vol. 4015, p. 378-389, Radio Telescopes, Harvey R. Butcher; Ed.*, (pp. 378–389).

Mauskopf, P. D., Bock, J. J., del Castillo, H., Holzapfel, W. L., & Lange, A. E. (1997). Composite infrared bolometers with Si 3 N 4 micromesh absorbers. *Applied Optics*, *36*, 765–771.

Mees, J., Nahum, M., & Richards, P. L. (1991). New designs for antenna-coupled superconducting bolometers. *Applied Physics Letters*, *59*, 2329–2331.

Mertz, L. (1965). *Transformations in Optics*. New York: John Wiley & Sons, Inc.

Nishioka, N. S., Richards, P. L., & Woody, D. P. (1978). Composite bolometers for submillimeter wavelengths. *Applied Optics*, *17*, 1562–1567.

Penzias, A. A. & Wilson, R. W. (1965). A Measurement of Excess Antenna Temperature at 4080 Mc/s. *Astrophisical Journal Letters*, *142*, 419–421.

Platt, S. R., Kovac, J., Dragovan, M., Peterson, J. B., & Ruhl, J. E. (1997). Anisotropy in the Microwave Sky at 90 GHz: Results from Python III. *ApJL*, *475*, L1+.

Puget, J. L., Lagache, G., Clements, D. L., Reach, W. T., Aussel, H., Bouchet, F. R., Cesarsky, C., Désert, F. X., Dole, H., Elbaz, D., Franceschini, A., Guiderdoni, B., & Moorwood, A. F. M. (1999). FIRBACK. I. A deep survey at 175 microns with ISO, preliminary results. *Astronomy and Astrophysics*, *345*, 29–35.

Richards, P. L. (1994). Bolometers for infrared and millimeter waves. *Journal of Applied Physics*, *76*, 1–24.

Ruhl, J. E., Dragovan, M., Platt, S. R., Kovac, J., & Novak, G. (1995). Anisotropy in the Microwave Sky at 90 GHz: Results from Python II. *ApJL*, *453*, L1+.

Sanders, D. B. & Mirabel, I. F. (1996). Luminous Infrared Galaxies. *Annual review of astronomy and astrophysics*, *34*, 749–+.

Saunders, W., Rowan-Robinson, M., Lawrence, A., Efstathiou, G., Kaiser, N., Ellis, R. S., & Frenk, C. S. (1990). The 60-micron and far-infrared luminosity functions of IRAS galaxies. *Royal Astronomical Society, Monthly Notices*, *242*, 318–337.

Scott, D., Borys, C., Chapman, S. C., Donahue, M., Fahlman, G. G., Halpern, M., & Newbury, P. (2002). A giant sub-mm lensed arc? *Bulletin of the American Astronomical Society*, *34*, 1312–+.

Serlemitsos, A. T. (1989). Flight worthy infrared bolometers with high throughput and low NEP. In Melugin, R. K. & Pierce, W. G. (Eds.), *Cryogenic optical systems and instruments III; Proceedings of the Meeting, San Diego, CA, Aug. 17-19, 1988 (A90-11251 01-31). Bellingham, WA, Society of Photo-Optical Instrumentation Engineers, 1989, p. 314-321.*, (pp. 314–321).

Smail, I., Ivison, R. J., & Blain, A. W. (1997). A Deep Sub-millimeter Survey of Lensing Clusters: A New Window on Galaxy Formation and Evolution. *Astrophisical Journal Letters*, *490*, L5+.

Soifer, B. T., Neugebauer, G., & Houck, J. R. (1987). The IRAS view of the extragalactic sky. *Annual review of astronomy and astrophysics*, *25*, 187–230.

Swinyard, B. M., Ade, P. A., Griffin, M. J., Dohlen, K., Baluteau, J.-P., Pouliquen, D., Ferand, D., Dargent, P., Michel, G., Martignac, J., Rodriguez, L., Jennings, D. E., Caldwell, M. E., Richards, A. G., Hamilton, P. A., & Naylor, D. A. (2000). FIRST-SPIRE spectrometer: a novel imaging FTS for the submillimeter. In Breckinridge, J. B. & Jakobsen, P. (Eds.), *Proc. SPIE Vol. 4013, p. 196-207, UV, Optical, and IR Space Telescopes and Instruments, James B. Breckinridge; Peter Jakobsen; Eds.*, (pp. 196–207).

Torbet, E., Devlin, M. J., Dorwart, W. B., Herbig, T., Miller, A. D., Nolta, M. R., Page, L., Puchalla, J., & Tran, H. T. (1999). A Measurement of the Angular

Power Spectrum of the Microwave Background Made from the High Chilean Andes. *ApJL*, *521*, L79–L82.

Torres, V., Davydova, V., Carrasco, L., & Guzmn, I. (1997). Evaluation of the long term behaviour of sites for mm-wavelength radioastronomy: the quest for a site for the large millimeter telescope. *Technical report. INAOE/GTM, Tonantzintla, Puebla.*, *Dic.97*.

van Vleck, J. H. (1947a). The Absorption of Microwaves by Oxygen. *Physical Review*, *71*, 413–424.

van Vleck, J. H. (1947b). The Absorption of Microwaves by Uncondensed Water Vapor. *Physical Review*, *71*, 425–433.

Weisstein, E. W. (1996). Millimeter/submillimeter Fourier Transform Spectroscopy of Jovian Planet Atmospheres. *Ph.D. Thesis*.

List of Figures

List of Tables